Origami-inspired micro folding actuators based on Shape Memory Alloys

---

Zur Erlangung des akademischen Grades einer
DOKTORIN DER INGENIEURWISSENSCHAFTEN (Dr.-Ing.)

von der KIT-Fakultät für Maschinenbau des
Karlsruher Instituts für Technologie (KIT)
genehmigte

DISSERTATION

von

M.Sc. Lena Annkathrin Seigner

Hauptreferent:	Prof. Dr. Manfred Kohl
Korreferent:	Prof. Dr. Martin Hoffmann
Tag der mündlichen Prüfung:	12. März 2025

Karlsruher Institut für Technologie
Institut für Mikrostrukturtechnik
H.-v.-Helmholtz Platz 1
76344 Eggenstein-Leopoldshafen

Abstract

As technical systems become more complex, traditional actuator designs may fall short in addressing the flexibility and reconfigurability needed for diverse applications. Besides multifunctionality, the miniaturization of components is an ongoing trend. The new research area of “re-programmable matter” addresses both challenges. It refers to materials or small-scale systems, i.e. continuous on the human length scale, that can alter their physical properties or geometry in response to external stimuli. Their adaptability is particularly valuable for applications in robotics, aerospace and biomedical devices. The inspiration for many emerging designs is based on art of Origami, which demonstrates how complex 3D structures can be created from simple two-dimensional (2D) sheets, exclusively through folding. Origami-based structures allow for compact storage of foldable 3D shapes. Planar fabrication techniques can be used to reduce manufacturing complexity and cost. The final 3D shapes are folded on demand according to their function.
Folding mechanisms can be achieved through the use of smart materials that respond to non-mechanical stimuli, such as thermal or electrical fields. These materials offer significant advantages in terms of design simplicity and miniaturization. Shape memory alloys (SMAs), e.g. TiNi, can generate high bending moments, are robust and biocompatible. They have the ability to "remember" their original shape and return to it after deformation, when heated. This property, known as the shape memory effect, is the result of a thermally induced phase transformation between the martensitic (cold) and austenitic (heated) phases of the alloy.
This thesis explores the integration of SMA foils as a key component for a miniaturized folding actuator. The focus here is on the development and characterization of a basic unit that can be expanded into a more complex origami system. It consists of a pair of rigid tiles that are interconnected by a TiNi double bridge for uni-directional folding, or two antagonistic TiNi double bridges for bi-directional folding. Precise folding and unfolding to discrete angles is enabled through localized Joule heating, ensuring reversible and programmable folding motions. The work covers three parts: First, the maximum bending angle and bending moment of the basic unit are characterized for macroscopic and micro scale folding actuators, respectively. Second, the enhancement of the folding

angle is investigated by extending the double bridge layout via cascading. Finally, a reversible latching mechanism based on magnetic interaction is explored.
The macroscopic unidirectional folding actuator features a 20 µm thick laser-structured TiNi double bridge, heat-treated in a vacuum furnace to achieve a +180° angle. After manually unfolding it to 0°, it can reset to +150°. The bending moment produced by the phase transformation upon heating is measured at 0.11 Nmm. When paired with an antagonist (heat-treated for -180°), the equilibrium between the bending moment of the protagonist (in austenite state) and the opposing bending moment of the antagonist (in martensite state) defines the maximum bi-directional folding angle. Using a rotational test setup, a bending moment of 0.03 Nmm is required for unfolding to 0°. The balance of bending moments theoretically allows for a bi-directional folding angle of ±100°. However, due to thermo-mechanical coupling between the two folding actuators, the experimental range achieved is limited between -40° and +42°.
With the aim of miniaturization, a microstructuring process using photolithography and wet chemical etching is being developed. The heat treatment required to set a folding angle of +180° is achieved through Joule heating. Actuators, reduced by a factor of 10 by controlled etching of 20 µm cold-rolled TiNi foil, reach a unidirectional folding angle of +145°. They exhibit a maximum bending moment of 0.13×10^{-3} Nmm. Using 5 µm thin sputtered TiNiCu films, actuators with bridge dimensions of 400 µm × 90 µm × 5 µm can achieve unidirectional folding angles of up to +150° and bidirectional angles of ±50°.
By developing a cascaded design, which involves the series connection and interlacing of two bending elements, the folding range is extended to +180° (unidirectional) and ±105° (bidirectional).
The reversible magnetic latching mechanism consists of a NiMnGaCu soft magnet and NdFeB permanent magnet. The 5 µm NiMnGaCu thin film is applied to the freely movable tile and changes from ferromagnetic to paramagnetic state by local heating above the Curie temperature. Its magnetic interaction with the cylindrical NdFeB magnet (diameter of 1 mm) can be controlled for (un)latching of folding actuators. The cascaded folding actuator can achieve an extended bi-directional folding angle of +125° due to the additional bending moment generated by the magnetic attraction force of up to 2.5 mN. The folding actuator remains latched even after cooling. Two mechanisms for releasing the magnetic latching system are being investigated: Actuation of the antagonist requires a heating power of approximately 55 mW, while the reduction of magnetic force by resistance heating of the NdFeB magnet becomes effective at a heating power of 210 mW.

Kurzfassung

Da technische Systeme immer komplexer werden, können herkömmliche Aktorkonzepte die für verschiedene Anwendungen erforderliche Flexibilität und Rekonfigurierbarkeit nicht mehr gewährleisten. Neben der Multifunktionalität ist auch die Miniaturisierung von Komponenten ein anhaltender Trend. Das neue Forschungsgebiet der „(re-)programmierbaren Materie“ befasst sich mit diesen beiden Herausforderungen. Hierbei handelt es sich um Materialien oder Systeme in kleinem Maßstab, d.h. kontinuierlich auf der menschlichen Längenskala, die ihre physikalischen Eigenschaften oder ihre Geometrie als Reaktion auf äußere Reize verändern können. Ihre Anpassungsfähigkeit ist besonders wertvoll für Anwendungen in der Robotik, der Luft- und Raumfahrt und für biomedizinische Geräte. Die Inspiration für viele neue Designs basiert auf dem Konzept von Origami, das zeigt, wie komplexe 3D-Strukturen aus einfachen zweidimensionalen (2D) Blättern ausschließlich durch Falten entstehen können. Origami-basierte Strukturen ermöglichen eine kompakte Lagerung von faltbaren 3D-Formen. Planare Fertigungstechniken können eingesetzt werden, um die Komplexität und Herstellungskosten zu reduzieren. Die endgültigen 3D-Formen werden dann bei Bedarf entsprechend ihrer Funktion gefaltet.
Faltmechanismen können durch den Einsatz sogenannter intelligenter Materialien erreicht werden, die auf nicht-mechanische Reize, wie thermische und elektrische Felder, reagieren. Diese Materialien bieten erhebliche Vorteile in Bezug auf einfache Designs und Miniaturisierung. Formgedächtnislegierungen (FGL), wie z. B. TiNi, können hohe Biegemomente erzeugen, sind robust und biokompatibel. FGLs haben die Fähigkeit, sich an ihre ursprüngliche Form zu „erinnern“ und diese nach einer Verformung wieder anzunehmen, wenn sie erhitzt werden. Diese Eigenschaft, der so genannte Formgedächtniseffekt, ist das Ergebnis einer thermisch induzierten Phasenumwandlung zwischen der martensitischen (kalten) und austenitischen (erwärmten) Phase der Legierung.

In dieser Arbeit wird die Integration von FGL-Folien als Schlüsselkomponente für einen miniaturisierten Faltaktor untersucht. Der Schwerpunkt liegt dabei auf der Entwicklung und Charakterisierung einer Grundeinheit, die zu einem komplexeren Origami-System erweitert werden kann. Es besteht aus zwei Kacheln, die durch eine TiNi-Doppelbrücke

für unidirektionales Falten oder zwei antagonistische TiNi-Doppelbrücken für bidirektionales Falten miteinander verbunden sind. Durch lokale Joulesche Erwärmung kann präzises Falten und Entfalten ermöglicht werden, sodass reversible und programmierbare Faltmuster entstehen können. Die Arbeit umfasst drei Teile: Erstens werden der maximale Biegewinkel und das Biegemoment der Grundeinheit für makroskopische bzw. mikroskopische Faltaktoren charakterisiert. Zweitens wird die Erweiterung des Faltwinkels durch Kaskadierung der Doppelbrückenstruktur untersucht. Schließlich wird ein reversibler Rastmechanismus auf der Grundlage magnetischer Wechselwirkung erforscht.

Der makroskopische unidirektionale Faltaktor besteht aus einer 20 µm dicken, laserstrukturierten TiNi-Doppelbrücke, die in einem Vakuumofen wärmebehandelt wird, um einen Winkel von +180° zu erreichen. Nach dem manuellen Ausklappen auf 0° kann er auf +150° zurückgestellt werden. Das Biegemoment, das durch die Phasenumwandlung beim Erhitzen entsteht, wird mit 0,11 Nmm gemessen. Bei der Paarung mit einem Antagonisten (auf -180° wärmebehandelt) bestimmt das Gleichgewicht zwischen dem Biegemoment des Protagonisten (im Austenit-Zustand) und dem entgegengesetzten Biegemoment des Antagonisten (im Martensit-Zustand) den maximalen bidirektionalen Biegewinkel. Bei Verwendung eines rotativen Versuchsaufbaus ist ein Biegemoment von 0,03 Nmm für die Entfaltung auf 0° erforderlich. Das Gleichgewicht der Biegemomente erlaubt theoretisch einen bidirektionalen Biegewinkel von ±100°. Aufgrund der thermomechanischen Kopplung zwischen den beiden Faltaktoren ist der experimentelle Bereich jedoch auf -40° bis +42° begrenzt.

Mit dem Ziel der Miniaturisierung wird ein Mikrostrukturierungsverfahren unter Verwendung von Photolithographie und nasschemischem Ätzen entwickelt. Die zur Einstellung eines Faltwinkels von +180° erforderliche Wärmebehandlung wird durch Joule-Erwärmung erreicht. Aktoren, die durch kontrolliertes Ätzen der 20 µm kaltgewalzten TiNi-Folie um den Faktor 10 verkleinert werden, erreichen einen unidirektionalen Faltwinkel von +145°. Das maximale Biegemoment beträgt 0.13×10^{-3} Nmm. Unter Verwendung von 5 µm dünnen gesputterten TiNiCu-Folien können Aktoren mit Brückenabmessungen von 400 µm × 90 µm × 5 µm unidirektionale Faltwinkel von bis zu +150° und bidirektionale Winkel von ±50° erreichen.

Die Entwicklung eines kaskadierten Layouts, das aus der Reihenschaltung zweier Biegeelemente besteht, erweitert den Faltbereich auf +180° (uni-direktional) und ±105° (bidirektional) bei Heizleistungen im Bereich von 80 mW.

Der reversible magnetische Rastmechanismus besteht aus einem NiMnGaCu-Weichmagneten und einem NdFeB-Hartmagneten. Der 5 µm NiMnGaCu-Film wird auf eine Kachel platziert und wechselt beim Erwärmung überhalb der Curie-Temperatur vom ferromagnetischen

in den paramagnetischen Zustand. Seine magnetische Wechselwirkung mit dem zylindrischen NdFeB-Magneten (Durchmesser 1 mm) kann für das Einrasten und Lösen von Faltaktoren gesteuert werden. Der kaskadierte Faltaktor kann aufgrund des zusätzlichen Biegemoments, das durch die magnetische Anziehungskraft von bis zu 2,5 mN erzeugt wird, einen erweiterten bidirektionalen Faltwinkel von +125° erreichen. Der Faltantrieb bleibt auch nach dem Abkühlen eingerastet. Es werden zwei Mechanismen zum Lösen untersucht: Die Aktuierung des Antagonisten erfordert eine Heizleistung von ca. 55 mW, während die Verringerung der Magnetkraft durch Widerstandserwärmung des NdFeB-Magneten bei einer Heizleistung von 210 mW wirksam wird.

Acknowledgements

Working in the field of shape memory alloys the past years has been both a pleasure and valuable experience for me. This thesis would not have been possible without the support of supervisors, co-workers, friends and family, to whom I would like to express my gratitude.

First and foremost, I would like to thank my supervisor Prof. Dr. Manfred Kohl, for the opportunity to explore this exciting area of research. His guidance and support throughout my thesis have been instrumental in expanding my knowledge. I appreciate him being always available for discussions and sharing his expertise.
I would also like to thank Prof. Dr. Martin Hoffmann for being my co-referee, taking the time and effort to review my work.

I would like to express my appreciation to all cooperation partners that contributed to the outcome of this work. Prof. Dr. Eckhard Quandt and his team, particularly Dr. Sabrina Curtis, supported me with superior TiNiCu thin films. Dr. Sebastian Fähler and Dr. Lukas Fink from IFW Dresden provided me with NiMnGa specimens. Furthermore, I would also like to express thanks to my research project partners, Dr. Frank Wendler, Georgino Tshikwand, and Olha Bezsmertna, for fruitful discussions and contributing to our shared vision. Particularly, I would like to mention Vincent Gottwald for his valuable contributions to the progress of our research.

I would like to extend my appreciation to my colleagues at the institute for their support throughout my time at IMT. My special thanks go to Dr. Joel Joseph, Dr. Kiran Jacob and Gowtham Arivanandhan for introducing me to fabrication processes and supporting me with HF-etching. I highly value our long discussions on new technical concepts but also off-topic subjects like Indian culture. I thank Carina Ludwig, Xi Chen, Li Zixiong, Danni Li and Alban Muslija for creating a very supportive atmosphere within our research group.

I am grateful to all staff at IMT for their support. Special thanks to Heike Fornasier, Birgit Hübner and Anja Eberhardt for their assistance in cleanroom fabrication and etching. I appreciate Alexandra Moritz and her team for their help in manufacturing components for test setups. Thanks to Nina Giraud for her guidance with ordering and organizing conventions. I appreciate Sagar Wadhwa for his support with laser cutting. Thanks to all other IMT members who made the time at the institute very memorable.

I express my gratitude to DFG for funding this research as part of the special priority program SPP 2206 and appreciate the discussions and shared knowledge at our bi-annual meetings.

I am grateful for the support and encouragement of my family and friends. They patiently supported me through this journey but also reminded me of the importance of balance. I would like to express special thanks to my parents, siblings, and parents-in-law for babysitting and being a constant source of motivation. My deepest gratitude goes to my partner for his unwavering support and understanding during demanding times of the thesis. Finally, I would like to thank my daughter for always reminding me of the joy of curiosity.

Publications

Parts of this thesis and related work have already been published:

in scientific journals

- **Seigner L.**, Tshikwand G. K., Wendler F., Kohl M., "Bi-directional Origami-Inspired SMA Folding Microactuator", *Actuators*, vol. 10, no. 8, 2021.
- Tshikwand G. K., **Seigner L.**, Wendler F., Kohl M., "Coupled Finite Element Simulation of Shape Memory Bending Microactuator", *Shape Memory and Superelasticity*, vol. 8, no. 4, pp. 373-393, 2022.
- Curtis S.M., Gugat J.L., Bumke L., Dengiz D., **Seigner L.**, Schmadel D., Lazarus S., Quandt E., "Thin-Film Superelastic Alloys for Stretchable Electronics". *Shape Memory and Superelasticity*, vol. 9, no. 1, pp. 35-49, 2023.

in conference proceedings

- **Seigner L.**, Bezsmertna O., Fähler S., Tshikwand G. K., Wendler F., Kohl M., "Origami-Inspired Shape Memory Folding Microactuator", *1st International Electronic Conference on Actuator Technology: Materials, Devices and Applications (IeCAT)*, 23-27 November 2020
- **Seigner L.**, Bezsmertna O., Fähler S., Kohl M., "Origami-basierte Mikroaktorik", *Mikrosystemtechnik-Kongress 2021*, 8-10 November 2021
- **Seigner L.**, Gottwald V., Bumke L., Quandt E., Kohl M., "Enhanced Bi-Directional SMA Actuation of Origami-Inspired Microstructures", *Mikrosystemtechnik-Kongress 2023*, 23-25 Oktober 2023

as conference contributions

- **Seigner L.**, Bezsmertna O., Fähler S., Tshikwand G. K., Wendler F., Kohl M., Origami-Inspired Shape Memory Folding Microactuator, 1st International Electronic Conference on Actuator Technology: Materials, Devices and Applications (IeCAT), 23-27 November 2020, *oral presentation*
- **Seigner L.**, Bezsmertna O., Fähler S., Kohl M., "Origami-basierte Mikroaktorik", *Mikrosystemtechnik-Kongress 2021*, 8-10 November 2021, *oral presentation*
- **Seigner L.**, Gottwald V., Bumke L., Quandt E., Kohl M., "Enhanced Bi-Directional SMA Actuation of Origami-Inspired Microstructures", *Mikrosystemtechnik-Kongress 2023*, 23-25 Oktober 2023, *oral presentation*

Contents

List of Parameters and Indices

Parameters and Symbols

Symbol	Unit	Name
$\mathbf{A}$	[-]	Austenite
$\mathbf{A_c}$	m	cross-sectional area
$\mathbf{A_f}$	K	Austenite finish temperature
$\mathbf{A_s}$	K	Austenite start temperature
α	°	folding angle
$\boldsymbol{B}$	T	magnetic flux density
$\boldsymbol{B_r}$	T	remanent magnetic field
$\mathbf{C_A}$	MPa/K	Clausius-Clapeyron coefficient (unloading)
$\mathbf{C_M}$	MPa/K	Clausius-Clapeyron coefficient (loading)
$\boldsymbol{c_p}$	J/kg/K	specific heat capacity (constant pressure)
$\boldsymbol{d}$	mm	distance
$\boldsymbol{E}$	GPa	Young's modulus
$\boldsymbol{\varepsilon}$	[-]	strain
$\boldsymbol{\varepsilon_r}$	[-]	residual strain
$\boldsymbol{\varepsilon_t}$	[-]	transformation strain
$\boldsymbol{F_r}$	N	restoring force
$\mathbf{G}$	J	Gibbs potential
γ	°	tilt angle
$\boldsymbol{H}$	A/m	magnetic field
$\boldsymbol{H_c}$	A/m	coercivity
$\mathbf{I_{heating}}$	A	heating current
$\mathbf{k_{th}}$	W/m/K	thermal conductivity
$\boldsymbol{k_{th}}$	J/K	Boltzmann constant
$\kappa_\mathbf{e}$	S/m	electrical conductivity
$\boldsymbol{l}$	mm	length

$\boldsymbol{l_0}$	mm	initial length
$\boldsymbol{\Delta l}$	mm	length difference
$\mathbf{M}$	[-]	Martensite
$\boldsymbol{M}$	Am²/kg	magnetization
$\mathbf{M_f}$	K	Martensite finish temperature
$\mathbf{M_s}$	K	Martensite start temperature
$\mathbf{M_z}$	Nmm	bending moment
$\vec{m}$	Am²	magnetic moment
$\boldsymbol{r}$	mm	folding radius
$\boldsymbol{R}$	Ω	electrical resistance
$\boldsymbol{res}$	$\Omega.cm$	electrical resistivity
$\boldsymbol{\sigma}$	MPa	Stress
$\boldsymbol{\sigma_{crit}}$	MPa	Critical transformation stress
$\boldsymbol{T_c}$	K	Curie temperature
$\boldsymbol{t_{SMA}}$	mm	SMA thickness
$\boldsymbol{\theta}$	°	opening angle ($\theta = 180 - \alpha$)
$\boldsymbol{w}$	mm	width
$\boldsymbol{\xi}$	[-]	Martensite volume fraction

Indices

Index	Name
A	Austenite
br	bridge
f	finish
M	Martensite
max	maximum
pad	pad
s	start
mag	magnetic

List of Abbreviations

AOD	Acousto-optic deflector
AOM	Acousto-optic modulator
DMM	Digital Multimeter
DSC	Differential Scanning Calorimetry
FEM	Finite Element Method
HAF	Heat Affected Zone
HP	Hinge Pair
IR	Infrared
LEM	Lumped Element Model
MEMS	Microelectromechanical Systems
MSMA	Magnetic Shape Memory Alloy
Nd:YAG	Neodymium-doped Yttrium Aluminium Garnet
PE	Pseudoelasticity
PEB	Post Exposure Bake
PI	Polyimide
PMMA	Polymethylmethacrylate
PVD	Physical Vapor Deposition
RD	Rolling Direction
RT	Room Temperature

RTA Rapid Thermal Annealing

SMA Shape Memory Alloy

SME Shape Memory Effect

SMP Shape Memory Polymer

TD Tranverse Direction

UV Ultra Violet

1. Introduction

1.1. Motivation

In today's increasingly interconnected world, driven by miniaturization and digital technology advancements, the demands placed on technical systems are growing rapidly. In a broad range of applications, from industrial automation and robotics to biomedical devices, systems become more complex and highly integrated, incorporating a growing number of sensor and actuator components. In recent years, significant progress has been made in sensor technology, data acquisition, and analysis, leading to the development of innovative and automated systems. However, actuator technologies have not advanced at the same pace as other system components, particularly in the context of miniaturized systems, which limits the overall performance and capabilities of these integrated solutions.
Microactuators, in particular, face critical challenges in meeting the high demands of compact system applications, such as generating sufficient force, achieving large displacements, and high-frequency operation, with limited space, power, or thermal constraints. Such advancements are critical for addressing future challenges in emerging fields such as robotics, microelectromechanical systems (MEMS), biomedical implants, and wearable technologies. To meet these demands, there is an urgent need for innovative microactuator designs that can deliver enhanced performance while maintaining small form factors, enabling precise control and manipulation in diverse and complex environments. These performance criteria are particularly challenging for applications where actuators are required to interface with sensors in real-time, driving the need for fast response times and accurate motion control.

One promising approach to solving these challenges lies in the concept of "programmable matter", a new paradigm in which materials or small-scale systems can be programmed to change their physical propertiess or their geometry. This concept envisions the ability to dynamically alter the behavior of programmable matter, enabling it to perform different tasks depending on the application. This capability is particularly attractive for scenarios

where remote or autonomous operation is required, such as in space exploration, where tools or structures could be created on-site, or in minimally invasive medical procedures, where precise operations need to be performed in constrained environments. To put it simply, a structure can be a fork one moment and deformed into a spoon the next.
From the perspective of materials produced through additive manufacturing, programmable matter can also be categorized as 4D printing, where 3D-printed structures are designed to transform over time in response to external stimuli [1]. These structures exhibit unique properties such as self-assembly, multifunctionality, and even self-repair. The realization of 4D printing has been made possible by the rapid advancements in smart materials – materials engineered to respond to environmental changes such as temperature, humidity, or light - and 3D printing technologies.
A novel approach for realizing such programmable, complex actuator systems is inspired by the principles of origami folding. In this concept, an initially planar structure composed of rigid, interconnected tiles can be folded into various three-dimensional shapes, through controlled bending movements at the joints. The ability to achieve different 3D configurations starting from the same planar structure allows for multifunctionality and adaptability in a wide range of applications. The role of miniaturization is crucial in this context: the smaller the individual tiles, the finer and more complex the resulting 3D structures can be, providing enhanced functionality and precision.
The concept of programmable matter has already been demonstrated at the macroscopic scale. Hawkes et al. [2] present a structure of 32 tiles and uni-directional folding actuators realized from structured shape memory alloy foils. The structure can fold into two distinct origami patterns; however, the reversion to the original planar state must be done manually.

1.2. Objectives

The objective of the present work is to scale this concept down to the micrometer range. To achieve this, thin, functional materials must be utilized, and advanced manufacturing and assembly techniques must be developed that are compatible with microsystem integration. For the adoption of a self-folding mechanism, thin-film shape memory alloys (SMAs) are microstructured accordingly and the folded configuration is set as the new “memory” shape. A folding motion is achieved by local activation through heating. Given the challenge of manual intervention at the microscale, a bi-directional folding mechanism is necessary to enable automatic resetting to the initial planar state. One potential solution is the antagonistic pairing of two uni-directional folding actuators, which

can facilitate reversion to the planar state. For shape memory materials, this would involve selective actuation to control the folding sequence. The outstanding capacity of the actuator system to reach different programmable folding states is referred to as "re-programmable matter". In addition, an approach to maintain the folded configuration is required, particularly for applications where stability in the folded state is critical. This can be achieved through the integration of magnetic actuators, capable of latching the structure in place. A combination of a hard magnet and a switchable soft magnet is proposed as a potential solution, enabling not only secure latching but also controlled release.

This work was conducted in the framework of the priority program KOMMMA (Cooperative Multistage Multistable Microactuator Systems [3]. The materials necessary for the development of microactuators are provided by external partners, including collaborators from IFW Dresden and CAU Kiel. Additionally, the simulation of the overall system is conducted in cooperation with the Institute of Materials Simulation at FAU Erlangen. The materials provided will be extensively characterized in order to design a folding actuator consisting of SMA double bridges, polyimide tiles and soft magnetic NiMnGa films. The engineering of re-programmable micro matter comprises three steps. First, the feasibility of unidirectional repetitive folding with thin film materials is to be demonstrated on a macro scale. In addition, the upscaling to a bidirectional actuator must be investigated, which includes the coupling and the resulting interaction effects of two individual folding actuators. A key challenge in this research is the integration of diverse materials through suitable manufacturing processes while ensuring that the micro-scale folding actuators meet the performance criteria of large uni- and bi-directional folding angles, high bending moments and low heating power. Due to the small dimensions of these actuators, it is imperative to design and implement specialized devices and test setups capable of high-precision measurements at the microscale. In a second step, the angular folding range can be improved by modifying the simple double-bridge layout towards a multi-stage folding concept. The effect of downscaling and design optimizations on the folding performance, in terms of uni- and bi-directional folding angle, bending moment, and required heating power, is to be investigated. In the third part, the integration of magnetic latching and controlled unlatching is studied. The magnetic interaction between soft and hard magnet has to be investigated and different unlatching concepts are to be tested. The main focus of this work is the development and characterization of a single bi-directional folding actuator unit, with the potential for future upscaling to a network of multiple cooperative folding actuators. This approach aims to lay the foundation for more complex and integrated systems capable of dynamic shape adaptation by re-programming.

1.3. Outline

Chapter 2 begins with a brief introduction to the principles of origami and its wide range of applications. It then covers the basic aspects of shape memory alloys and ferromagnetic materials. A review of prior research on self-folding actuators based on shape memory alloys is provided, followed by an introduction to the concept and operational principles of the micro-folding actuator designed in this work. Chapter 3 details the fabrication and characterization methods utilized in this thesis. Due to the variety of materials, the corresponding material characterization results are described in the relevant sections. In Chapter 4, the development and characterization of macroscale double-bridge folding actuators are described, with a focus on the transition to bi-directional folding and miniaturization. Chapter 5 explores methods for achieving larger folding angles through cascading, along with the characterization of these structures. Chapter 6 extends the cascaded folding actuators by incorporating magnetic latching mechanisms. Finally, Chapter 7 presents a summary of the key findings and offers perspectives for future research.

2. Fundamentals and State of the Art

The following chapter will introduce the characteristics of origami, the basics of folding, and the properties of shape memory alloys and ferromagnetic Heusler alloys. An overview of relevant work in this field is provided and the operation principle of a novel micro folding actuator including magnetic latching is presented.

2.1. Origami and Folding Mechanics

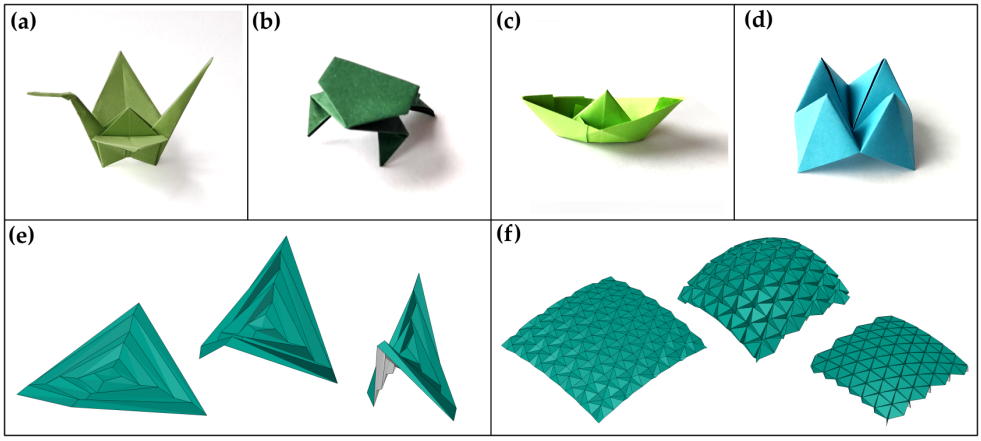

Figure 2.1.: Famous origami patterns: **(a)** crane, **(b)** frog, **(c)** boat, **(d)** lotus flower, **(e)** Hypar structure, **(f)** Resch triangular tessellation (RTT). **(e)**-**(f)**: created using the online tool *Origami Simulator* [4].

The term *origami* originates from the Japanese roots *ori* (folded) and *kami* (paper), known as the art of paper folding. Its underlying principle is straightforward: starting from a planar sheet, it is transformed into various 3D shapes, exclusively by creasing it along lines. This ancient art has a rich history and has produced a number of popular patterns, some of which are shown in Figure 2.1. Most people are familiar with origami animals, such as the crane (a) or the frog (b), but it also includes paper toys like boats (c) and the lotus flower (d). Origami tessellations, which are based on grids of geometric shapes, are another category of origami. Examples are the Hypar (hyperbolic paraboloid) structure (e)

and the triangular tessellation (f) designed by R.Resch [5] which can generate surfaces with various curvatures and has potential for practical applications. The Hypar structure like some other 3D structures exhibit interesting properties: They are bistable and show snapping behavior at the corners of the outer boundaries.
One of the best-known origami tessellations is Miura Ori shown in Figure 2.2. This periodic parallelogram pattern (a) was designed by K. Miura in the 1970s [6]. As shown in the folding sequence (b) it can be folded from a planar configuration into a more compact flat shape. The pattern has unique mechanical properties, including tunable (positive or negative) Poisson ratio and stiffness. Additionally, the Miura origami shows bistability for certain side length ratios of the parallelograms. Two neighboring Miura tubes can be set in a zig-zag arrangement, resulting in a stiff structure with a single degree of freedom, resisting other bending and twisting modes [7]. The Miura ori is highly versatile and tunable, making it a popular choice in various engineering applications.

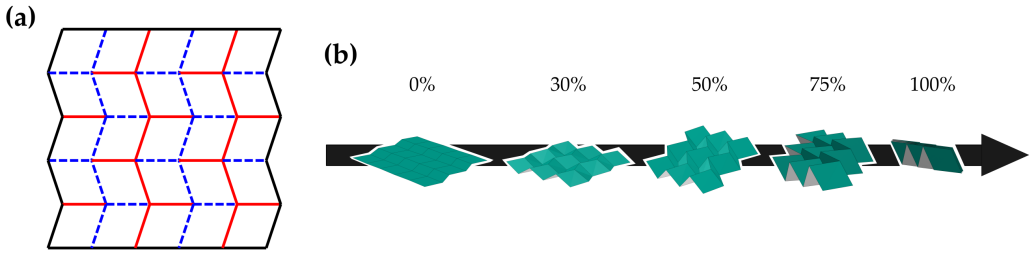

Figure 2.2.: Miura Ora origami structure **(a)** Crease pattern, **(b)** 3D folding sequence in percentage of the final configuration.

Based on Meloni [8], the terminology of origami is explained using a unit cell of the Miura structure (refer to Figure 2.3 (a)). Each origami pattern can be uniquely defined by its *crease pattern*. The flat configuration is termed as reference configuration and is a bounded planar surface without overlaps. A *crease* is a line along which a fold takes place, a *vertex* is a point where several creases meet, and a *face* is a region bounded by creases and the sheet boundary [9]. Crease patterns indicate where and what type of folds occur. A fold is a crease with a certain fold angle α and it is defined by the relative angle between the two neighboring faces. It can either be of mountain type if convex ($-\pi < \alpha < 0°$) or of valley type when concave ($0° < \alpha < \pi$). An origami is considered to be flat-foldable, e.g. the Miura ori, when the fold angles of mountain and valley folds can reach $-\pi$ and $+\pi$.
In the 1970s it was mathematically proven that theoretically an endless number of shapes can be achieved by traditional origami [9]. This discovery has raised the attention of mathematicians and scientists, leading to a study of the origami theory and the establish-

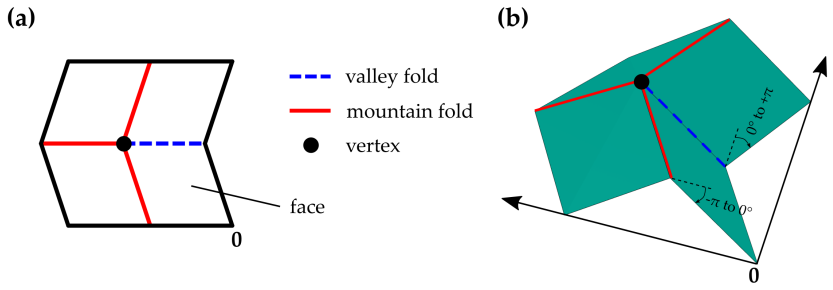

Figure 2.3.: (a) Crease pattern of Miura ori unit cell, **(b)** folded configuration of Miura ori unit cell.

ment of fundamental laws. Scholars such as Lang [10], Demaine [11], and Fuchi [12] have proposed various origami design methods and kinematic models. A transformation from a reference to a final configuration of a sheet must fulfill three properties [13]:

1. The faces undergo exclusively rigid deformations (no stretching nor bending)
2. The overall sheet is not torn (all joint faces remain joined)
3. The sheet does not self-intersect.

These limitations are important in the consecutive design of new patterns and enable the simulation models of complex folding patterns. The *Rigid Origami Simulator* [14] and *Freeform Origami* [15], developed by Tachi T., are among the most famous simulation and visualization models imposing constraints on the fold angles to derive valid configurations. Similarly, the online tool *Origami Simulator* [4] is based on structural truss representations [16], as proposed by Schenk and Guest [17]. It has been used to generate the 3D images in Figures 2.1 - 2.3. Zhu et al. [18] offer a comprehensive overview of existing simulation techniques and models.

The understanding and modeling tools open up new possibilities for manufacturing, assembly, and design of morphing structures based on origami layouts. In recent years scientists and engineers came up with interesting applications and tools. Origami-inspired structures are particularly useful for applications that require compact storage and on-demand folding (e.g. wings [19]) as they occupy a minimum of space when not in use. For instance, airbags are inserted into small cylindrical housings and can be stored more efficiently by folding them in an origami pattern [20]. In the event of a collision, the structure can be inflated into an air cushion. With more elaborate folding patterns, the deployment mechanisms can be more efficient than conventional airbag folding schemes,

reaching the inflated state within milliseconds. Also, the aerospace and medical fields (e.g. for minimally invasive surgery) rely on minimizing weight and volume. Origami-inspired structures can be particularly useful in these scenarios as they can be compactly stored and deployed at the actual site of operation, whether it be in orbit or inside the human body. Despite being lightweight, these structures can be strong and flexible depending on their configuration. Another advantage is the reduction in manufacturing complexity. Ultimately, three-dimensional structures can be fabricated in 2D with fewer components and reduced material usage. The additional use of self-folding structures helps to minimize the number of required assembly steps. This advantage is particularly interesting for smaller structure sizes when mounting by conventional techniques becomes more difficult. Microfabrication technologies allow to produce large foldable origami structures while conserving resources. For this reason, origami-inspired patterns have become particularly popular in micro and nanometer technology. A very important feature of origami structures is their reconfigurability [21] (e.g. used for antennas [22] or acoustic waveguides [23]). After being designed, a crease pattern can be transformed into multiple 3D configurations and thereby adapt their shape to specific constraints. Such structures can be assigned to the field of 4D fabrication. Adaptable structures are particularly important in robotics, where components should accommodate to the shape and surface [24]. The geometrical properties of origami-based designs allow for scaling across all length scales. Certain patterns retain important features independent of scale, which has led to a broad range of applications in recent years.

2.1.1. Origami Applications

Engineering applications for origami also combine with kirigami. This alternative folding art additionally involves cuts. Figure 2.4 provides an overview across all scales and the associated research areas. The smallest origami-inspired structures are made of DNA and are designed from long single-stranded threads of DNA called "scaffolds". Short synthetic oligonucleotide molecules are used to hold a folded scaffold in place by adhering onto fixed cross-over points [31]–[33] and thereby constructing 3D nanostructures. DNA origami can be used for creating nanoscale biosensors and constructing nanomaterials with specific geometries, e.g. to transport molecules by forming nanometer-sized containers (Figure 2.4 (a)). Similar applications exist on the micrometer scale for targeted drug delivery in volume-enclosing 3D structures. The pentahedral voxel made of polysilicon and permalloy (Figure 2.4 (c)) is controlled by magnetic and surface tension forces in water. Some examples of micrometer-scale structures include micro mirrors [34], acoustic

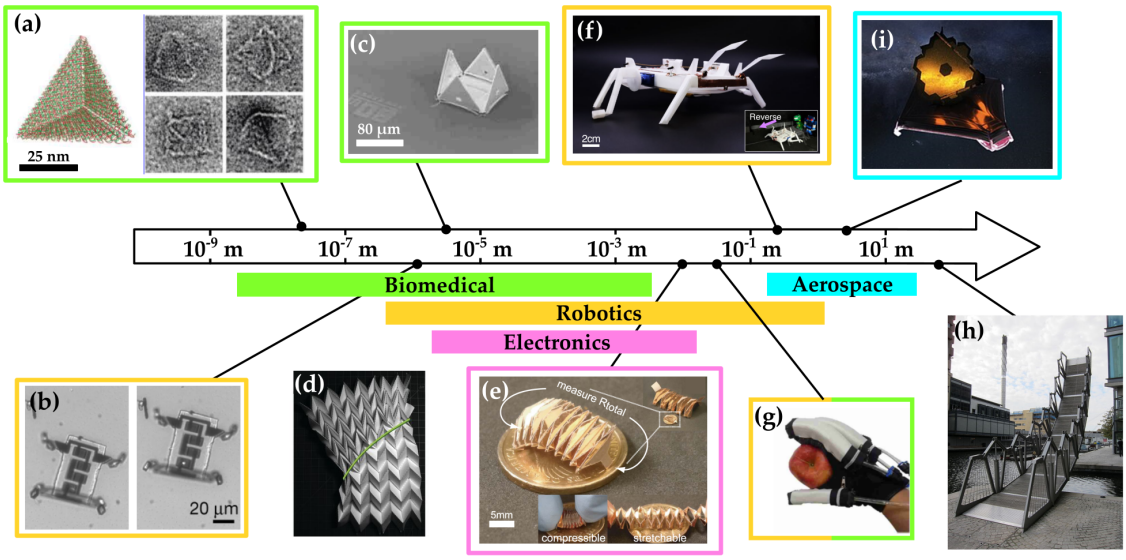

Figure 2.4.: Brief overview of origami applications at different length scales and various engineering fields: **(a)** DNA tetrahedron cage (adapted with permission from [25]. Copyright 2009 American Chemical Society); **(b)** Walking microscopic robot [26] (reproduced with permission from Springer Nature); **(c)**. Pentahedral voxel (adapted from [27]); **(e)** Stretchable and compressible resistor (adapted from [28]); **(f)** Untethered self-reversing crawling robot [29] (CC BY 4.0); **(g)** Pneumatic origami muscles for rehabilitation therapy [30] (©2020 IEEE); **(h)** The Rolling Bridge in London (by C.Bejarano CC BY 2.0); **(i)** James Webb Space Telescope (CC BY 2.0, Flickr).

waveguides [23], and the large field of metamaterials. Metamaterials are synthetic structures that are micro or nanostructured periodically, resulting in new mechanical, chemical, or electromagnetic properties. Certain origami patterns, such as miura-ori, induce programmable mechanical properties into these materials. Origami-based metamaterials in contrast to traditional ones enable to reprogram their stress-strain curves, exhibit negative Poisson's ratio, and show excellent energy-absorption capabilities [35].

Origami layouts can be combined with traditional MEMS and NEMS (nanoelectromechanical systems) manufacturing methods to create electronic components using planar lithographic fabrication with subsequent pop-up folding into 3D structures [36]. An example of this are S-RUMs (self-rolled microtubes), which consist of thin membranes made of semiconductors, dielectrics, or polymers, combined with a pre-stressed planar precursor. When detached from the substrate, cylindrical structures emerge [37]. This technique can be applied to various materials and can produce compact capacitors, inductors, and antennas. These components are commonly used for miniaturizing radio frequency integrated circuits, creating vertical ring resonators for 3D photonic integration, and making

batteries. Rogers et al. [38] provide a comprehensive overview of all relevant work in the field of MEMS and NEMS. Additionally, Figure 2.4 (e) showcases an origami-inspired foldable and adaptable resistor. These examples illustrate that the application of origami principles could revolutionize electronic design and manufacturing.
For this reason, significant advancements have been made in the field of robotics, particularly through the utilization of foldable origami-inspired structures [24], [39]. This has led to the emergence of a new research field known as *Robogami*, which focuses on creating self-folding robotic origami that can be reconfigured by multiple degrees of freedom [40], [41]. These robots consist of stiff parts and foldable joints. As illustrated in Figure 2.4, the applications of this technology are diverse, ranging from microrobots (b) to large-scale self-folding and self-sensing robots (f), and even exoskeletons made of origami muscles for the purpose of rehabilitation after injuries (g). In general, the primary applications for these small-scale origami-inspired structures or robots are in biomedicine. Further examples in this field are self-deploying stents [42] and endoscopes [43].
At the end of the size scale are applications in architecture and aerospace. For both areas, the advantage of compact storage and on-demand deployability is of interest. In architecture, in addition to the aesthetic effect, the structural stability has also proven to be an advantage. Examples in architecture are foldable temporary connecting tunnels [44], the deployable curtain wall of the Al Bahr Towers in Abu Dhabi for on demand tunable shading of sunlight or the *Rolling Bridge* in London (see Figure 2.4 (h)). For space applications, one well-known example in particular has attracted the attention of the general public in recent years. The space telescope developed by NASA, named after its former director James Webb, consists of a mirror structure with 18 beryllium hexagonal segments to collect light from distant objects (i). The entire structure was efficiently stored in the launch vehicle and deployed once in orbit over a period of several days.
The capability of *self-folding* is crucial for certain engineering applications where manual mechanical forces are not feasible, especially at very small or large scales or in remote inaccessible applications such as invasive biomedical devices and space structures. A self-folding structure folds autonomously and/or unfolds into a pre-determined shape without external mechanical intervention. The process of self-folding can be accomplished through various mechanisms, and one of the most important approaches is by using *active materials*. Active materials, also known as smart materials, are substances that can convert different forms of energy (thermal, chemical, electromagnetic) into mechanical work. The material's mechanical response (e.g. strain, stress) is typically one or more orders of magnitude larger than that resulting from conventional material behavior such as thermal expansion [45]. In addition, they are typically energy-dense, making them

excellent candidates for sensing and actuation applications. Examples of such materials include shape memory polymers (SMPs) and alloys (SMAs), hydrogels, liquid crystal elastomers, and magneto-active elastomers.

2.1.2. Folding Mechanisms

While mathematical models often exclude the impact of realistic properties (e.g. material thickness or stiffness), for the implementation of origami layouts in engineering applications one has to consider these effects. In practice, the sheet material and faces will bend, and folding does not exclusively occur by creasing. Figure 2.5 shows five different concepts that use active materials to achieve folding [46]. The shape of the folds can be categorized into *hinge-type* ((a)-(c)) or *bending-type* ((d)-(e)). Hinge-type origami structures are simplified as line segments on sheets that work as rotational hinges when folded. Three different hinge-type mechanisms allow for active folding: The extensional concept (a) involves an active rod or spring connecting the two faces. When activated, the rod changes its length, resulting in a folding motion. In the torsional concept (b) a torsional spring causes a twist in the hinge region, and the angle of the twist corresponds to the rotational motion of the faces. In the flexural concept, the active material connecting the two faces is pre-trained to a folded configuration and then deformed to an initial flat configuration. By applying the activation field, the active material takes its pre-set shape and guides the faces into the folded state.

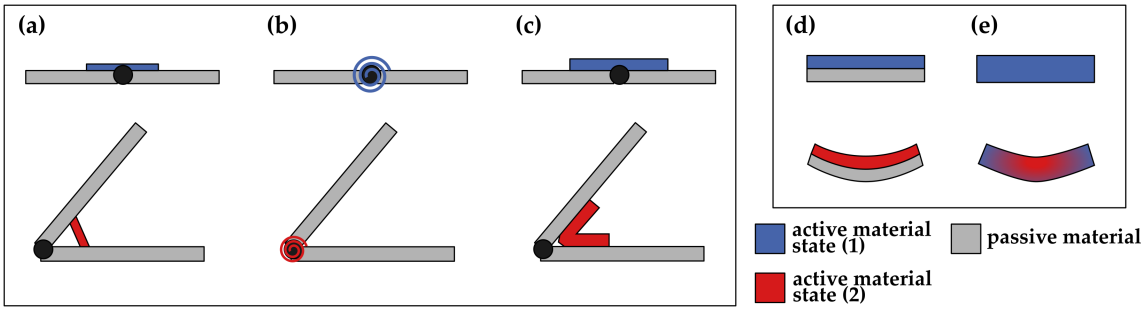

Figure 2.5.: Overview of different folding mechanisms adapted from [46]. Hinge type: **(a)** extensional, **(b)** torsional and **(c)** flexural. Bending type: **(d)** bilayer and **(e)** single layer subjected to graded driving field.

Other applications may not employ discrete hinge mechanisms and may be made of materials with larger thicknesses, or materials for which creased folds are not desirable and lead to delamination or damage. For these materials, folding is achieved by bending lo-

calized regions. These bending-type hinges can be classified as bilayer (d) or single-layer graded (e), both made of active materials. The bilayer type is a laminate of active and passive layers. When the active layer deforms under the stimulus of the activation field, the difference in expansion or contraction compared to the passive layer generates a bent. For the single-layer type, the driving field (e.g. temperature) has a gradient that induces a distribution of actuation strain across the thickness of the sheet. This allows for folding in both directions, depending on the applied field gradient.

As proposed by Peraza-Hernandez et al. [46], depending on the active material chosen for the self-folding structure, there are three ways for control:

1. Direct coupling by applying fields that induce actuation strain without modifying the material and nano-structure (e.g. piezoelectric effect where the electric field E increases the actuation strain or thermal expansion).

2. Direct coupling by applying fields to modify the micro- and nano-structure of the material (e.g. apply a temperature to induce a phase-transformation, such as in shape memory materials).

3. Indirect coupling and applying fields that modify certain material properties (e.g. use temperature to change the material stiffness [47]).

The relevant design criteria for the choice of active materials as folding actuators are: the actuation strain, actuation stress and the capability of generating and/or maintaining the desired activation field at the chosen scale [46]. To compare different active materials along those properties, fold-specific characteristics (bending moment, folding angle, and radius of curvature) should be mapped. Figure 2.6 gives an overview of common active materials and their mechanical performance.

For the case of bending, the minimum allowable bending radius of curvature R is related to the material thickness t and its maximum actuation strain ε_{max}:

$$\frac{R}{t} = \frac{1 - |\varepsilon_{max}|}{2|\varepsilon_{max}|} \tag{2.1}$$

This equation allows to relate the actuation strain to folding metrics. It is derived and further discussed in section 4.2. The top axis in Figure 2.6 provides a quantitative evaluation of the behavior of different materials under bending load.
Ceramic-type active materials may not be suitable for self-folding applications, due to

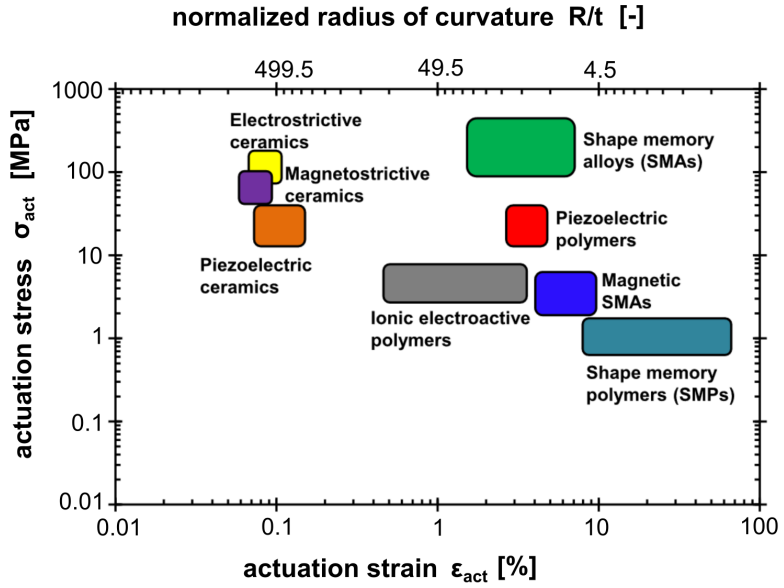

Figure 2.6.: Overview of different active materials and their typical ranges of actuation strain and actuation stress as adapted from [46].

their limited bending radii. While SMPs allow for large actuation strains, they show the lowest actuation stress. On the other hand, SMAs have proven to be a good compromise of high actuation stress and reasonable small bending radii.

2.2. Shape Memory Alloys

Shape memory alloys (SMAs) are a fascinating class of materials that are able to "remember" a pre-defined shape and, when deformed, return to that original shape when the temperature is increased. Shape recovery by heating can occur even under high loading. SMAs show highest actuation energy densities (product of actuation strain and actuation stress) among all active materials, including piezoelectric or electroactive materials [48]. Their excellent scaling behavior of their mechanical properties upon miniaturization makes them particulary attractive for sensor and actuator applications in micro-dimensions [49]. Other important features of SMAs are their biocompatibility, low corrosivity and stiffness compared to other active materials. In recent years, many applications arose in the fields of robotics, aerospace and biomedical engineering. The most common examples of SMA alloys are based on near-equiatomic TiNi (Ti-Ni-X), also known as Nitinol. Other typical compositions are Cu-based (Cu-X) or ferrous alloys (Fe-X).
In this section, the characteristics of the martensitic transformation, and the resulting

thermomechanical mechanisms (shape memory effect and superelasticity) are described. Here, the focus is on TiNi-based materials.

2.2.1. Martensitic Transformation in TiNi Alloys

The thermoelastic martensitic transformation involves a reversible change in crystal structure without diffusion of atoms [50]. The phase transformation takes place between a high temperature parent phase, called austenite, and a low temperature phase, called martensite. As shown in Figure 2.7(a), austenite has typically a highly symmetric body-centered cubic (BCC) lattice structure of B2-type. For TiNi alloys the martensite phase is usually of monoclinic (B19') type (see Figure 2.7(c)). It is three-dimensionally close packed and of lower symmetry. Depending on material composition and heat treatment, TiNi alloys do also show an additional intermediate phase which takes place before the martensitic transformation. This presumed rhombohedral phase (denoted as R-phase) can be formed by elongation of the <111> directions in the B2 structure (Figure 2.7(b)). The R-phase transformation appears for TiNi alloys with high Ni content, when annealed at temperatures below recrystallization after cold working and by addition of ternary elements [51, pp. 74-75].

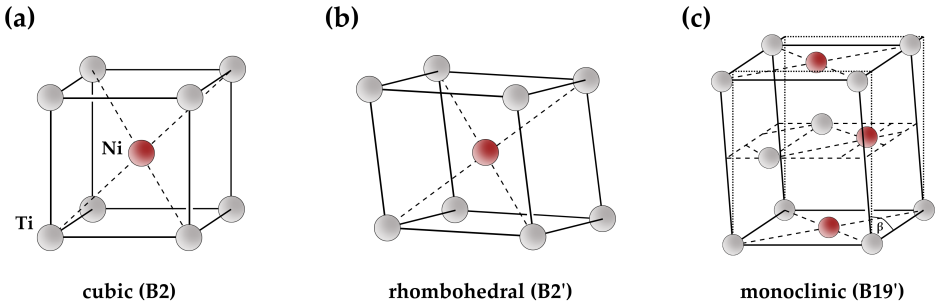

Figure 2.7.: Unit cells of the crystal structures of austenite **(a)**, R-phase **(b)** and martensite phase **(c)**. Adapted from [51, pp. 75]

The martensitic transformation is a first-order transformation that proceeds through nucleation and growth. Austenite transforms into the martensite phase by cooperative motion of atoms and creates a habit plane between the two lattices. The mismatch of the lattice structures introduces large strains at the interface that can be released by either slipping or twinning. These mechanisms are called lattice invariant shear, since the overall symmetry or orientation of the crystal lattice is not changed. The dominant lattice invariant shear of TiNi is twinning which is reversible. In general, there are up to 24

different martensite variants that have the same crystalline structure but different orientations. If one variant forms from austenite upon cooling, the formation of other variants is required, to minimize the total strain. By this so-called self-accommodation of martensite variants the macroscopic shape of the material is maintained [50, pp. 11-21].
In the nucleation of martensite from austenite the Gibbs free energy G is decisive in determining which variant is formed. The material tends to transform in the direction that minimizes the free energy. Written as a thermodynamic potential for both phases, $G^{A/M}$ depends on the inner energy $U^{A/M}$, the strain tensor $\boldsymbol{\varepsilon}^{\boldsymbol{A/M}}$ and the entropy $S^{A/M}$. The two state variables are the stress tensor $\boldsymbol{\sigma}(\boldsymbol{\varepsilon}^{\boldsymbol{A/M}})$ and the temperature T [48, pp. 127-129]:

$$G^{A/M} = U^{A/M} - \boldsymbol{\sigma}(\boldsymbol{\varepsilon}^{\boldsymbol{A/M}}) : \boldsymbol{\varepsilon}^{\boldsymbol{A/M}} - S^{A/M}T \tag{2.2}$$

The Gibbs free energy G for all phases is a function of temperature and is schematically shown in the stress-free condition for austenite and martensite in Figure 2.8(a). T_0 represents the thermodynamic equilibrium temperature between the two phases at which both phases have the same free energy. At lower temperatures, martensite is more stable, whereas in the higher temperature region the free energy of the austenite phase is lower. For the nucleation of martensite, the driving force $\Delta G^{A\rightarrow M} = G^M - G^A$ is required [50, pp. 22-23]. This change in Gibbs energy upon the martensitic transformation decomposes into a chemical energy term ΔG_c associated with the structural change from austenite to martensite, a surface energy term ΔG_s and an elastic energy term ΔG_e:

$$\Delta G = \Delta G_c + \Delta G_s + \Delta G_e \tag{2.3}$$

The non-chemical energy term $\Delta G_{nc} = \Delta G_s + \Delta G_e$ is equally large as ΔG_c. Therefore, supercooling is necessary for the martensitic transformation. Only by supplying additional driving force, e.g. by cooling, the growth of martensite continues because of the elastic energy around martensite. For this reason, the phase transformation takes place in a certain temperature window between martensite start (M_s) and martensite finish temperature (M_f). Similarly, for the reverse transformation, from austenite to martensite, superheating is required and the phase transformation is completed between austenite start and austenite finish temperature, denoted as A_s and A_f in the further course.

One method to derive the martensitic transformation temperatures are differential scanning calorimetry (DSC) measurements. For each phase transformation in the cooling or heating cycle, latent heat is released or absorbed, leading to a peak in the heat flow curve (see Figure 2.8(b)). The onset and endset of the peak mark the start and end of the phase transformation. Upon cooling, the austenite phase transforms between M_s and M_f,

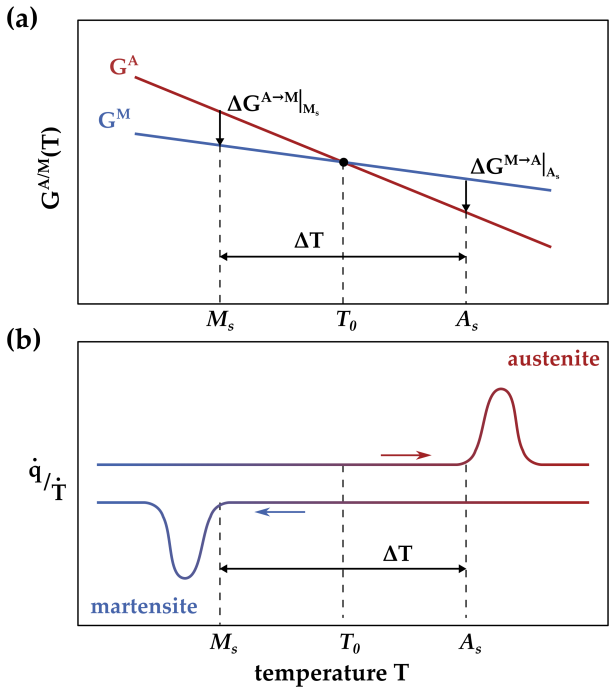

Figure 2.8.: (a) Schematic of Gibbs free energy of martensite G^M and austenite G^A. **(b)** Schematic of the corresponding DSC curve. Adapted from [50]

whereas the reverse transformation takes place between A_s and A_f. The temperature hysteresis between the martensitic and reverse transformation $\Delta T = \frac{1}{2}(A_s + M_s)$ is usually in the range of 20 to 50 K for TiNi alloys. Further details on DSC measurements are provided in section 3.2.1. Other methods to characterize the phase transformation temperatures are temperature dependent resistance measurements.
The two unique properties of SMAs, the shape memory effect (recovery of the memory shape) and pseudoelasticity (large nonlinear recovery of strain upon unloading), are related to the temperature- and stress-induced martensitic transformation. They will be discussed in the following sections.

2.2.2. Shape Memory Effect

The one-way shape memory effect (SME) is the phenomenon of shape recovery in a temperature cycle. This cycle is depicted in Figure 2.9. Above A_f, the SMA is in its austenite phase (1) and has its predefined shape. This so-called memory shape can be imprinted by annealing at high temperature. When the material is cooled from austenite state, the alloy undergoes the martensitic transformation and grows self-accomodated martensite variants without macroscopic shape change. For sake of simplicity, only two of those vari-

ants are represented in the twinned configuration and stress-free state in Figure 2.9 (2). The twin boundaries are mobile under stress and thus, the twinning works as deformation mechanism in the martensitic state. When applying an external force, the twinned martensite M' is initially deformed elastically and upon further loading, de-twins along the twin boundaries. One single martensite variant forms that is oriented in the most favorable orientation to the applied stress. This rearrangement of martensite variants is associated with a plateau region in the stress-strain curve (see Figure 2.9(b)). The end of the detwinning process is marked by a sudden increase in the slope. If the external force is completely removed, the strain decreases by elastic unloading of detwinned M (3). The large quasi-plastic deformation remains even after unloading and represents the transformation strain ε_t. In order to reset the memory shape, the material is heated and undergoes the reverse transformation between A_s and A_f. Thereby, the starting point of the cycle (1) is reached again. The material does not remember its previous deformation; therefore, this heating-induced effect is also called one-way shape memory effect.

Loading beyond the elastic limit of M would introduce irreversible slip deformation and defects in the crystal structure, as in conventional metals and alloys without shape memory characteristics and should be avoided in applications.

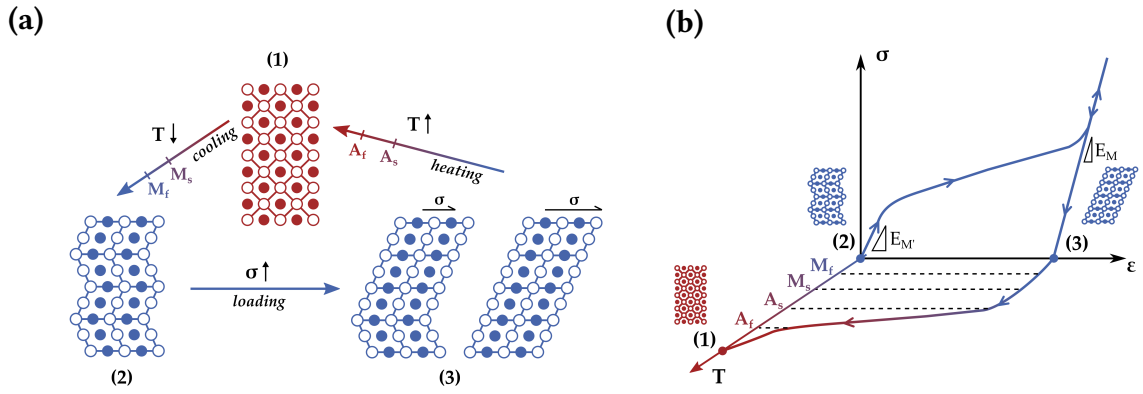

Figure 2.9.: Mechanism of the shape memory effect. **(a)** Change of crystal lattices. Schematic is adapted from [51, p. 82]. **(b)** Characteristic curves of the shape memory effect in the temperature-stress-strain diagram. [48, p. 11]

The SME is mainly used for actuators coupled with a biasing load or most commonly for biomedical stents. TiNi based materials undergoing the direct phase transformation from A to M allows for large macroscopic strains of up to 10% depending on the orientation. The ε_t of R-phase transformation is much lower due to the smaller changes in the detwinning of the rhombohedral lattice [52].

2.2.3. Pseudoelasticity

The effect of pseudoelasticity (PE) takes place at temperatures above A_f where the stress-induced martensitic transformation is initiated by applying an external load above the critical stress (Figure 2.10(a)). The de-twinned martensite state M is directly reached (2). A sudden increase in slope indicates the completion of the martensitic transformation and the elastic loading of fully detwinned martensite (3). Upon unloading, the alloy recovers the original shape without heating. The martensitic and reverse transformation during a complete pseudoelastic cycle results in a hysteresis that represents the dissipated energy.

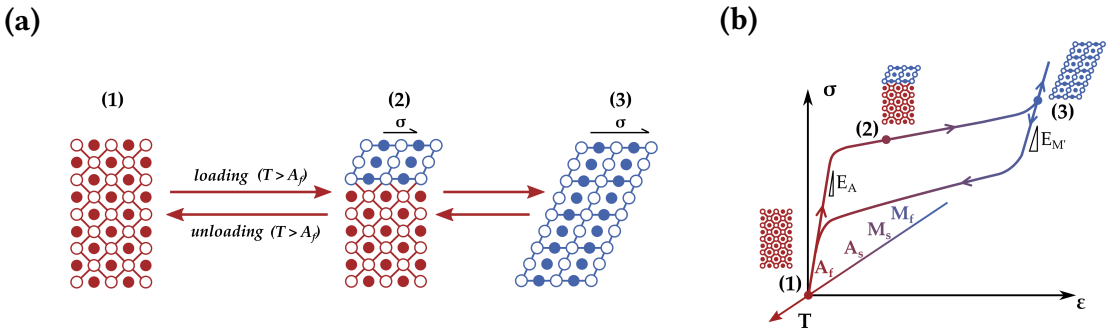

Figure 2.10.: Mechanism of pseudoelasticity. **(a)** Change of crystal lattices by stress-induced martensitic transformation. Adapted from [50, p. 37] **(b)** Characteristic curve of pseudoelastic behavior in the temperature-stress-strain diagram. Adapted from [48, p. 10].

In literature, the described phenomenon is often refered to as *superelastic effect* but superelasticity is a side phenomenon of pseudoleasticity. Both effects, the SME and PE are associated with the same martensitic transformation resulting in the same amount of shape recovery. For pseudoelastic material behavior, the transformation strain ε_t corresponds to the width of the pseudoelastic plateau.

As stated in equation 2.2 besides temperature, also the stress state of the material is relevant for the Gibbs energy. As a shear-like mechanism, the martensitic transformation is assisted by any shear stress acting on the habit plane. The Clausius-Clapeyron relationship describes the effect of a uniaxial stress σ on the martensitic transformation as follows:

$$\frac{d\sigma}{dT} = -\frac{\Delta S}{\varepsilon_t} = -\frac{\Delta H}{\varepsilon_t T} \propto C_{A/M}, \tag{2.4}$$

where ε_t denotes the transformation strain, ΔS the entropy of transformation per unit volume, and ΔH the enthalpy of transformation per unit volume. Above M_s, the critical stress to initiate the martensitic transformation increases approximately linearly with the temperature.

As shown in Figure 2.11, the derivation of $C_{A/M}$ and the critical transformation stresses allows to define all phases in a stress-temperature diagram and the respective phase transitions that are marked by dashed lines.

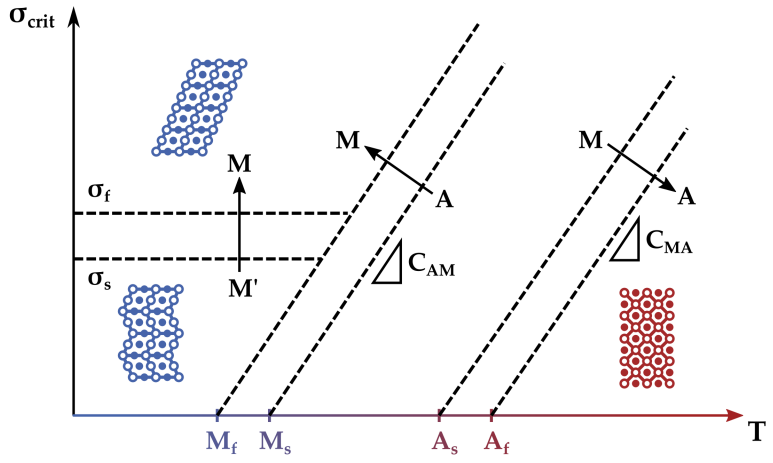

Figure 2.11.: Schematic of a typical stress-temperature and phase diagram of SMAs. Adapted from [48, p. 10].

Furthermore, a so-called two-way shape memory effect can be realized in shape memory materials. It can be observed in specimens that received a thermomechanical treatment producing microstresses in the austenite phase [53]. The microstresses affect the nucleation and growth of martensite, favoring certain martensite variants to form preferentially. Therefore, two "memory shapes" occur, one upon cooling and one according to the one-way shape memory effect.

2.3. Magnetic Materials and Effects

All magnetic materials have unique responses to magnetic fields. The primary types of magnetic materials include ferromagnets, ferrimagnets, paramagnets, diamagnets, and antiferromagnets. Their properties differ based on the ordering and interaction between the dipole moments of the atoms and ions comprising the magnetic materials. Figure 2.12 (a) shows these different types of magnetic materials schematically.

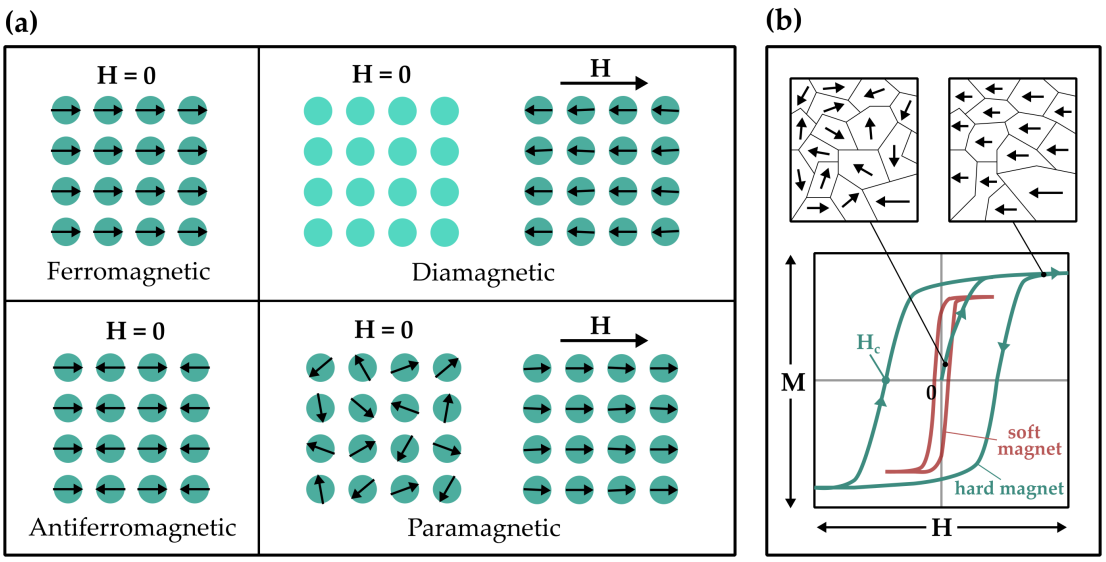

Figure 2.12.: **(a)** Schematic of the behaviour of magnetic dipole moments in different types of magnetic materials with and without external magnetic field H, adapted from [54] **(b)** Schematic of a typical magnetization curve generated by an applied magnetic field and reorientation of magnetic domains.

2.3.1. Ferromagnetism

As depicted in Figure 2.12 (a) ferromagnetic materials consist of small regions where atomic magnetic moments are aligned parallel to each other, so-called magnetic domains. The magnetization process of ferromagnetic materials under the influence of an applied field involves two related phenomena: the movement of domain walls and rotation of magnetic moments. Domains that are favorably aligned with the external applied field experience growth at the expense of unfavorably aligned domains [55]. The resulting magnetization field $\boldsymbol{M}$ of a solid is defined as

$$\boldsymbol{M} = \frac{d\vec{m}}{dV}, \tag{2.5}$$

where $d\vec{m}$ is the elementary magnetic moment, and dV the infinitesimal volume element. Figure 2.12 (b) depicts schematic magnetization curves of a ferromagnetic material and illustrates the impact of its initial magnetization on the magnetic domains. Compared to other types of magnetic materials a large magnetization is obtained on application of a much smaller field. The magnetization saturates and removal of the field does not lead to its unmagnetized state but results in a so-called remanent magnetic field $\boldsymbol{Br}$ and magne-

tization hysteresis. The reversal field required to reduce the magnetic induction to zero is called coercivity $\boldsymbol{H_c}$ [56, pp. 17-19].
Hard magnetic materials have wide hysteresis loops and high coercivity, requiring more energy to magnetize and demagnetize (see green hysteresis curve). These materials, such as neodymium magnets (typically NdFeB) or samarium-cobalt magnets, are used for permanent magnets or magnetic data recording. On the other hand, soft magnetic materials can be easily magnetized and demagnetized due to their low coercivity (see red hysteresis curve). They are used in transformer cores, inductors, and electromagnets. Some examples are silicon steel (electrical steel) and soft iron.

2.3.2. Curie Temperature

At room temperature, there are only three ferromagnetic metals: iron, nickel, and cobalt. This is because substances require a high atomic magnetic moment in order to exhibit ferromagnetism. Additionally, the energy needed for the atoms to align themselves in the same direction must be significantly greater than the energy of thermal agitation k_BT, which causes random movement and disrupts the ordering of magnetic domains [57, p. 155]. This results in the paramagnetic state, where magnetic moments are asymmetrical and non-aligned in the absence of a magnetic field. When a magnetic field is present, the magnetic moments temporarily align parallel to the field (refer to Figure 2.12 (a)), creating a magnetic field.
The transition from ferromagnetic to paramagnetic state occurs at the Curie temperature, T_c. This transformation is of second-order and is not associated with any latent heat or hysteresis. The Curie temperature of iron, for example, is $T_c = 1043\,K \approx 770\,^{\circ}C$.

2.3.3. NiMnGa Heusler Alloys

Manganese possesses a larger magnetic moment compared to iron, but its interaction energy does not lead to the alignment of moments required for ferromagnetism. However, when manganese atoms are integrated into the crystal structure of an alloy containing the two other paramagnetic elements, copper and aluminum, the conditions allow for the magnetic interaction to align the moments of the manganese [57, p. 156]. This type of alloy, known as the Heusler alloy Cu_2MnAl, was first described by Carl Heusler in 1903 and exhibits ferromagnetic properties up to 710 K.
Generally, Heusler alloys are ternary intermetallic compounds with the composition X_2YZ, where X and Y are transition metals and Z belongs to the p-block (e.g. Al, In, Sb, Ga). Another famous Heusler alloy is the Ni_2MnGa system. The stoichiometric,

fully-ordered $Ni_{50}Mn_{25}Ga_{25}$ crystal structure is based on four cubic face-centered sublattices, which are shifted by ¼ of the unit cell, a so-called $L1_2$ structure [58]. This corresponds to the highly symmetrical austenite phase shown in Figure 2.13 (a).
Figure 2.13 (b) shows the magnetization curve depending on the temperature of $Ni_{48}Mn_{31}Ga_{21}$. Above the Curie temperature T_c (365 K), the material is paramagnetic. During cooling, the austenitic phase forms first, which is ferromagnetic and leads to an increase in magnetization. On further cooling below 300 K, the material undergoes a first-order phase transition to martensite with twinning between different variants. The martensitic structure is also ferromagnetic, but the saturation magnetization decreases during the phase transition starting from austenite. The martensitic transition is completely reversible. Unlike the second-order Curie transition, additional thermal energy is required here. Consequently, there is a hysteresis between the martensitic transformation and its reverse transformation upon cooling.

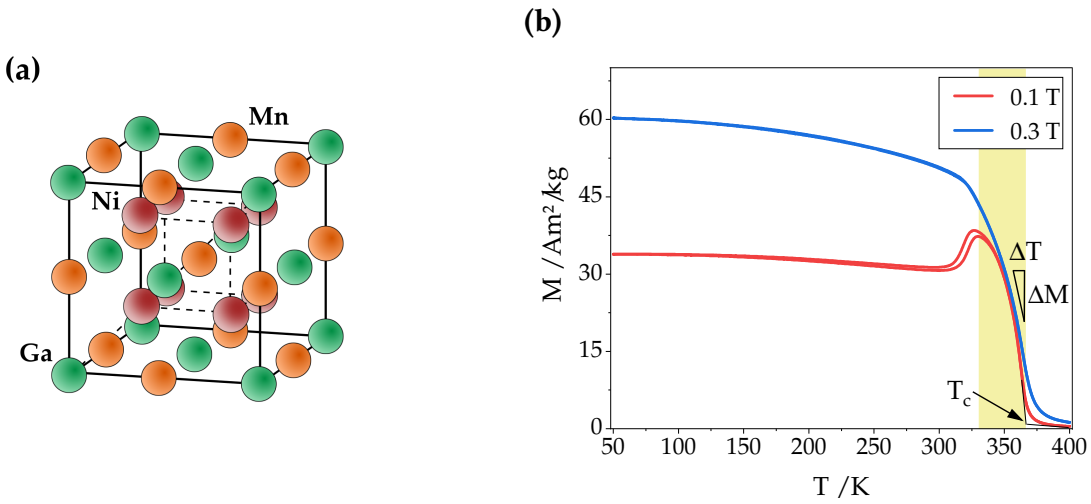

Figure 2.13.: (a) NiMnGa unit cell of cubic austenite structure ($L1_2$), adapted from [58]. **(b)** Magnetization of sputter-deposited $Ni_{48}Mn_{31}Ga_{21}$ thin film as a function of temperature for two different fields $\mu_0 H$.

Using $Ni_{2+x}Mn_{1-x}Ga$, it was shown that T_c can be lowered by increasing the Ni content [59]. The additional alloying with Cu and the resulting extension to a quaternary alloy NiMnGaCu also enables a shift of the Curie transition towards room temperature and improvement of the thermomagnetic properties [60]. Especially when used in thermomagnetic generators, a low T_c with a high $\Delta M/\Delta T$ ratio is important for low operation temperatures, high operation frequencies and large power output.

2.4. State of the Art of SMA-based Folding Actuators

The use of SMA components in folding actuators combines the outstanding mechanical properties of this material, such as high energy density and high rigidity, with the possibility of thermal activation. For this reason, there are already a large number of publications in this field.

Generally, these actuators use the one-way shape memory effect, and the reset can be achieved by various mechanisms. The simplest but also most inconvenient option is manual unfolding by hand or another external mechanical aid to return the actuator to its initial state. Another solution is the coupling between the SMA component and a bias spring. This mechanism is shown schematically in Figure 2.14 (a). By connecting a spring in parallel, the SMA component is in a pre-strained state (1). If the SMA is activated by heating (2), the actuator folds in the desired direction if the austenite phase has a higher stiffness than the bias spring. When the thermal supply is switched off and the martensitic phase transformation can take place, the spring force ensures the return to the starting position (3).

A comparable result is obtained by using a minimum of two SMA components arranged antagonistically (see Figure 2.14 (b)). In the initial state (1), at least one component must be pre-stretched. By activating this deformed SMA, work can be performed on the second component and a movement is generated due to shape recovery (2). By sequentially heating (3), the actuator can be reset or folded bi-directionally.

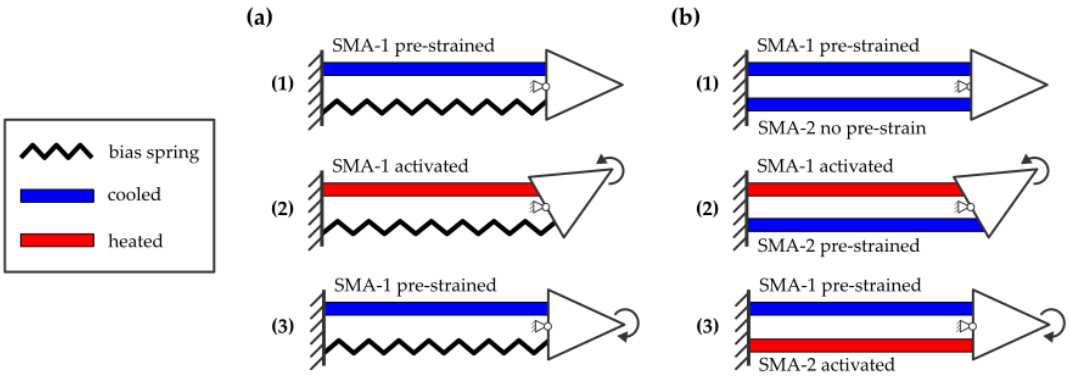

Figure 2.14.: Two mechanisms of reversible and bi-directional SMA folding actuators: **(a)** SMA and bias spring, **(b)** Two antagonistic SMAs. Adapted from [61].

In principle, it is also possible to use only one SMA component if it has the two-way effect and alternates between the martensite and austenite memory shapes [62].

The use of an SMA actuator requires compatible heating and cooling methods. In the

literature, there are usually only two different heating options: With Joule heating, the current is passed directly through the SMA component. This method is simple and allows control over the folding angle. To achieve the transformation temperature (A_f), a sufficiently high current is required, which scales with the diameter of the SMA element. This method is only applicable for SMA wires with a diameter below 1 mm to keep the current below 8 A [63]. The second heating option involves the use of an additional heater comprising resistance lines. A current is passed through the resistance lines, and the heat generated is then transferred to the SMA element. This particular method is valuable in applications where direct electrical contact with the SMA element is not feasible or when heating large volumes.
Most SMA actuators have no additional devices for cooling and rely on natural convection. Forced convection by means of a fan can be used to increase the actuation frequency.

In the literature, various geometric shapes of SMA elements used in folding actuators have been explored, including wires, springs, and foils. Among these, SMA wires are particularly noteworthy for their ease of manufacturing and ready availability in the commercial market, contributing to their wide utilization across different applications. Straight wires can only be used in tension to achieve high forces due to their limited ability to withstand compression. With recoverable strains below 8 %, the total length of the SMA wires must be proportionally longer to obtain the desired stroke length for the application. To circumvent the need for larger actuators, wires can be coiled to generate a larger output stroke within the current dimensions. The resulting SMA spring can attain higher rotations at the expense of torque output.
Some types of folding actuators are powered by SMA sheets, strips, or films. In these actuators, the primary motion is bending, resulting in the local distribution of tensile and compressive strains on both sides of the SMA element. The rotational motion occurs around an axis defined by the structural deformation, rather than involving a rotation between separate elements. SMA bending beams can provide similar rotational angles and torques when compared to normal-strain-driven actuators, but they enable size reduction of the overall actuator design.
In the following, a variety of concepts for creating SMA-based folding actuators is presented. These concepts utilize and combine the principles mentioned above.

Hawkes et al. significantly advanced SMA-based self-folding origami with a "programmable sheet" [2]. As shown in Figure 2.15 (b), a composite sheet is fabricated by laser machining consisting of triangular glass-fiber segments and elastomeric folding

creases. Laser-structured 100 µm thin TiNi foils serve as folding actuators. The shape and heat treatment of the foils allow for four possible folds within the SMA element: one central bending fold and three distal clamping folds. Thereby, folding between 0 and +180° is achieved. The three "feet" of the SMA structures are inserted into through holes within the triangular tile structures and soldered to copper traces. The traces of a power circuit interconnect several SMA actuators forming an actuator group. When leading across a folding crease, the copper traces are patterned to allow for stretching in the bent state. Additionally, hard magnets are incorporated into each triangular segment. Depending on the desired 3D shape, optimal actuator groups are designed and a folding sequence is programmed. To obtain the final 3D shape, one or more groups are Joule heated until the folds are complete and the magnets latch, and the next group of actuators is activated. Figure 2.15 (b) depicts the different stages of folding into a boat shape. With the given pattern, the folding into a plane following a different folding sequence, is also possible. The size of the segments are 1 cm wide, resulting in a total size of 4 x 4 cm². Unfolding has to be performed manually before re-programming and folding into a new shape.

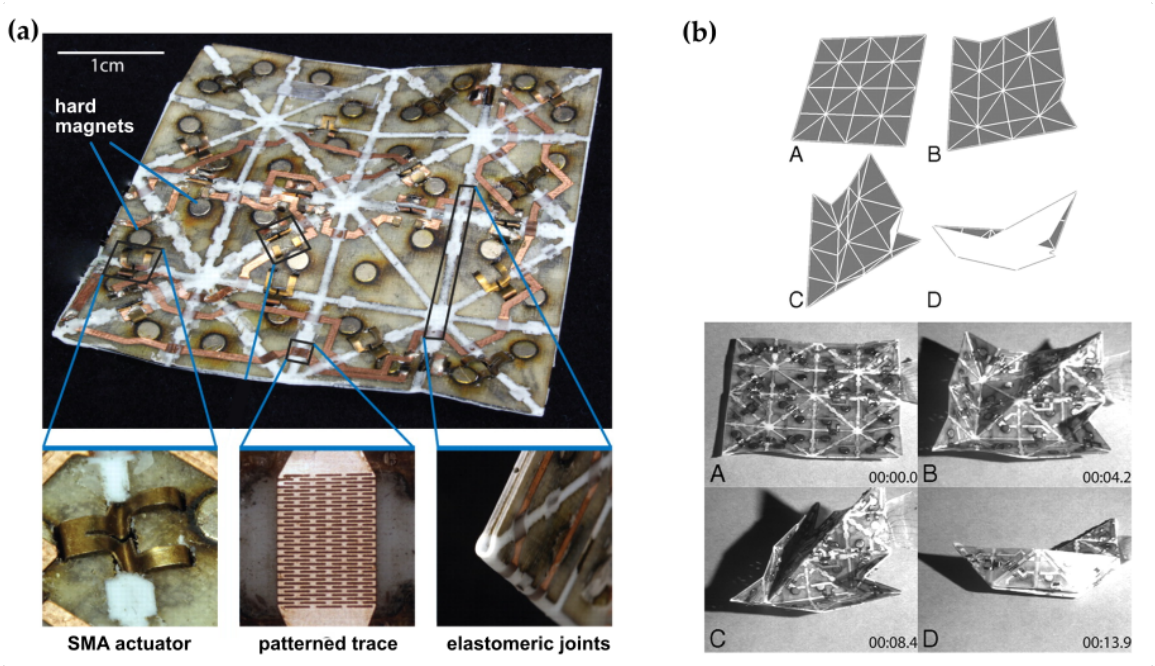

Figure 2.15.: **(a)** Programmable sheet consisting of TiNi folding actuators, hard magnets and flexible patterned traces crossing the elastomeric joints. **(b)** Folding sequence of a boat shape. Images adapted from [2]. Copyright (2010) National Academy of Sciences.

The concept of using SMA foils as hinge components has been further developed to achieve bi-directional folding. Paik et al. introduced a two-axis SMA folding actuator that produces two opposing motions [64]. As shown in Figure 2.16 (a), the actuator is composed of a 100 µm thin NiTi actuator and an external heating element for localized activation. The NiTi foil is laser-machined and heat-treated in an annealing jig to create two folding regions (curved segments). The external heater is made of a composite of a structured conductive Ni-based layer (40 µm thick) and a flexible polyimide layer (35 µm thick). It is laser-machined into a layout with three electrodes and laser-welded on the NiTi substrate (Figure 2.16 (b)). By individually heating the two folding regions, the actuator achieves a bi-directional bending motion (Figure 2.16 (c)). At a maximum heater temperature of 85 °C on one side of the actuator, it allows for folding between 0° and +180° within 2 s. At a total power consumption of 92 mW, the folding actuator produces a torque of 4×10^{-3} Nm. The additional introduction of feedback control using flexible carbon ink sensors has made it possible to develop the first *Robogami* system that can crawl with four legs [40].

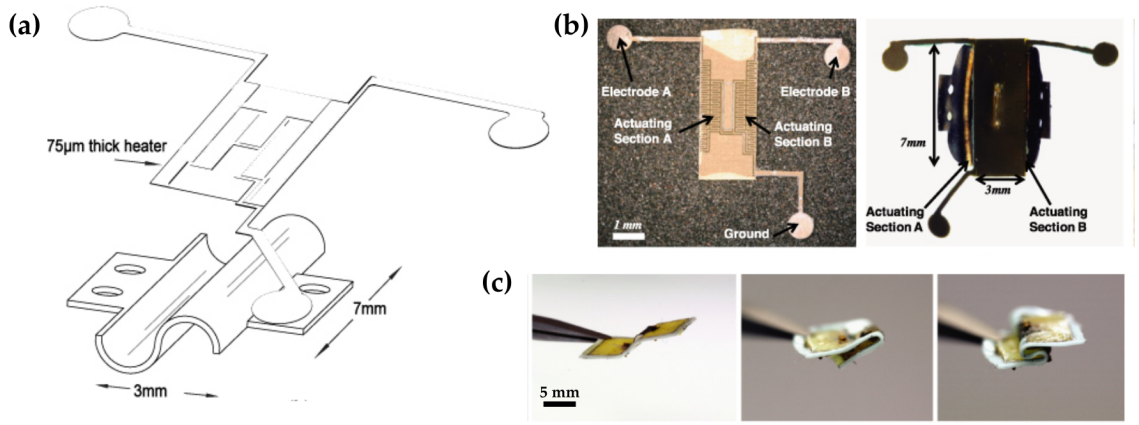

Figure 2.16.: Bi-directional SMA folding actuator: **(a)** Heater and SMA actuator dimensions. **(b)** Patterned Iconel heater with three electrodes before and after mounting to an actuator. **(c)** Bi-directional actuator modes: before actuation, single axis activated and both axes activated. © IOP Publishing. Reproduced with permission from [64]. All rights reserved.

Foil-based SMA actuators achieve folding using the flexural type, as introduced in Figure 2.5. Alternatively, SMA wires in a prestretched state can be used as a connection between two faces (extensional type). When a thermally induced shape recovery occurs, it results in a folding motion. Peraza-Hernandez et al. present a concept

for a self-folding sheet, consisting of a woven mesh of SMA wires separated by a compliant elastomer layer [65]. Figure 2.17 (a) depicts the three layers. The bottom mesh is shifted relative to the top mesh in both planar directions. The heated region is representing a localized heater that induces the martensitic transformation and thus folding actuation along the highlighted folding line. Unless restricted mechanically, the sheet returns to its flat state upon cooling. Figure 2.17 (b) shows the initial and fully deformed configuration of an optimized sheet design and the distribution of temperature and martensite volume fraction. After cooling and resetting, the sheets are fully re-programmable and could fold into a variety of different patterns. But due to the bimorph effect the smooth folds are limited in radius of curvature and bending angles.

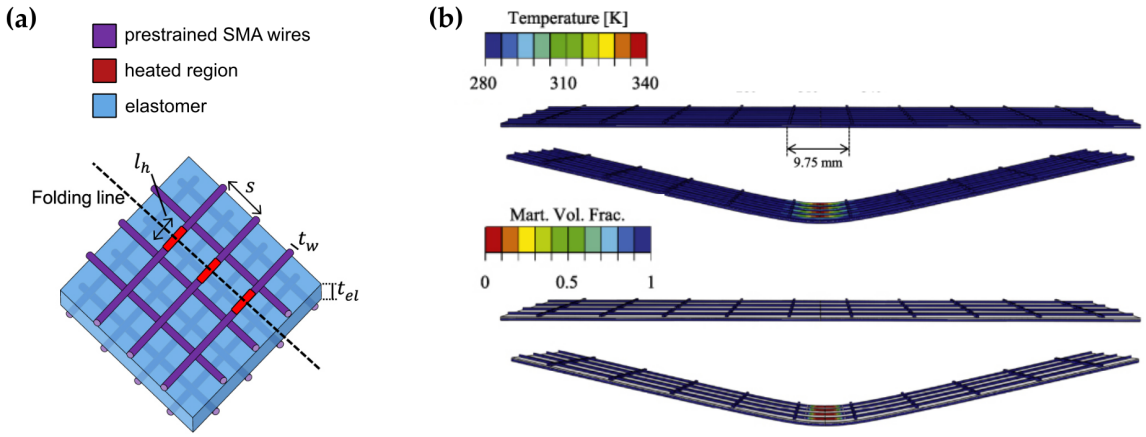

Figure 2.17.: Concept for an SMA-based reprogrammable self-folding sheet. **(a)** Schematic of the mesh design. **(b)** Temperature and martensitic volume fraction contour plots of initial and final configuration obtained by finite element analysis © IOP Publishing. Reproduced with permission from [65]. All rights reserved.

Torsional actuators based on SMA wires can provide larger bending angles when a compliant layer does not mechanically constrain its motion. Shin et al. present a modular concept based on arc-shaped SMA wires with a thickness of 250 µm [66]. As shown in Figure 2.18 (a), one module consists of an actuator unit (red) that is rigidly attached to two supporting elements (blue). In the initial state (I), the SMA wires are in a deformed martensite phase. Upon heating the SMA restores its original linear shape, contracts and generates a torque (state II). Cooling extracts the actuating unit while keeping its previous heated shape in state III. Parallelly connected into an array of 28 SMA wires, as shown in Figure 2.18 (b), increases the force/torque capacities. The respective actuated and unac-

tuated spring constants are k_a = 0.14 Nm/rad and k_u = 0.04 Nm/rad. Folding from the flat position (0°) to 80° takes less than 1 s for input currents of 0.8-1.2 A. The single modular torsional actuator is further extended in a serial connection, consisting of eight actuating units (AUs) and nine supporting elements. Figure 2.18 (c) displays the resulting modular torsional actuator, which can be used for a soft robot to transform its shape and perform rolling locomotion.

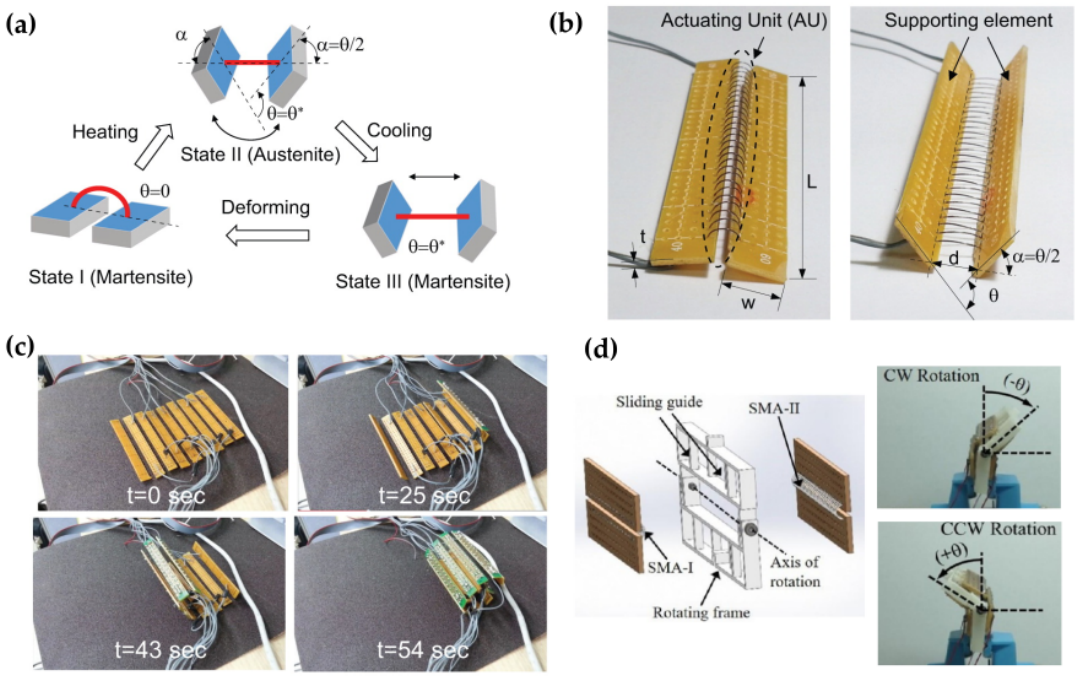

Figure 2.18.: Modular torsional actuator using SMA wires: **(a)** Actuator states based on thermo-mechanical properties, **(b)** Prototype comprising an SMA actuating unit (AU) and two supporting elements in deformed state I (left) and cooled state III (right), L = 80 mm, w = 11 mm. **(c)** Serial connected modular actuator transforming from a linear to a circular posture in time stamps. Copyright © 2015 by Sage Journal [66]. Reprinted by Permission of Sage Publications. **(d)** Bi-directional torsional actuator based on a rotating frame and the combination of two antagonistic single torsional actuators. Angular displacement is achieved in clockwise (CW) and counter-clockwise (CCW) direction (reprinted from [67], with permission from Elsevier)

For bi-directional actuation two unidirectional AUs, e.g. SMA-I and SMA-II, are paired in an antagonistic way [67]. As shown in Figure 2.18 (d), the supporting elements of SMA-I and SMA-II are attached onto a rotating frame. The upper supporting units are attached to a sliding guide to accomodate deflections of both activated and deactivated

AUs. Clockwise and counterclockwise rotational motion is demonstrated between -50° and +50° (see images in Figure 2.18 (d)).

Zheng et al. developed a modularized paper actuator based on SMA wires that paves the way toward fabrication of origami soft actuators (OSA) [68]. As schematically shown in Figure 2.19 (a), the OSA consists of three main components: SMA wires that generate the actuating force, printed heaters for SMA activation, and elastic paper origami structures that provide recovery force. Prepunched craft paper is folded into a stiff origami structure into which the SMA wires are threaded. The paper-based flexible heater is fabricated by screen-printing and wrapped around the SMA wires. Figure 2.19 (b) shows the change in bending angle for different voltages applied to the heater. The bending angles of the OSA are 237.1° and 223.7° for 4.5 V and 6.5 V, respectively. After turning of, the OSA recovers to its initial angle of 245° within 96 s. For a voltage of 8.5 V, the OSA bends up to 173.4°, thus reaching a total angle difference of 71.4°. However, the OSA does not return to its initial angle upon cooling because the origami structure does not provide enough flexural rigidity for recoverability. It is shown that the recoverability of the folded OSA is two times higher compared to a flat structure.

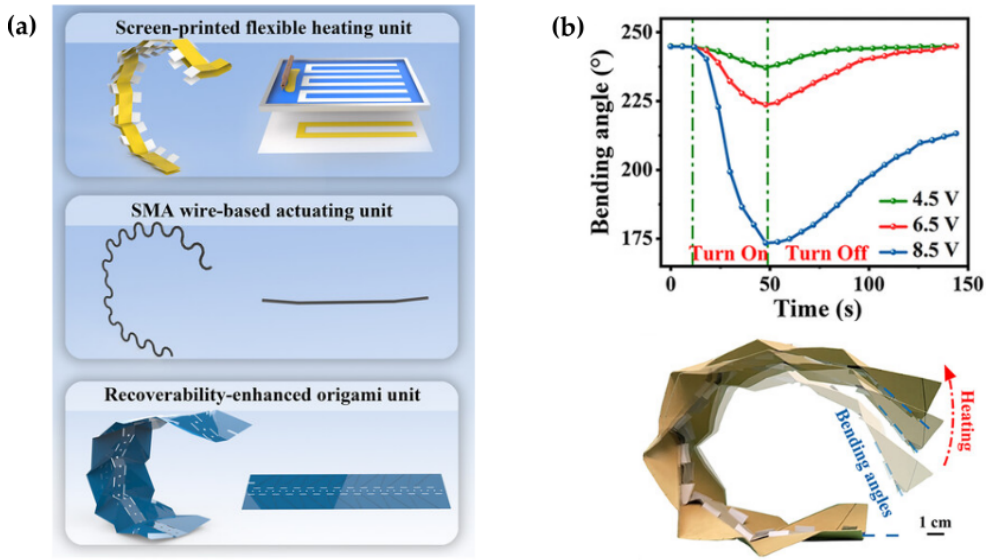

Figure 2.19.: Origami soft actuator (OSA): **(a)** Components of the modularized OSA. **(b)** Changes of OSA bending angle for different voltages (4.5, 6.5 and 8.5 V) Reprinted from [68] CC BY 4.0

To evaluate the performance of different folding concepts, the achieved bending torque and folding angle should be compared. The following Table 2.1 summarizes the presented works with respect to their dimensions and output performances according to [69]:

Publication	D [mm]	L [mm]	Angle [°]	T [mNm]	P [W]
Hawkes et al. [2], [70]	0.1	12	180	4.7	0.25
Firouzeh and Paik [40]	0.1	4.5	60	0.83	1.8
Kim et al. [67]	0.25	320	100	15	1.2
Zheng et al. [68]	0.5	297	21	-	-

Table 2.1.: Comparison of the performance of various folding actuators (SMA diameter D, SMA length L, total (bi-)directional folding angle, folding torque T and heating power P).

The highest reported output torque is achieved by Kim et al. with the aforementioned bi-directional rotational actuator [67]. It reaches a maximum output torque of 15 mNm and a total angular folding motion of 100°. For smaller actuator dimensions, Hawkes and Paik achieve remarkable folding angles. However, the origami-inspired folding actuators, presented by Hawkes, can only fold unidirectionally in 180°.

These examples provide an overview on the challenges regarding the design and fabrication of SMA-based folding actuators. In order to achieve large scale re-programmable matter based on origami layouts, downscaling of actuator dimensions is an important factor. For this purpose, new structuring and assembly concepts must be explored. Additionally, evaluating the actuator performance at smaller size scales requires new experimental setups.

2.5. Operation Principle of the SMA-based Folding Actuator with Magnetic Latching

The aim of the thesis is the development of a novel SMA-based micro folding actuator. Its operation principle is summarized in Figure 2.20. It is composed of SMA folding hinges that interconnect two rigid tiles and that are shape set to discrete angles up to 180° during a heat treatment. The SMA hinges utilize the one-way shape memory effect, as this allows reaching high bending moments. Manual unfolding and subsequent selective heating for shape recovery results in uni-directional actuation. The angular position can be controlled by Joule heating and convective cooling. For bi-directional actuation two unidirectional folding actuators are combined in an antagonistic configuration. By selective

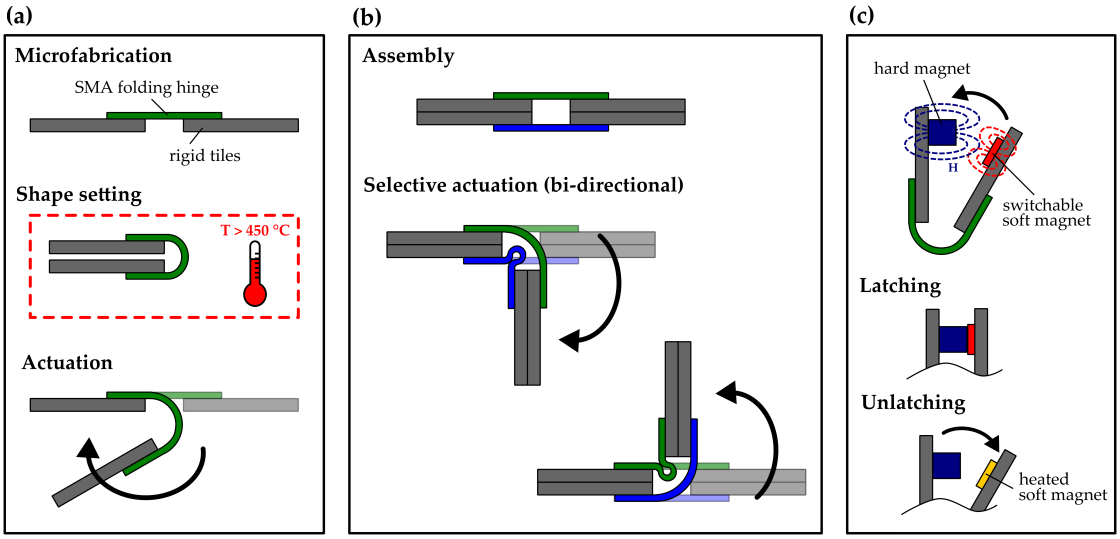

Figure 2.20.: Overview of the concept of the SMA-based micro folding actuator with magnetic latching: **(a)** Uni-directional actuation; **(b)** Bi-directional actuation; **(c)** Magnetic Latching.

heating, the bending motion can be controlled in two directions. For latching, the magnetostatic interaction between hard magnetic dots and switchable soft magnetic films is used. The attractive magnetic forces can contribute to larger folding angles. Buth they mainly prevent the elastic resetting and fix the angular position of the folding actuator, when the heating power is turned off. By locally heating the soft magnetic film, it undergoes the transition to paramagnetic state. The magnetic attraction force drops below the elastic resetting force of the cooled actuator and the freestanding tile is released. From here, a new folding sequence can be initiated.

3. Devices and Methods

The following chapter gives an overview on special fabrication methods related to this work and relevant characterization devices and measurement setups.

3.1. Fabrication Technologies

The main materials used in this work are shape memory alloy thin films, magnetic films, and polyimide as tile material. In the following, the processing and characterization methods for the film materials are explained.

3.1.1. SMA Film Fabrication

Shape memory materials are nowadays available in various sizes and geometries, ranging from rods, sheets, wires, sheets to thin films. No matter the geometry, any fabrication of SMA parts starts with an ingot of the desired alloy composition. These ingots can be produced by vacuum induction melting. The pure elements in form of pellets and rods are mixed and stirred in a graphite crucible, heated by electromagnetic induction and poured into molds [71]. The mixture should be as homogeneous as possible avoiding the dissolution of carbon and oxygen into the melt. These impurities can have a huge effect on the properties of the SMA material [72]. Generally, binary TiNi alloys are very sensitive to variations in composition. For near-equiatomic compositions, a difference of 0.1 at.% in Ni-content with increasing Ni/Ti ratio changes the phase transformation temperatures by 9.6 K [73].
For the use in microactuators, flat homogeneous SMA parts are of most interest. In this work, foils and films are mostly used. These terms are differentiated by their thickness. Thin films generally can be defined as any homogeneous layer of atoms, thus, starting from a few nanometers to several micrometers in thickness [74]. The transition to coatings is fluid. Therefore, here, the term film is defined as a free-standing layer with a thickness below 10 µm. Foils have higher thicknesses and with large lateral dimensions, these extend to below the millimeter range. Here, materials with thicknesses between 10

µm and 100 µm are referred to as foils.
For the fabrication of commercially available SMA foils and films, only three different manufacturing routes are used: Cold Rolling, Sputter Deposition, and Melt Spinning. The two methods applied to the materials used in the work are presented below.

3.1.1.1. Cold Rolling

Cold rolling is a widely used fabrication method for sheets and foils based on step-wise plastic deformation of the material. For TiNi-based materials in particular, the workability in hot rolling is much better [75]. But to avoid surface oxidation and work the material below the crystallization temperature, cold-rolling is often used. The cold-rolling process involves rolling a stoichiometric ingot multiple times until the desired thickness is achieved. Starting from a stochiometric ingot, several successive rolling steps are carried out until the desired thickness is achieved. To reduce any defects in the microstructure, intermediate heat treatment steps are carried out. Since the process is directional, the cold-rolled materials can have a structured microstructure and anisotropic properties [76], [77].

3.1.1.2. Sputtering

The second common manufacturing technology of thin films is sputtering. The sputtering is a physical vapour deposition technology (PVD). The shape memory material is ablated from a solid bulk material (target) and transferred to the substrate. This process takes place in a magnetic field-enhanced gas discharge vacuum that generates a plasma (mix of electrons and positive gas ions). Argon is generally used as a process gas. As shown schematically in Figure 3.1 the target is mounted onto a magnetron and the substrate is fixed on the anode. The positively charged Argon ions are accelerated by the electric field onto the surface of the target, which is connected as a cathode. Individual atoms are knocked out of the target surface and condense on a substrate to build up a film. The exposure time to the vapor flow determines the resulting thickness of the layer. As a bottom-up process sputtering allows for very thin coatings at atomic scale. At higher thicknesses, delamination can be observed due to thermal stresses between the deposited layer and the substrate.
In this work, TiNiCu films were fabricated by sputter deposition at Kiel University. The basic process is described in [78]. Before deposition a Cu film is deposited as a sacrifical layer onto a Si wafer. A *Von Ardenne CS730S* sputter device is used to deposit a Ti-rich TiNiCu film. By wet-etching the sacrifical Cu layer the thin film can be released from

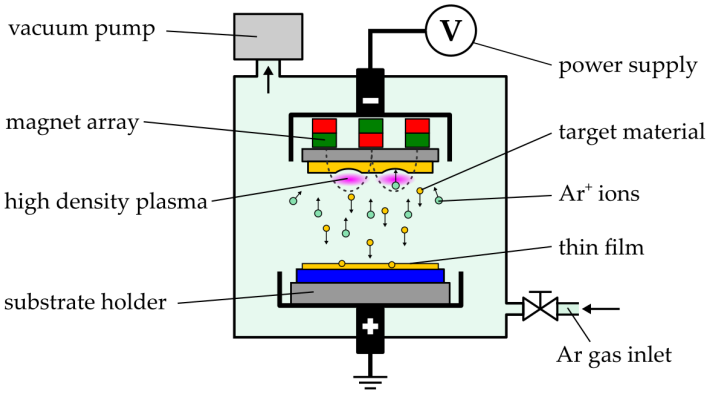

Figure 3.1.: Schematic of magnetron sputtering setup.

the substrate. The amorphous TiNiCu film can then be crystallized by rapid thermal annealing in a high vacuum chamber to prevent oxidation.

3.1.2. Structuring Technologies

Thin-film SMA films need to be structured for both material characterization and for use as actuator components. Unlike additive processes, where active layers can be deposited, the material used in this case is only available in film and foil form. Thus, only subtractive processes are used for material structuring. It is important to ensure that the material is exposed to minimal thermal, mechanical and chemical stress during the process.
The fastest option for structuring any foil material is by using a manual guillotine cutter. As shown in Figure 3.2 (a), the film is aligned with a stop and cut using a sharp cutting blade that is guided by a hand lever. For film thicknesses of less than 50 µm, the force required is very low. Nevertheless, plastic deformation can occur at the cut point. Additionally, only straight cuts can be made, meaning that more complex shapes cannot be achieved.

3.1.2.1. Laser Machining

Laser machining is a fast and efficient way of structuring materials. It involves using a high-power laser beam that is precisely focused and guided along the targeted geometry using optics and CNC (computer numerical control). For cutting, the laser beam heats the material to a point where it melts or vaporizes directly, leaving a trench. Figure 3.2 (b) shows an illustration of this process known as ablation. The material in the irradiated zone is removed by direct evaporation or ejection of particles. Furthermore, a melting zone appears that can generate debris on the surface upon cooling. Due to the high tem-

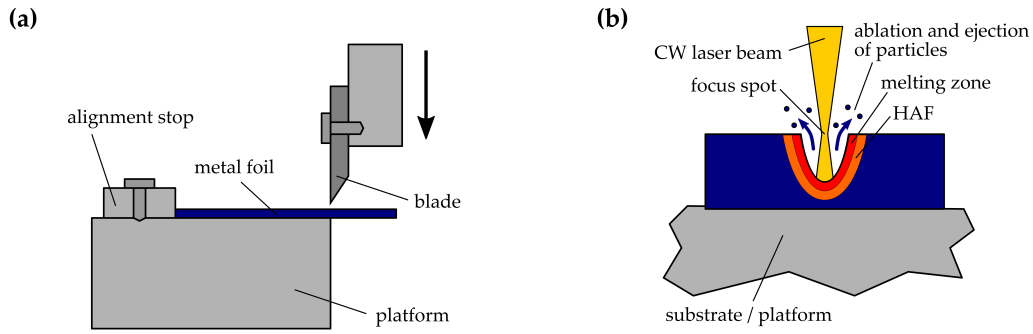

Figure 3.2.: (a) Schematic of a manual guillotine cutter. **(b)** Ablation process during laser cutting.

peratures, the heat affected zone (HAF) spreads into the material and may create thermal stresses. Optimization of laser cutting parameters such as power, speed, and repetition depends on the material's absorption properties and the wavelength of the laser. This non-contact cutting process does not require any pre- or post-treatment of the material (e.g. removal of melt drops) and can be used to cut any geometry.
An ACSYS Piranha II Nd:YAG laser system is used to structure SMA films. It operates at Infrared (IR) wavelength (1.06 µm) in continuous wave mode. The laser system can generate a power of 16 W at a pulse repetition frequency up to 50 kHz. The resulting kerf widths range from 25 to 40 µm, and sharp edges are smoothed during the cutting process. There is a problem associated with localized heating that occurs at the cutting edges during the cutting process. This heat can lead to several issues such as melting, material build-up, and thermal stress that can extend further into the material. In the SMA material, recrystallization can occur within a few micrometers at the cutting edge, which can result in local changes to the material properties. Furthermore, oxidation is visible at the edges, which can affect the material behavior.
Polymer materials such as polymethylmethacrylate (PMMA) and polyimide (PI) are cut with a Universal Laser System VLS 3.50. It is equipped with a CO2 laser source with a wavelength of 10.6 µm and a power output of 40 W. For thicker sheets, the divergence of the laser beam creates a conical cutting edge, but this laser system offers a quick way to structure components for test setups.

3.1.2.2. Optical Lithography

Optical lithography is a process that is highly effective in patterning microstructures. It meets the high requirements for the accuracy and integrity of the material to be struc-

tured. In lithographic processes, polymer-based surface layers are irradiated with photons (optical or UV lithography), electromagnetic radiation (X-ray lithography), electrons (e-beam lithography), or ions (ion beam lithography). The exposed areas undergo a chemical change. A distinction is made between positive and negative resists. When exposed to radiation, negative resists become non-soluble due to polymerization, whereas positive resists are decomposed making them soluble in a developer solution. The resulting patterns can be transferred to the substrate by etching processes or deposition techniques.
In this work, only optical lithography was used for the patterning of microstructures. Figure 3.3 shows an overview of the sequence of process steps. All steps are carried out in the yellow light area of the cleanroom to avoid any undesired exposure to ambient light. First, the wafer or substrate is cleaned of grease and particles. In the case of minor contamination, this can be done in an ultrasonic bath in isopropanol and acetone. To enhance the adherence of the hydrophobic photoresist, the surface is dehydrated. This is achieved by heating the substrate to a temperature of over 100 °C. Afterward, a primer, such as the adhesion promoter HMDS (hexamethyl disilazane), can be applied.

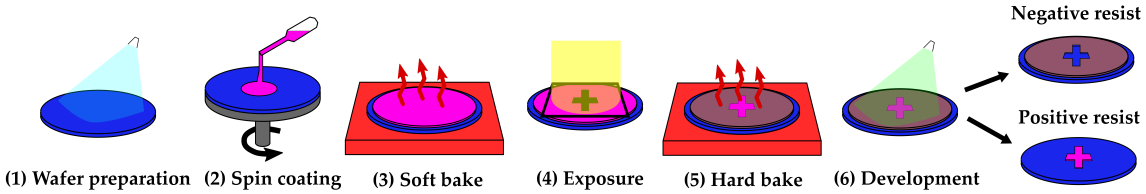

Figure 3.3.: Schematic of a typical lithography process.

In the next step, a photosensitive coating is applied to the substrate by *spin coating*. The substrate is attached to a rotating vacuum-chuck, and a liquid photoresist is dispensed onto it via the use of a pipette. Here, the positive resist AZ1505 (MicroChemicals) is used. The resist is uniformly distributed throughout the substrate surface through centrifugal force, while the chuck rotates at a speed of 1000 rpm for a duration of 60 s, resulting in a homogeneous and even layer thickness of 1 µm. For thicker layers or small substrates, edge beads can form at the borders, which could stick to a photomask, for example. The edges are treated with a solvent to avoid these problems later on during exposure. Subsequently, the solvents present in the photoresist need to be evaporated via a so-called *soft bake*, which involves placing the substrate on a hot plate at 95 °C for 3 minutes. This can also reduce film stresses that are caused by shearing during spin coating.
During the subsequent *exposure* step, a pattern is "printed" in the photoresist, either by using a photomask or directly writing on the resist by using a UV laser. If the substrate

has been previously structured, the layout should contain alignment markers that enable alignment with respect to existing structures. In *mask-based lithography*, a transparent mask plate with an opaque pattern on one side is positioned on top of the substrate [79, p. 321]. The mask is brought into direct contact with the photoresist by applying additional pressure, to avoid any proximity effects. The exposure is by parallel UV light and shadow projection through the mask.

Alternatively, *2D direct laser writing* can generate microstructures in photoresists directly from an electronic layout file. In this work, the rapid prototyping of new microstructure layouts is done using the direct laser writing system DWL66fs (Heidelberg Instruments). A schematic of the system's operating principle is shown in Figure 3.4. A Nd:YAG laser produces a laser light with a wavelength of 355 nm. The laser beam intensity is modulated by an acousto-optic modulator (AOM), while an acousto-optic deflector (AOD) changes the beam angle perpendicular to the moving substrate. A mirror directs the laser beam towards the substrate surface where it is focused onto the resist layer by a lens. A pneumatic auto-focus system ensures that the exposure distance is constant. Due to the substrate motion, stripes with the width of the scan are exposed on the substrate. A lateral resolution of 2.5 µm at a writing speed of 36 mm²/min can be achieved [80].

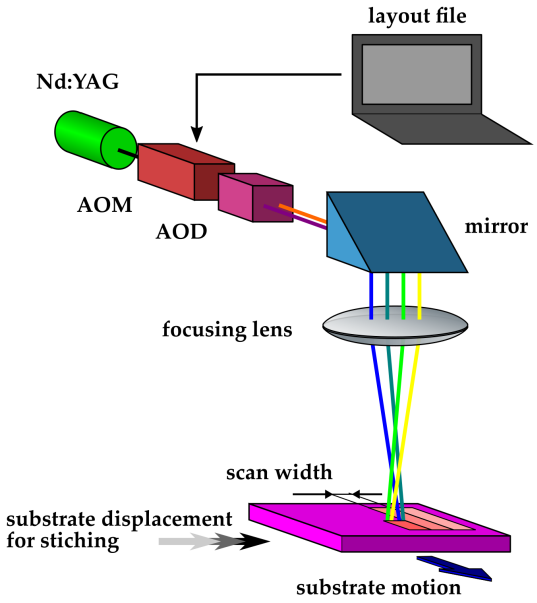

Figure 3.4.: Schematic of a 2D direct laser writing system. Adapted from [81].

The exposure of a resist layer can create thermomechanical stresses which can be relaxed by using a post-exposure bake (PEB). Next, a developing agent is used to remove either the

exposed areas of a positive photoresist or the unexposed areas of a negative photoresist, respectively. The wafer can be processed either by a developer spray or immersed in a developer bath. For the aforementioned AZ1505 photoresist, a potassium-based buffered developer (AZ400K) is diluted by a ratio of 1:4 with deionized (DI) water. Optionally, a hard bake step can be taken to remove any residual solvents. The resulting so-called photomask can then be used for pattern transfer either by deposition of additional layers or by wet-etching. As soon as the resist layer is no longer required, it can be removed e.g. with the undiluted developer solution (stripping).

3.1.2.3. Wet Etching

Wet etching is a common method for removing materials off substrates utilizing liquid etchants or chemicals. A photomask provides the protection layer for the areas that should not be patterned. For longer etching times or chemical reactions where a lot of bubbles are generated, a vapor-deposited hard mask with chromium and gold can serve as a more robust mask for patterning. A 10 nm thin layer of chromium is deposited onto the substrate to promote the adhesion of the 30 nm gold layer. In the case of SMA structuring this Cr/Au hard mask is directly evaporated onto the SMA layer. A photoresist is spin-coated on top and structured by optical lithography. Subsequently, it serves as a patterning mask when wet-etching Au and Cr. After stripping off the photoresist, the Cr/Au hard mask for further wet etching of the SMA material in a HF:HNO3 solution remains. When the wafer is immersed in the etching solution a redox (reduction-oxidation) reaction takes place. In the case of TiNi, HF oxidizes the material and HNO3 dissolves the oxidized material. Care has to be taken that the ratio of reactant to removed material is high enough to avoid depletion of the etchant. Furthermore, underetching of the hard mask has to be avoided by removing the substrate as soon as the SMA is fully etched.

3.1.3. Thermal Annealing of SMAs

The heat treatment of SMAs has a direct influence on the deformation behavior and material properties. In particular, the phase transformation temperatures depend on this important process step. In addition, both superelasticity and the one-way shape memory effect can be adjusted via heat treatment. Heat-treated films that are brought into a new memory shape by a second annealing step do not have the same deformation quality. Each heat treatment step can contribute to precipitation (e.g. Ti_3Ni_4) and surface oxidation.
The heat treatment for the initial imprinting of the shape memory effect depends on the

factors of duration and temperature. The higher the temperature, the shorter the imprinting step can be carried out. It can also be roughly stated that the phase transformation temperatures and shape recovery strain increase with increasing aging temperature [82, p. 118-120]. However, effects such as oxidation are also intensified at higher temperatures.
The foils and sputtered films, which have already been heat-treated after fabrication, must be brought into a new memory shape for use as folding actuators. If the heat treatment is carried out under vacuum conditions, the surface oxidation can be minimized. To achieve this, the samples are fixed onto a temperature sensor and inserted into a quartz tube. The tube is flushed with nitrogen for removing any loose particles and evacuated by a vacuum pump. If the vacuum level drops below $10^{\div}2$ mbar, the tube is placed into the oven. The temperature and vacuum conditions are monitored. When the required annealing time is reached, the tube is again flushed with nitrogen to quench the SMA material.

3.1.4. Electrical Contacting for Annealing and Actuation

Another method of heat treating SMA is direct Joule heating. Joule heating, also known as resistive or Ohmic heating, is a phenomenon where the energy of an electric current generates heat as it flows through a conductor. The Joule's law states that the heating power P produced by an electrical conductor is proportional to its resistance R and the square of the current I flowing through it:

$$P = I^2 R \tag{3.1}$$

In SMAs, the heat generated can be utilized not only for local heat treatment, but also to actuate one-way shape memory actuators without requiring an external heat source to heat the entire actuator. For this purpose, the actuators need to be designed in a way that allows them to be electrically contacted, and the area to be heated must have the highest local resistance. However, TiNi is not well-suited for soldering due to the presence of a natural oxide layer.
The gap welding shown in Figure 3.5 is a resistance welding technique in which two electrically conductive parts (e.g. SMA and conductor track) can be joined together. The two bonding partners are stacked and pressed by two parallel electrodes. A voltage is applied across the two electrodes that generates a current flow across both welding parts. The interface is heated due to resistive heating and melts. During solidification, a weld-like material bond is created. Here, a UNITEK Equipment Linear DC resistance welding device is used that allows to monitor and control the current flow and/or applied voltage.

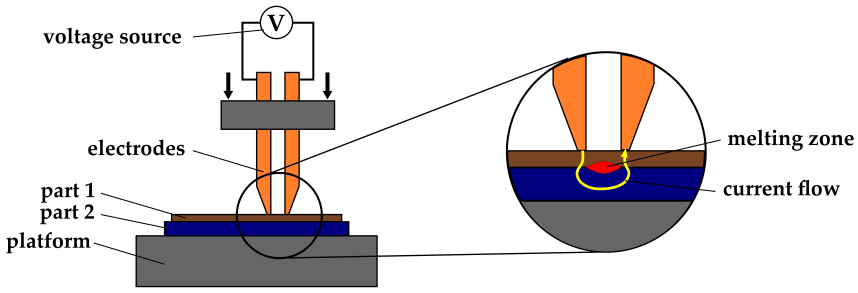

Figure 3.5.: Schematic of a gap welding setup.

An alternative for smaller contact areas is electrical bonding with conductive glue. A two-component silver glue is applied onto the SMA parts and copper wires can be attached on those regions. The positioning of both components must be secured during the curing on a hot plate (at 100 °C). As its mechanical connection is rather weak, an additional layer of an electrically insulating epoxy is applied which avoids detatching of the bonding partners.

3.2. Characterization Methods

3.2.1. Thermal Characterization

The thermal properties of SMAs include the phase transformation temperatures, heat capacity, thermal expansion coefficient, and thermal conductivity. The most common method to determine the phase transformation temperatures in a stress-free state is the differential scanning calorimetry (DSC), as mentioned in section 2.2.1. The sample material is encapsulated in a sample pan of high thermal conductivity (e.g. aluminum) and is placed together with a reference pan in the inert gas chamber. Both pans are heated at a controlled rate. Heat flux sensors measure the heat flow in and out of the sample compared to the reference material. Changes in the heat flow indicate phase transitions, melting, or crystallization. For SMAs the phase transformation from austenite to martensite is exothermic and results in a peak in the DSC curve. The area below the peak is equivalent to the latent heat of the phase transition.
In this work, a *Netzsch Phoenix DSC 204* is used for DSC measurements which is equipped with a nitrogen gas connection for purging and as inert gas. Additionally, liquid nitrogen is used for cooling. The temperature sweep rate is set to 10 K/min and a holding time of 2 min is set in between the heating and cooling cycles. The specimen mass is measured with a precision scale and ranges typically between 7 and 15 mg. The peaks of the

exothermic and endothermic phase transformations are bell-shaped. The start and finish temperatures are evaluated by drawing tangents at the steepest parts of the two sides of the peak. The intersection of the tangents with the baseline defining the latent heat area, gives the temperature values (compare [83]). The heat capacity, defined as the amount of heat required to raise the temperature of the sample by 1 K, is derived according to ASTM E1269 [84].
Further thermal characterizations, such as surface temperature profiles of actual actuators or the elastocaloric effect upon rapid loading/unloading are obtained by IR thermography. The IR camera measures the heat radiated by a specimen. When the emission coefficient of the surface is known, the temperature can be derived. Here, the IR camera *FLIR A655sc* is used with a macrolens that provides a pixel size of 15 µm. The frame rate can be set up to 200 fps. The absolute temperature can be measured with an accuracy of 2 K. Control, data acquisition and post processing are performed with the provided software *FLIR research IR*. In experiment, the specimens under investigation are covered with a thin layer of black carbon spray. Its emissivity has been calibrated to 0.8.

3.2.2. Electrical Characterization

The electrical properties of materials, such as electrical conductivity, are strongly dependent on the structure of the material at the atomic scale. Therefore, phase transformations or crystallization processes can be revealed by changes in resistivity ρ. The most common method to measure the resistance of a material is to use two surface probes and apply a current across them. Simultaneously the voltage drop is measured between the two contact points. The resistance R_{tot} can be calculated as $R_{tot} = V/I$. The accuracy of this value is affected by parasitic resistances, such as contact resistance between the material and the probes or the resistance of the cables.
Parasitic resistances can be eliminated by a 4-point probe measurement. A sample current I is applied across the two outer samples and the voltage drop V across the two inner samples is measured. The differential resistance is $dR = \rho\frac{dx}{A}$, where A represents the area of the spherical protusion of the emanating current in the bulk material. If the spacings s between the four probes are identical, the resistance R is calculated by integrating between the inner probe tips [83]:

$$R = \int_{x_1}^{x_2} \rho \frac{dx}{2\pi x^2} = \frac{1}{2s}\frac{\rho}{2\pi} \tag{3.2}$$

Due to the superposition of current at the two outer probes, $R = V/2I$. Thus, the bulk resistivity can be expressed as:

$$\rho = 2\pi s \left(\frac{V}{I}\right) \tag{3.3}$$

For a very thin layer (thickness $t << s$), the current spreads in rings instead of spheres. The area A expresses as $A = 2\pi xt$. The resistance R can be calculated by:

$$R = \int_{x_1}^{x_2} \rho \frac{dx}{2\pi xt} = \frac{\rho}{2\pi t} ln(2) \tag{3.4}$$

The specific resistivity for a thin sheet then derives to:

$$\rho = \frac{\pi t}{ln2} \left(\frac{V}{I}\right) \tag{3.5}$$

Depending on the dimensions of the sheet and relative to the probe spacings s, additional correction factors have to be considered [85]. Here, the thickness of the foils does not exceed 20 µm. If the probe spacings are larger than 50 µm, and the lateral dimensions exceed 8 mm, the correction factors can be neglected.

In this work, temperature dependent electrical resistance measurements are performed in an in-house upgraded cryostat from CryoVac. As shown in Figure 3.6, it consists of a vacuum chamber, where a thin film can be fixed onto a heating/cooling tube. The adapter with four spring-loaded pins with equal spacing of 0.2 mm is positioned by centering pins onto the thin film. The four pins are connected to a current source and two digital multimeters, for accurate current and voltage monitoring, according to the 4-probe resistivity setup. The chamber is continuously evacuated by a vacuum pump to stay below $2x10^{-}2$ mbar. The temperature measured by a temperature sensor located underneath the substrate. A thermostat is controlled by a PID control implemented in LabView to regulate the electrical heating power and a magnetic valve for liquid nitrogen cooling. In contrast to the DSC measurement, the temperature is not swept at a constant rate, but the temperature value is stabilized in a range of ±0.5 °C for 30 s. The resistance value is then read out after 30 samples if the relative resistance change is below $R_{n-1}/R_n x R_n/\Delta t < 10^{-5}\Omega/s$ and the approach to the next temperature value starts. The resistance values versus temperature and the duration until temperature stabilization are plotted in LabView graphs. The raw data is evaluated in customized Origin import files.

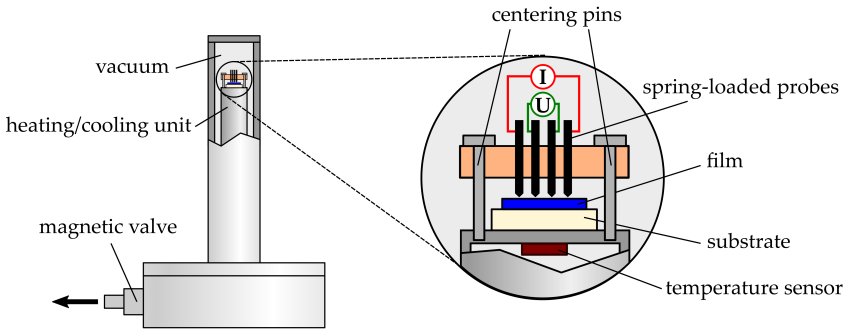

Figure 3.6.: Schematic of resistance measurements

The temperature-dependent electrical resistance curves of SMAs show a drop during the phase shift from martensite to austenite and an increase for the reverse transformation. The phase transformation temperatures can be estimated by fitting tangents to the linear sections of the curves and reading off the temperatures at the intersections.
The Wiedemann-Franz law can be used to derive the thermal conductivity of metals by stating that the ratio of the electronic contribution of the thermal conductivity k_{th} to the electrical conductivity κ_e is directly proportional to the temperature T. It is based on the fact, that heat and electrical movement involve freely moving electrons in the metal. The law can also be used to determine the thermal conductivity of SMAs [86] and can be expressed by the following equation:

$$k_{th} = \kappa_e L T, \tag{3.6}$$

where $L = 2.44 \times 10^{-8} W.\Omega.K^{-2}$ is the proportionality constant, known as the Lorenz number.

3.2.3. Mechanical Characterization

The mechanical properties of SMAs are generally derived by uniaxial tensile tests. A specimen sample is clamped in between a fixed and a movable holder. The traverse of the tensile testing machine elongates the sample by moving upwards. The relative elongation Δl is tracked by a position sensor and the force F is measured by a load cell. For a known initial cross-section A_0, and the initial length L_0, the instantaneous engineering stress is $\sigma = F/A_0$ and the engineering strain is $\varepsilon = \Delta l/L_0$. As in classical stress-strain curves, Young's modulus of the different phases can be derived from the slope of the linear regions, as mentioned in section 2.2.2. Further mechanical characteristics of interest, are

the critical transformation stress, maximum transformation strain and yield strength.
In this work, tensile tests are performed with the *Zwick Roell* tensile testing machine, equipped with 5 N and 50 N load cells providing a resolution of 0.002 N and 0.25 N, respectively. All experiments are conducted by displacement control with a resolution of 0.25 µm. For samples with thicknesses below 10 µm a special holder is designed in which dog-bone shape samples can be positioned, clamped and additionally glued to avoid slipping during loading.
In order to determine the properties of austenitic SMAs and the Clausius Clapeyron coefficient, the sample holder is placed into an in-house built heating chamber. The temperature inside the chamber is adjusted by a PID controller and additionally monitored by attaching thermocouples onto the sample holder. This setup allows for tensile testing at different ambient temperatures up to 80 °C. In general, the strain rate during loading and unloading should avoid elastocaloric effects to ensure isothermal conditions. This is particularly important when the ambient temperature is between the austenite start and finish temperature and any additional heat could contribute to a structural change. Therefore, a strain rate of at least $10^{-4}/s$ is applied during tensile tests in the temperature chamber. For high temperatures, the chamber is heated for up to 1 h in order to achieve a stationary and homogeneous temperature distribution.
The Young's modulus of the initial specimen is determined via the linear fit to the straight section of the load curve. The critical transformation stress σ_{cr} can be obtained by the intersections of stress plateau and elastic curve sections. If the material is fully transformed and displays a linear increase after the transformation plateau, the Young's modulus of the reoriented martensite can be determined by fitting a line to the aforementioned linear portion. The maximum transformation strain ε_t is represented by the remaining strain after unloading, which is the point where the stress-strain curve intersects the x-axis. The residual strain ε_r corresponds to the non-recoverable strain that remains even after heating above A_f.

To accurately measure the output torque of folding actuators, it is essential to have an experimental setup that allows the rotational motion of the freestanding element without introducing any additional moments (such as through friction). This becomes even more challenging at a micro-scale due to the reduced dimensions and small output torques. One possible solution is to measure the force and consider the lever arm to the rotational axis to calculate the corresponding torque. Force measurements are mainly conducted by using the 5 N load cell of the tensile testing machine which provides a displacement-controlled motion and highly resolved displacement steps. Another option is the usage

of micromanipulators equipped with a micro force measurement tip (Kleindiek). In both cases, the fabricated folding actuators are loaded, and the resulting angular motion is tracked by a camera. In a postprocessing step, one can extract the rotational axis, the resulting folding angles and the lever arms from recorded images and videos.

4. Double-bridge SMA-based Folding Actuators

With the objective of achieving bi-directional folding through the utilization of the one-way shape memory effect of SMAs, a double bridge actuator is designed and structured starting from a TiNi foil.
This chapter discusses the material characterization of the TiNi foils and the design and fabrication process of the folding actuators based on the material properties. The folding actuator's uni- and bi-directional folding behavior is examined, and further steps toward miniaturization are explored[1].

4.1. Material Characterization of TiNi Foils

The TiNi material used in this work is commercially available and has a nominal chemical composition of $Ni_{55.57}Ti_{44.39}$. The datasheet reports a carbon content of 4 at%. The foils of 20 µm thickness are fabricated by cold rolling and subsequently heat-treated. The manufacturer does not provide any precise information on heat treatment, so various heat treatment temperatures and durations are tested. Heat treatment in the vacuum furnace at 460 °C for 45 min results in very similar transformation temperatures, so that these are used as the optimum parameters for the shape setting in the further course.
An additional DSC measurement is performed on the one-way shape memory foil material after having received an additional in-house heat-treatment in a vacuum furnace. The temperature is cycled between -100 °C and 150 °C. Figure 4.1 shows the resulting exo- and endothermic heating and cooling curves. On cooling, a two-step A→R→M transformation is observed. On heating, a one-step transformation M→A takes place. The derived transformation temperatures are summarized in Table 4.1 and compared to the manufacturer's characterization data. At room temperature and in absence of any external loads, the material is in R-phase condition.

[1] The content of chapter 4.4 is based on the master thesis of V. Gottwald [87], which was co-supervised by the author. The results of V. Gottwald's master thesis are used with his permission.

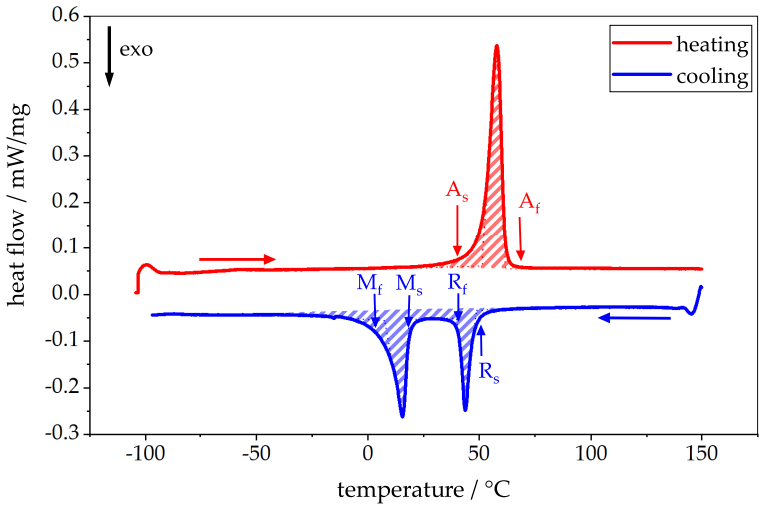

Figure 4.1.: DSC measurement of TiNi foil material. The phase transformation temperatures are labeled by arrows and summarized in Table 4.1

Figure 4.2 (a) shows the heating and cooling cycle of the four-point probe resistance measurement in the cryostat between -150 °C and +140 °C covering the complete phase transformation. On cooling, the intermediate R-phase transition is characterized by an increase in resistance followed by a decrease during the R - M transition. The derived transformation temperatures are summarized in Table 4.1.

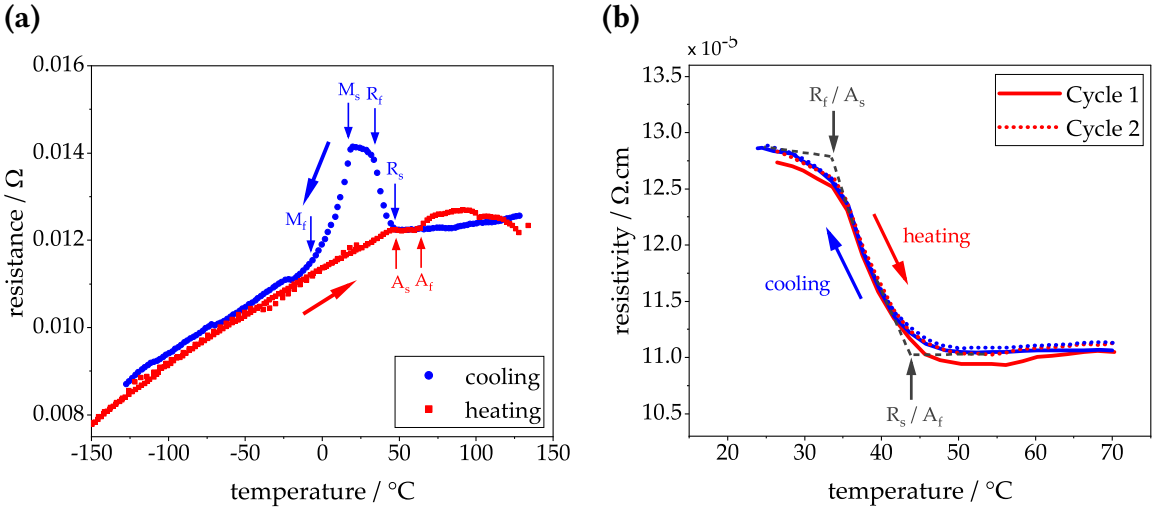

Figure 4.2.: Resistivity measurement of annealed TiNi (460 °C, 45 min). **(a)** Thermal cycling between -150 °C and +140 °C. **(b)** Thermal cycling between ambient temperature (23 °C) and above A_f without martensite phase transformation. The black dashed lines indicate the tangent lines for the derivation of the transformation temperatures.

The foldable microactuators are not actively cooled during operation. The temperature is therefore only varied between room temperature and austenite finish temperature. The associated back and forth transformation from the R-phase to austenite without the formation of twinned martensite shows a low thermal hysteresis and good fatigue behavior (Figure 4.2 (b)). After the first cycle, the transformation is already highly reversible, and the phase transition takes place between 33.7 °C (R_f/A_s) and 43.9 °C (R_s/A_f) on cooling and heating. These measurements are used to derive the electrical resistivity and thermal conductivity according to equations 3.3 and 3.6 for the simulation of resistive heating.

The comparison of the transformation temperatures in Table 4.1 shows only small variations and confirms the applied annealing parameters for the supplied material (460 °C, 45 min). By varying the heat treatment temperature between 400 °C and 500 °C and the duration between 30 mins and 5 h, it was not possible to shift the transformation temperatures of martensite above room temperature. This would require a modification in the alloy composition.

Heat treatment	**Method**	$\mathbf{M_s}$	M_f	R_s	R_f	A_s	A_f
manufacturer	DSC	14.6 °C	-9.3 °C	49.2 °C	39.7 °C	48 °C	64 °C
460 °C, 45 min	DSC	19 °C	9 °C	49 °C	40 °C	52 °C	62 °C
460 °C, 45 min	Cryostat	18.2 °C	-8.3 °C	46.2 °C	33.7 °C	48.5 °C	62 °C

Table 4.1.: Comparison of derived transformation temperatures from various samples and measurement devices.

Due to the cold rolling process, the 20 µm TiNi foil exhibits anisotropic material properties. The orientation can be identified by periodic dark lines in rolling direction on the material surface. When used as a folding actuator, the material is not only subjected to uniaxial loads, so that the deviations in the mechanical properties in the different directions are also investigated to gain a better understanding of the material behavior. In Appendix A.1 specimens oriented in rolling direction (RD) and in transverse direction (perpendicular to RD) are compared for the initial cycle and fourth loading cycle. Regardless of the loading direction, the initial loading curve shows a higher critical stress and a flatter transformation plateau. From the second cycle onwards, the stress-strain curve is reproducible. The stress in TD is higher and the transformation strain is reduced. For this reason, areas that experience the maximum strain in the actuator design should be aligned along the RD.

In a stress-free state, the material transforms from R-phase to austenite phase upon heating. Quasi-stationary tensile tests are conducted in the heating chamber for different ambient temperatures at low strain rate ($10^{-4}/s$). The loading curves at a strain rate of $10^{-3}/s$ result in a less flat stress plateau (represented by dashed lines). The resulting stress-strain curves for four temperatures are shown in Figure 4.3 (a). The plateau shifts to higher stress with increasing temperature. At an ambient temperature of 65 °C the material is not yet in fully austenitic state, and a quasi-plastic strain remains after unloading. This strain can be restored when heated above 80 °C. A test at this ambient temperature cannot be carried out to protect the load cell in the used experimental setup. The critical transformation stress is plotted for different ambient temperatures in Figure 4.3 (b). The Clausius-Clapeyron coefficient C_M is estimated by a linear fit to 7.75 MPa/K.

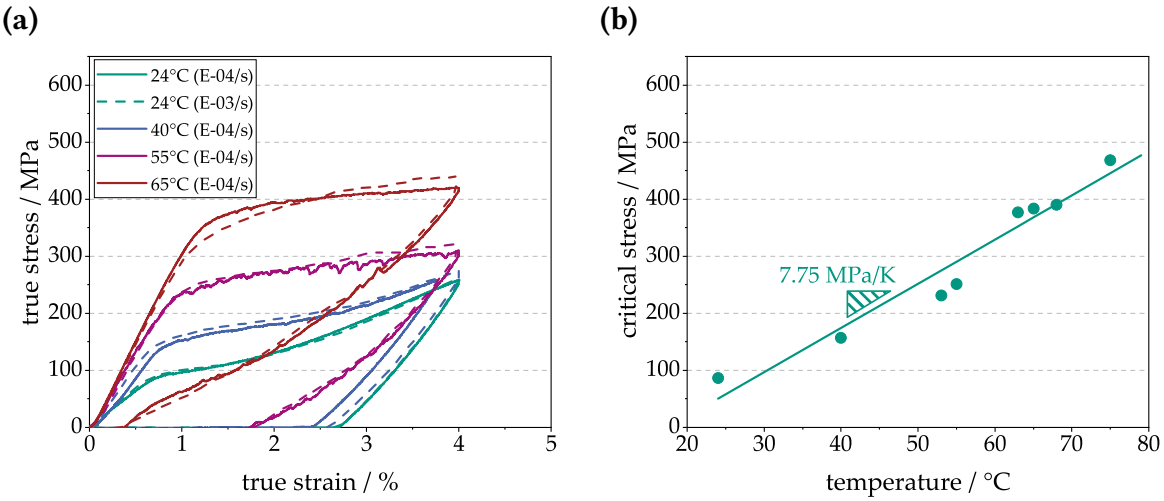

Figure 4.3.: Tensile tests of 20 µm TiNi cold-rolled foil at various temperatures in a temperature chamber: **(a)** Stress-strain characteristics. The strain-rate is indicated. **(b)** Critical stress for phase transformation as function of temperature.

While the small temperature hysteresis of the R-A phase transition can be an advantage for high frequency applications, the stress-induced R-phase can only generate strains up to 0.8 % [88]. At higher strain stress-induced martensite is formed which mainly contributes to the 6 % recoverable strain that is shown by the cold-rolled TiNi foil. The detwinning of the R-phase has not been recorded by the tensile tests and no crystallographic investigations have been undertaken to further understand the phase transitions of the TiNi foil.

Besides the shift of the stress plateau, the stiffness of the material changes upon heating, due to the co-existence of multiple phases. The formation of austenite and stress-induced martensite results in a complex interplay of three phases. According to the rule of mix-

ture, the effective modulus can be derived from the phase fractions of the "soft" low temperature phases (R- and M-phase) and the “hard” austenite. The temperature-dependent effective modulus and the sigmoidal fit can be found in Appendix A.2.
The material parameters for the cold-rolled NiTi foil are summarized in Table 4.2. These parameters are used by project partners to develop a simulation model that can describe the folding behavior of the actuators.

Parameter	**Symbol**	**Value**	**Unit**
Young’s modulus (starting phase)	E_R	12.9	GPa
Young’s modulus (austenite)	E_A	32.5	GPa
Critical stress (at RT)	σ_{cr}	95	MPa
Clausius-Clapeyron coefficient	C	7.75	MPa/K
Transformation strain (at RT)	ε_t	0.035	-
strain limit (at RT)	ε_{max}	0.06	-
Specific heat capacity (at RT)	c_p	360	J/kg/K
Thermal conductivity (starting phase)	k_{th}^R	5.8	W/m/K
Thermal conductivity (austenite)	k_{th}^A	8	W/m/K

Table 4.2.: Summary of experimentally derived parameters for one-way TiNi foil heat-treated at 460 °C for 45 mins.

One disadvantage of the cold-rolling foil is its non-uniform thickness distribution. Variations of up to 2 µm have been measured. Furthermore, as a top-down process, cold-rolling for even thinner foils requires a lot of effort. For the miniaturization of the folding actuators, thinner and more homogeneous films are required. One possibility to obtain thinner foils, besides bottom-up deposition methods, is the controlled wet-chemical etching of 20 µm foils. This process of film thickness reduction is discussed in more detail in chapter 4.4.

4.2. Design and Fabrication of Double-bridge Folding Actuators

The basic engineering element for the dimensioning of the entire folding actuator is the double bridge structure made of TiNi. This structure connects the two individual tiles and is designed to enable folding to + and − 180°, acting as flexible element and folding hinge. The initial state corresponds to the folded configuration (Figure 4.4 (a)). After imprinting this new memory shape by a heat-treatment, this configuration is completely stress- and strain-free. The folding radius r is defined by the inner radius. The folding

hinge can be unfolded to 0° by applying an external bending moment either manually or by an antagonistic actuator. This will result in a deformation along the cross-section of the unfolded segment (Figure 4.4 (b)). The previously located inner area of the segment experiences tensile stress, while the outer area is compressed. The neutral fiber (marked with a dashed line) is the undeformed region. Here, we assume a symmetry in compression and tension loading of SMAs. Therefore, the neutral fiber runs halfway through the thickness, perpendicular to the applied bending moment.

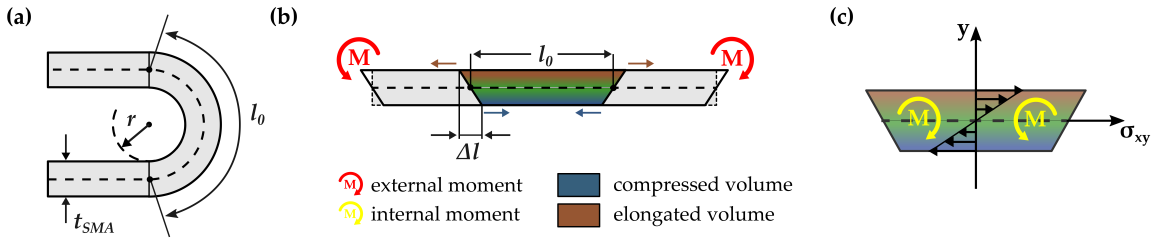

Figure 4.4.: Relevant dimensions for the design of SMA folding bridges. **(a)** memory shape of SMA hinge, **(b)** unfolded configuration

Since the neutral axis remains undeformed it serves as reference to determine the strain induced by unfolding. Its initial length l_0 and the elongation Δl at the outer surfaces derive from the circumferences of the corresponding half circles:

$$l_0 = \pi(r + \frac{t_{SMA}}{2}) \tag{4.1}$$

$$\Delta l = l_0 - \pi r = \pi \frac{t_{SMA}}{2} \tag{4.2}$$

The highest strain is located on the outer surfaces of the unfolded segment. The strain ε is derived by $\varepsilon = \Delta l / l_0$ and results in:

$$\varepsilon = \frac{t_{SMA}}{2r + t_{SMA}} \tag{4.3}$$

The maximum allowable tensile and compressive strain ε_{max} and the foil thickness of the SMA material are relevant for obtaining the minimum admissible folding radius r_{min}:

$$r_{min} > t_{SMA} \frac{1 - |\varepsilon_{max}|}{2|\varepsilon_{max}|} \tag{4.4}$$

The TiNi foil with a given thickness of 20 µm allows for a maximum strain of 6 %. Thus, the minimum folding radius derives to $r = 157$ µm. The minimum separation between the tiles or the minimum bridge length is $l_{br} = \pi(r + t_{SMA}) = 0.56$ mm. From a mechanical point of view the width of the bridges w_{br} can be neglected in the case of an uniaxial bending moment M_z. But in terms of thermal and electrical behavior, w_{br} is a critical design parameter. The electrical resistance of the bridge structures $R_{br1,2}$ can be calculated using the formula

$$R_{br1,2} = res_{SMA} L / A_c, \tag{4.5}$$

where res_{SMA} is the temperature-dependant resistivity of the SMA, and A the constant cross-sectional area $A_c = t_{SMA} \times w_{br}$. The main criterium is temperature homogeneity of the active parts. Therefore, the bridges require the lowest resistance across the entire actuator. If the thickness is fixed, the resistance can be increased by reducing the width of the bridges w_{br} and increasing the length l_{br}. This will also reduce the amount of heating power required to control the folding actuator.

The 20 µm TiNi foils are used to fabricate macroscopic mm-sized SMA folding actuators which are to be heat-treated in the vacuum oven. The TiNi foils are laminated onto a thermal release tape and structured using the Nd:YAG laser. Figure 4.5 (a) shows the layout of the SMA double bridge structures and the respective dimensions of the folding hinges and their separation. Two centering holes are designed to fix the sample in the folded configuration into the annealing setup by a pin. The two welding legs are connected by a thin bridge. This provides more mechanical stability when removing the laser-cut structure (Figure 4.5 (b)) from the substrate and when inserting it into the annealing fixture. The detailed description of the annealing procedure to set the folded configuration as memory shape can be found in the appendix A.3. Figure 4.5 (c) depicts the structure after annealing in the folded configuration.

The further assembly steps are depicted in Figure 4.6 (a). Two Ni stripes are glued onto a polyimide (PI) tile which is structured by a CO2 laser. The electrical connection is realized by gap welding the welding legs of the shape memory double-bridge structures onto the Ni stripes. Finally, the second PI tile is bonded. The completed folding actuator is positioned and fixed onto a movable platform by circular holes in the tiles. Only the tile which is electrically contacted is fixed, while the other one is freely movable. The two Ni stripes can be easily clamped so that the folding actuator can be actuated by

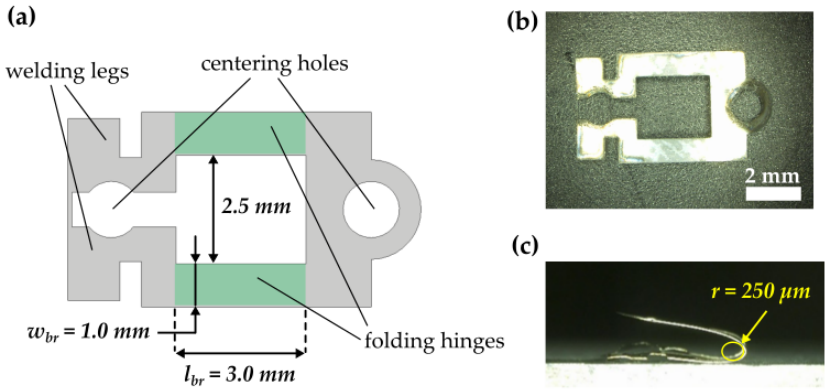

Figure 4.5.: **(a)** Layout of macroscopic folding actuators. **(b)** Laser cut SMA foil **(c)** fabricated structure in folded configuration after annealing.

resistive heating. For a perfectly annealed folding actuator, the initial configuration is the +180° fold.

Bi-directional actuators comprise two single folding actuators, consisting each of a pair of tiles that is interconnected by a folded double-bridge SMA actuator. As depicted in Figure 4.6 (b) the two actuators are deformed to a flat state (0°). The two pairs of tiles are bonded to each other in an antagonistic configuration. Due to the counteracting of a +180° folded single actuator and a -180° folded single actuator, the resulting equilibrium position is at 0°.

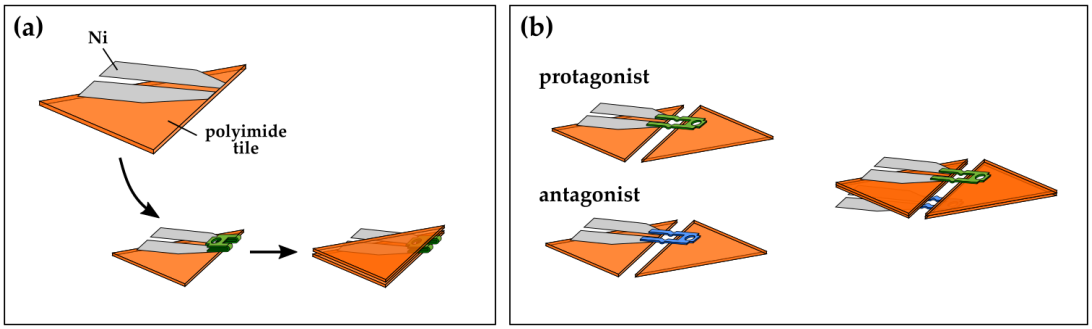

Figure 4.6.: Schematic of the folding actuator assembly: **(a)** uni-directional folding actuator gap-welded onto Ni stripes for electrical connection, **(b)** bi-directional folding actuator consisting of two counteracting uni-directional folding actuators bonded on the tiles.

4.3. Characterization of Folding Performance

The actuation behaviour of the folding actuators is studied in terms of mechanical and thermal performance. This includes the characterization of folding angles, heating power, actuation torque, temperature distribution, influence of loading and the folding dynamics (actuation hysteresis, folding speed, ...). The folding angles and the temperatures are tracked by IR thermography. The heating current is supplied by a current source and the voltage drop across the actuator is monitored by a digital multimeter (DMM). The resulting heating power is derived by the product of supplied current and measured voltage. The force measurements required to determine bending moments are recorded with a 5 N load cell of a tensile machine.
Here, uni-directional folding actuation is achieved by shape recovery of deformed SMA folding actuators. The martensitic transformation from stress-induced martensite to austenite is induced by local Joule heating. The SMA folding actuators are unfolded manually and/or by applying different biasing loads, and thereby generating stress-induced martensite in the folding region. Here, only single folding hinge structures are characterized without coupling to an antagonistic actuator. These folding actuators can only fold into one direction (0° - 180°) but allow for wide investigation of actuation behavior.
The bi-directional folding characterization is based on the maximum folding angles in heated and cooled state. In the following, various experiments are performed on samples with the dimensions shown above: hinge width of 1 mm, hinge separation of 2.5 mm and hinge length or separation between the tiles of 3 mm. The folding radius is set to 250 µm. The side length of the triangular tiles is 20 mm.

4.3.1. Uni-directional Folding Performance

If the folding axis of the uni-directional folding actuator is aligned with the gravitational force, the freestanding tile is distorted by a small angle due to the weight of the tile. Figure 4.7 shows the ideal position of the tiles and the real deviation in dashed lines. In this sample orientation the two folding hinges are not loaded equally. The upper hinge (bridge T) is subjected to an additional tensile load, while a compressive load is applied on the lower hinge (bridge C). In order to investigate the influence on the folding actuation, the folding actuator is manually unfolded to 0° and heated by Joule heating for shape recovery. The folding angle of each hinge is observed individually by video tracking. The position of the camera is switched between T and C. Here, the load of the tile is 0.39 mg. The deviation of the folding characteristic is relatively small. Bridge T which experiences an additional tensile load starts its folding actuation at approximately

0.2 V higher compared to the compressed hinge (bridge C). For both hinges the folding is completed at around 3.1 V. The difference in folding angle is constant at 4° before and after folding.

Due to this small deviation which is caused by the distortion of the tile relative to the folding axis, only one folding hinge is considered in the characterization of folding angles in the further course.

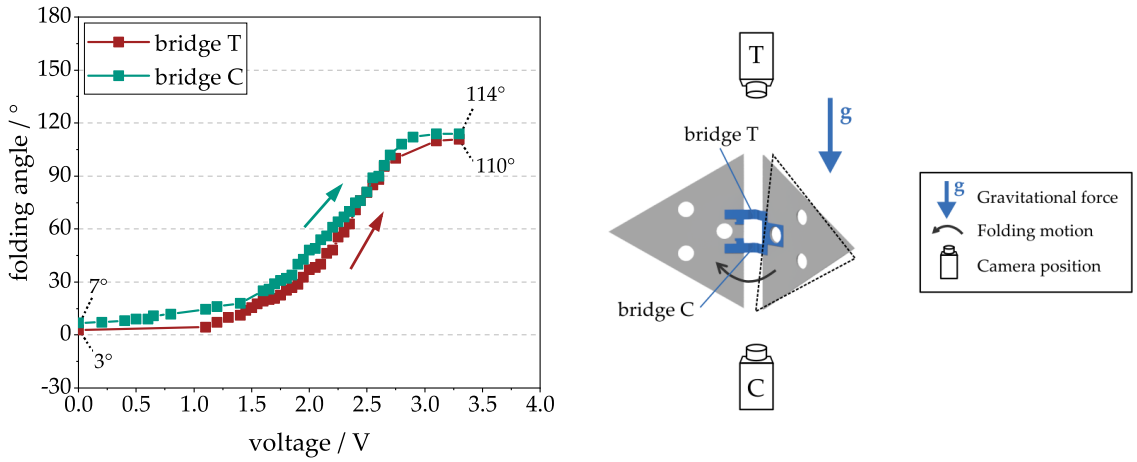

Figure 4.7.: Folding characteristics of the two individual folding beams (loaded in compression (C) and tension (T) due to gravitational load of the tile) after manual unfolding to 0°.

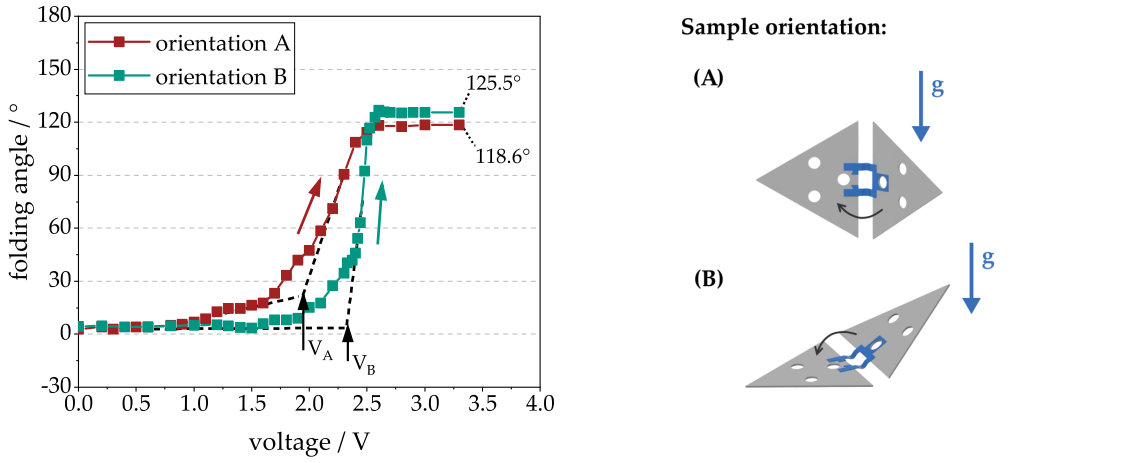

Figure 4.8.: Folding performance depending on sample orientation after unfolding to 0°. In orientation A the folding axis of the sample is aligned along the gravitational field, in orientation B the gravitational load of the freestanding tile acts perpendicular to the folding axis.

If the folding axis of the uni-directional folding actuator is oriented perpendicular to the gravitational force, the external load of the tile acts additionally onto the SMA folding hinge. Figure 4.7 (a) shows the shape memory recovery of the folded actuator upon heating for two different orientations. Here the load of the tile is 49.5 mg. Thus, in orientation B, a gravitational force of around 0.486 mN acts onto the folding hinges. In orientation A, the unfolding is initiated at a voltage of V_A = 1.8 V and reaches a folding angle of 118.6°. In orientation B the starting voltage for folding is shifter to higher voltages (V_B = 2.3 V) and the folding characteristic shows a steeper curve. The resulting folding angle is 125.5°. The voltage shift can be attributed to the stress-induced increase in SMA transformation temperatures and the increase in folding angle of 7° is due to the additional weight of the tile.

The influence on the folding behavior and the opening angles under an additional load is examined representatively by using different tile materials. This allows to study the relevant forces to close remanent opening angles of the folding actuators. Figure 4.9 shows the folding characteristics upon heating. In the unloaded case the actuator folds back to 150° upon heating. Upon cooling the actuator re-opens to an angle of 114°. This behavior can be attributed to an imprinted two-way shape memory effect during heat-treatment and thermo-mechanical training.

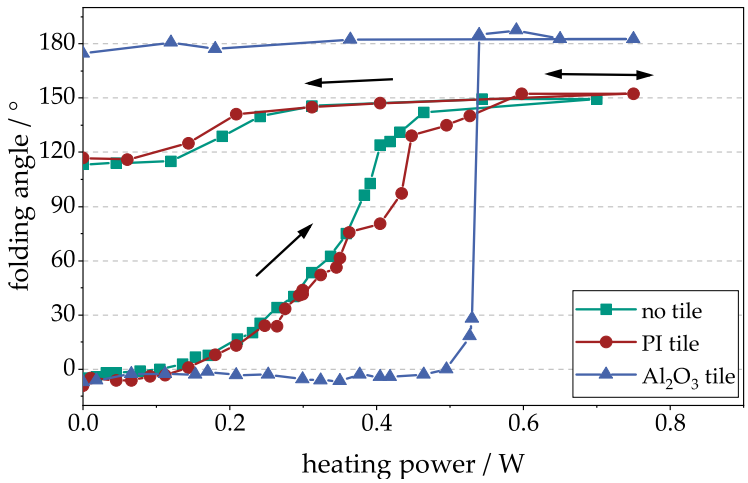

Figure 4.9.: Folding performance upon heating and cooling for different loads after unfolding to 0°.

The temperature of the folding hinge is measured by IR thermography while step-wise increasing the heating power. Figure 4.10 shows the unloaded case (*no load*). As the temperature increases proportionally to the heating power, its course is similar to the

graph in Figure 4.9. In the unloaded case the folding motion takes place approximately between 30 and 50 °C. This corresponds to the phase transformation range obtained by material characterization of TiNi.

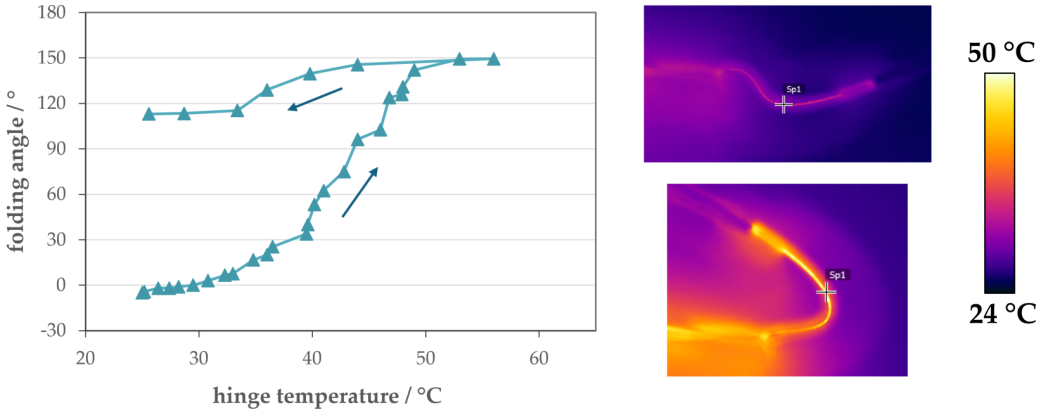

Figure 4.10.: Folding angle as a function of the hinge temperature for the case of *no tile* in Figure 4.9.

With the additional load of a PI tile (0.5 mN) the start of the folding motion requires a higher heating power and results in an increased folding angle by 5° upon heating. After cooling to room temperature, the folding angle is equally increased. The use of a ceramic tile (Al_2O_3) which causes a graviational load of 3.8 mN follows the observed trend. Instead of 0.1 W, a heating power of 0.5 W is required to initiate the folding motion followed by a steep transition to the folded configuration upon further heating. The actuator folds down to 183° and by subsequent cooling reaches the aimed folding angle of around 180°. These measurements show that additional loading can suppress possible second memory shapes and allows for tuning of the folding actuator.

Regardless of the orientation of the actuators and without any additional loads, there remains an opening angle after folding and complete folding to +180° cannot be achieved. Directly after annealing, a small opening angle is already visible as shown in Figure 4.5 (c). The change of the folding angle by cyclic loading is tracked (see Figure 4.11). Samples that are heat-treated in the vacuum oven for the 180° configuration, show a folding angle of 175° after their removal from the heat treatment jig and re-heating on a hot plate. After the additional assembly steps, including gap welding onto the Ni pads and glueing onto the tiles, the folding angle reduces to 165°. The folding actuator is unfolded to beyond -90° to remain in the 0° configuration. One temperature cycle (T-cyc.) consists of heating

above A_f (65 °C) and subsequently cooling to RT. The folding angle decreases further to approximately 160°. One explanation for this observation is the local overstraining which introduces non-recoverable plastic deformations within the SMA material. Repeating this heating and cooling cycle at the constraint position at 0° does not lead to an additional decrease of the folding angle. When the folding actuator is deformed and heated in the blocked -180° configuration, a further drop of folding angles occurs. A different folding angle between the heated (135°) and the cooled (145°) actuator also appears here for the first time. The formation of a two-way effect is due to the introduction of plastic deformation in the material. This trend of a decrease in the fold angle is intensified with five additional temperature cycles of heating up to 80° while constraining the actuator in the -180°. The resulting folding angle is 75° when the actuator is heated. The deviation of heated and cooled folding angle is not further increased. For different samples similar trends for the drop of folding angles were observed. The occurence of a second memory shape did also result in further lower folding angles. One example are the measurements as shown in Figure 4.9, where upon cooling the folding angle decreases.

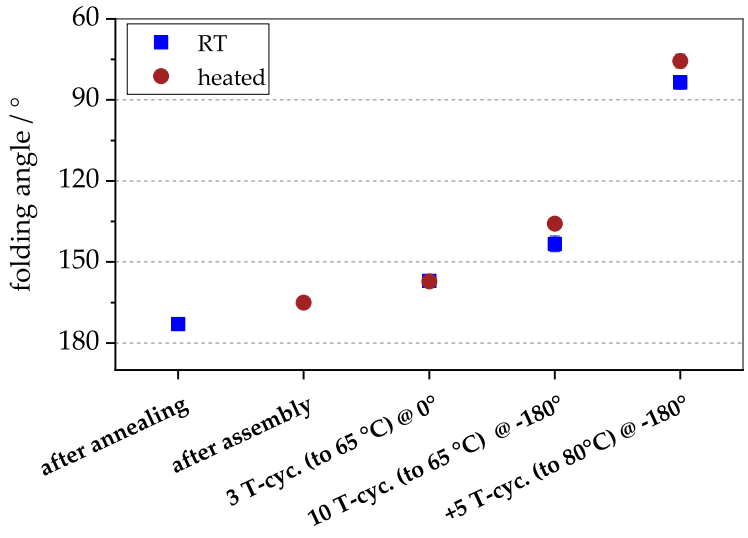

Figure 4.11.: Evolution of opening angle upon cyclic loading.

While the SMA structure was designed for bidirectional folding at +180° and -180°, the manufactured actuators are exposed to additional local overloads that lead to plastic deformations and prevent a complete return to the memory shape imprinted during heat-treatment. Furthermore, the cold-rolled TiNi foil contains small defects and can be locally sensitive to overstraining. However, for the free recovery of manually unfolded actuators

the difference between annealed angle (175°) and resulting angles upon heating (160°) is acceptable and is not subjected to further decrease when cycled 20 times. The extreme cases for constrained angles upon heating cause the major effects on the drop of folding performance. Especially over-heating should be avoided.

4.3.2. Bi-directional Folding Performance

For the use as a bi-directional folding actuator, the single actuators have to be characterized in terms of their generated bending moments during folding actuation and their opposing torque upon unfolding. These measurements allow for predicting the bi-directional folding performance.
In literature, two main experiments have been defined for uni-directional folding actuators [70]. The *blocked angle* measurement on unfolded active folding actuators provides information on the bending moments during shape recovery. The *blocked torque* measurement mimics the unfolding motion of a passive folding actuator and its opposing bending moment, generating a bending moment-angle diagram. It can be defined as the equivalent of a classical force-displacement characteristics but transferred to the bending case.

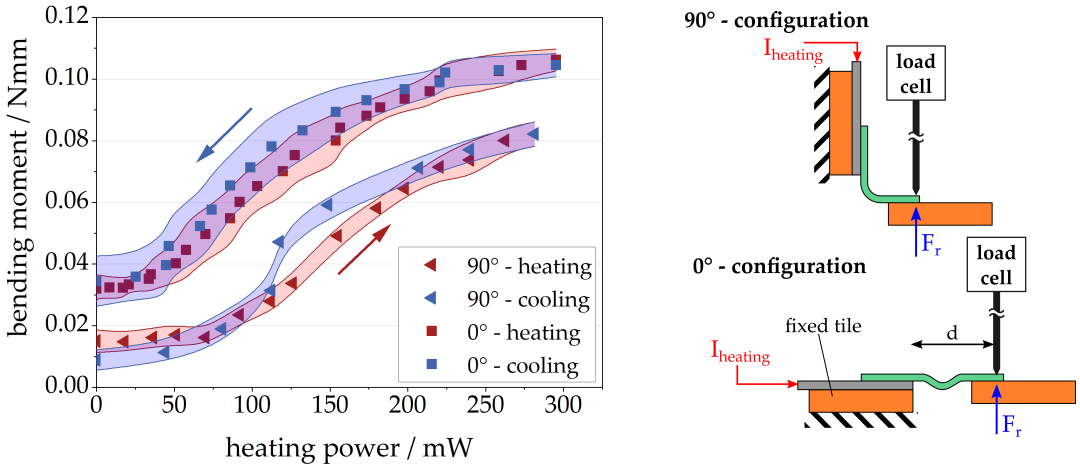

Figure 4.12.: Blocked angle measurement. The restoring force F_r of the folding actuator acts onto the load cell.

For the blocked-angle measurement the single folding actuator is positioned below a pin that is attached to a load cell. One tile is fixed onto a platform (see schematic in Figure 4.12) and the freestanding tile is unfolded to two different configurations (90° and 0°). When the heating current $I_{heating}$ is applied the shape recovery of the SMA folding hinge

is blocked and a restoring force F_r acts onto the load cell. The resulting bending moment is calculated by taking into account the distance d between the point of load application on the freestanding tile to the fixation. The shorter the "lever arm" d, the higher the forces to be measured. Therefore, the position of the load cell is chosen to be as closely as possible to the fixed tile. The bending moment versus heating power characteristic upon heating and cooling is measured. The shaded area represents the minimum and maximum values of the measured bending moments.

The specimen is tested for two heating and cooling cycles at $d = 4mm$. In the 90° configuration, a bending moment of 0.018 Nmm exists before heating which corresponds to the opposing unfolding moment. When heated, a maximum bending moment of 0.085 Nmm is reached at a heating power of 280 mW. Upon cooling, a small hysteresis can be observed that is related to the difference in forward and backward phase transformation temperatures of the SMA. The remaining bending moment of 0.01 mN differs from the initial bending moment before heating. This deviation can be associated to the formation of different martensite variants between free and constrained recovery.

The specimen is similarly tested in the 0° configuration. The initial and maximum bending moments are 0.031 and 0.11 Nmm, respectively. Thus, the bending moment generated upon heating is 3.5 times higher than the bending moment required to unfold the folding actuator to 0°.

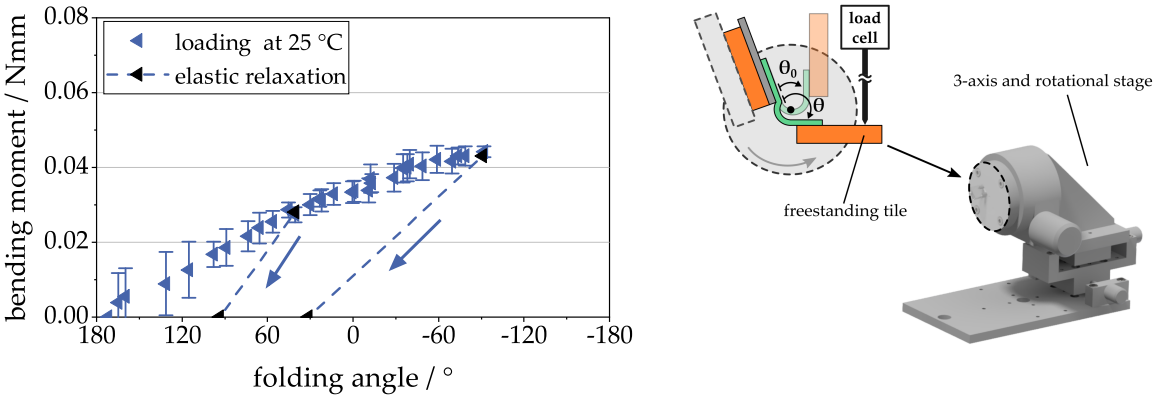

Figure 4.13.: Blocked torque measurement at RT and schematic of the test setup.

For the blocked-torque measurement two specimens are tested. The folding actuator is fixed on a rotational platform that allows for adjusting the opening angle θ (see schematic in Figure 4.13). The folding angle α derives from $\alpha = 180 - \theta$. Using the rotatable platform, the folding actuator is opened incrementally by the measuring

tip and the resulting force is recorded by the load cell. Here, the lever arm d varies upon unfolding ($d = 2..4mm$). Both, folding angle and distance d, are obtained by post-processing of recorded images of each measurement increment. Force measurement of small opening angles is difficult because the measuring tip is difficult to position in the confined space between the two tiles. This results in a high standard deviation in the bending moments for folding angles between 180° and 90°. A maximum bending moment of 0.043 Nmm is reached at a folding angle of -90°. After removing the load cell, the folding actuator returns to a folding angle of 30°. If the folding actuator is unfolded to 45°, the elastic relaxation leads to a folding angle of 95°.

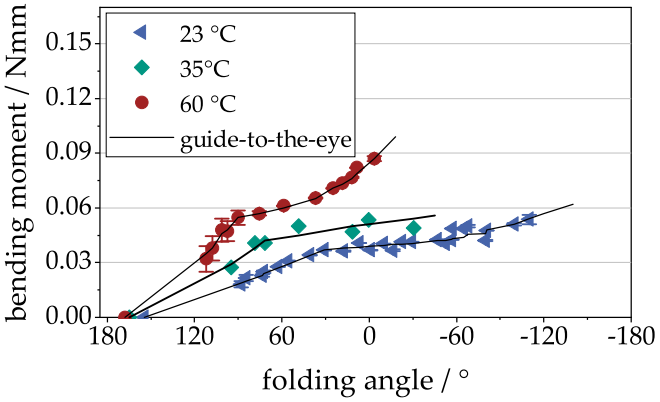

Figure 4.14.: Blocked torque experiments for three different hinge temperatures (23 °C, 35 °C and 60 °C).

The blocked torque measurement is performed at various temperatures. For this purpose the actuators are Joule heated. The temperature of the center of the hinge region is evaluated by an IR camera. The heating current is adjusted and kept constant until the average temperature stabilizes to ±1 °C. Figure 4.14 displays the folding angle vs bending moment curves at room temperature (23 °C) and hinge temperatures of 35 °C and 60 °C. For ease of reading, a guide-to-the-eye line is drawn over the measurement data. The opening angles vary for the different temperatures. Therefore, the starting angles α_0 for unfolding shift. At room temperature, the folding actuator is opened by 25° ($\alpha_0 = 155°$). When heated above the austenite finish temperature, the actuator folds down to $\alpha_0 = 170°$. As with the tensile tests, an increase in material stiffness can be observed at higher temperatures and the transformation plateau shifts to higher bending moments. At a hinge temperature of 60°, the hinge shows superelastic behavior upon loading and unloading. Therefore, it is partly or fully in austenite state. The unfolding to

0° at room temperature requires a bending moment of 0.038 Nmm. At 60 °C, the bending moment is around 0.085, thus more than two times higher.

The blocked torque measurements for the two extreme cases, at room temperature and in heated state (60 °C), allow to set up an actuation path diagram for bi-directional folding actuators. Figure 4.15 schematically displays the combination of two counteracting folding actuators, a protagonist shape-set to +180° (solid lines) and an antagonist shape-set to -180° (dashed lines). Combining both actuators after annealing by bonding their tiles as shown in Figure 4.6 results in an equilibrium position at 0° (E). Heating exclusively the protagonist leads to a folding motion towards the point (I-a) at the intersection of the two bending moment-angle characteristics of the cold antagonist and the heated protagonist. Subsequent cooling leads to the elastic relaxation of the folded antagonist and the equilibrium point (I-b) is reached. If the antagonist is heated in the next step, a direct folding actuation from (I-b) to (II-a) is possible, followed by the second equilibrium point (II-b) upon cooling. This graph shows that bi-directional actuation can be possible between +100° and -100°, with two stable positions at approximately +50° and -50°. These positions are determined by drawing a linear segment with a slope corresponding to the elastic relaxation slope at RT (see Figure 4.13).

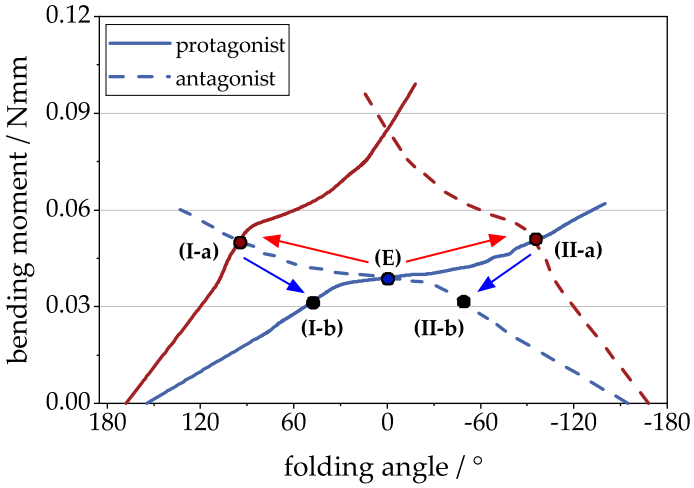

Figure 4.15.: Actuation paths of a bi-directional folding actuator. Selective heating of single actuators results in a maximum folding motion of around +100° (I-a) and -100° (II-a). Subsequent cooling leads to the two equilibrium points (I-b) and (II-b).

A coupled bi-directional folding actuator is fabricated as described. When the protagonist is actuated by a heating power of 320 mW (0.64 A, 0.5 V) the total folding angle reaches

+42° (±2°). The cooled equilibrium position (I-a) is at 9°. When the antagonist is heated with a heating power of 246 mW the bi-directional actuator folds to -40° and reaches the equilibrium point (II-b) at -6° upon cooling. Thus, reversible and bi-directional folding is achieved. The IR images of the four characteristic positions are shown in Appendix A.4.

The difference between the theoretical prediction of the folding performance and the experimental values can be attributed to additionnal coupling effects. In the blocked torque experiment the freestanding tile can freely move upon unfolding and shear forces are not measured. The motion of the coupled folding actuator is however mechanically constrained in in-plane direction of the tiles. Furthermore, due to the fabrication process, the zero-plane of both actuators is not coinciding but offset by the doubled thickness of the tiles and the bonding layer (by approximately 250 µm). This introduces an additional bending moment during actuation. Additional internal stress can be introduced by the fabrication process. The actively heated single actuator does also affect the passive actuator thermally and generates a higher opposing bending moment due to the stiffness increase. The thermal influence between the two opposing actuators can be decreased by increasing the separation between them. But a wider separation leads to a higher bending moment perpendicular to the folding axis.

4.4. Downscaling of Double-bridge Folding Actuators

The major limitation for downscaling the lateral dimensions of the folding actuator is the thickness of the used SMA material. Contrary to applications where exclusively tensile loading is applied, bending generates surface stresses that scale with the thickness of the bent material. As derived in section 4.2 the smallest possible bending radius and the minimum bridge length derive from the shear stresses at the outer bent surfaces. For the fabrication of miniaturized folding actuators the TiNi foil is reduced in thickness.

4.4.1. Foil Thickness Reduction

Several techniques for thickness reduction by subtractive processes are possible. Handling of thin films is delicate and micro milling and grinding introduce plastic deformation in the material. Therefore, wet chemical etching is chosen for a controlled thickness reduction. Films of 8 µm and 5 µm are fabricated by double-sided etching in a HF:HNO3 etching solution in a petri dish. The etching rate is higher at the beginning

of the etching process due to the native oxide layer of the TiNi foil that gets removed by HF. The averaged etch rate of different etch tests is 1.65 µm/min. The defects and inhomogeneities of the initial cold-rolled foil cause a non-uniform thinning of the etched foil. Furthermore, an increase in roughness of the thickness-reduced films is observed. Figure 4.16 (a) shows an etched film with etch holes and dents. Additionally, increased waviness and inhomogeneous edges can occur. Figure 4.16 (b) shows the variance in film thickness of a 40 x 15 mm² TiNi foil after wet etching. The film thickness increases towards the edges.

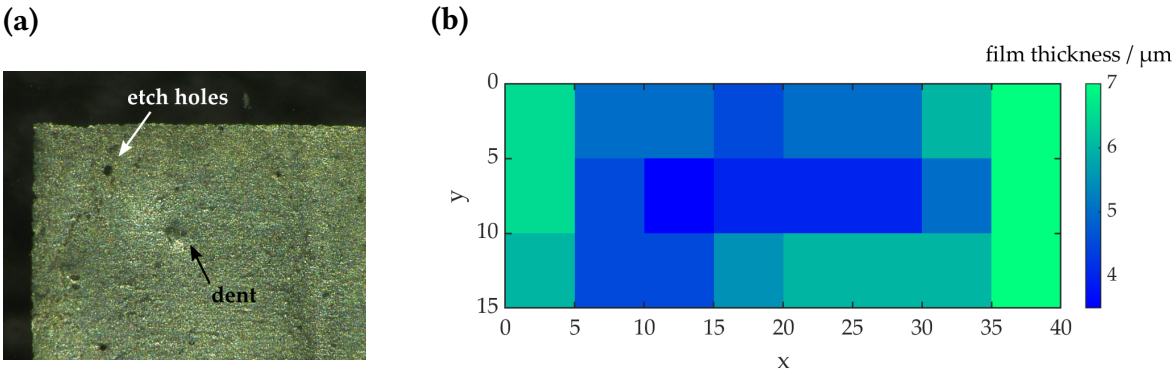

Figure 4.16.: (a) TiNi foil defects after etching. **(b)** Film thickness distribution across sample.

4.4.2. Fabrication of Miniaturized Folding Actuators

The thinned TiNi foils allow for downscaling of the double-bridge design. Structuring of the miniaturized layout by Nd:YAG laser cutting highly affects the SMA material. As shown in Figure 4.17 (a), the heat affected zone (HAZ) due to the laser ablation process distributes widely into the relevant areas of the folding hinges. Oxidation and depletion of Ti due to high temperatures impacts the SMA properties and should be avoided. Therefore, structuring by photolithography and wet etching is the preferred technology to fabricate miniaturized folding actuators.

Figure 4.17 (b) shows a TiNi foil after HF:HNO3 wet etching. Smallest hinge widths of 30 µm are achieved for functional actuators structured by wet-etching at a minimum thickness of 5 µm. The structured actuator is transferred and bonded to a polyimide tile. Tinned copper wires of 100 µm thickness are electrically contacted to the pad areas of the SMA structure by a two-component conductive adhesive (EPO-TEK H20E). The wires are connected to a source-measurement unit (SMU) for Joule heating and 2-wire resistance measurement.

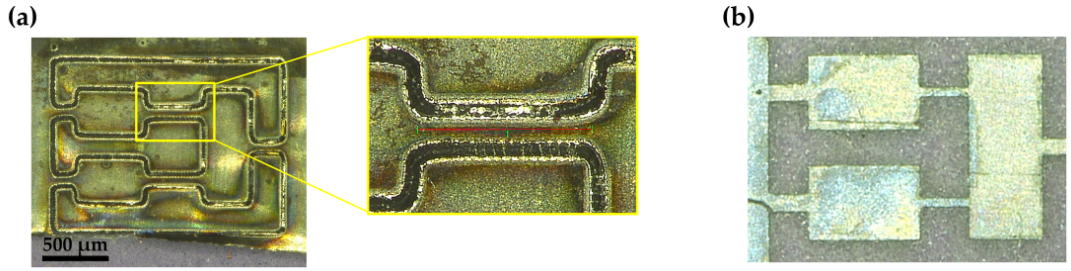

Figure 4.17.: (a) Laser cut structure with surface oxidation and rough edges. **(b)** Wet-etched actuator structure on heat-releasable film.

The shape-setting to the +180° folding angle is performed by Joule heating. The small size of the miniaturized actuator does not allow for an IR measurement of the actual surface temperature during heating. A simulation model is used to approximate the local temperature in the hinge region and to predict the required heating current for re-annealing. For the annealing step, the actuator is placed on a 3-axis positioning platform and folded into the 0° position by a manipulator tip. 8 µm thin actuators with hinges of 250 µm length and 30 µm width are shape-set with an annealing current of 110 mA (approx. 45 mW) for 10 s. A bending radius of 46.1 µm is measured (±13.1 µm).

4.4.3. Characterization of Miniaturized Folding Actuators

The unidirectional folding performance is characterized by the free recovery of a deformed miniaturized actuator upon heating. Figure 4.18 shows the actuation sequence of a 5 µm thin actuator with hinges of a length of 500 µm and a width of 75 µm. The folding actuator is quasi-plastically deformed to the 0° position (a). Heating with a heating current of 50 mA (approx. 10 mW) generates a folding motion (b) and a maximum folding angle of 145° (c) is reached. Upon cooling, re-unfolding due to the two-way shape memory effect results in a folding angle of approximately 110°.

The bending moment of a miniaturized folding actuator is measured with an elastometer. The unidirectional actuator has hinge dimensions of 250 µm x 30 µm x 8 µm. The measurement tip that is connected to a load cell is positioned above the center of the free-standing tile. By Joule heating the actuator, the folding motion is blocked and a load is applied onto the measurement tip. The weight value displayed on the elastometer screen is converted into a force value and multiplied by the lever arm between measurement tip and tile fixation. Figure 4.19 shows the derived bending moment versus Joule heating current. The drift of the elastometer results in negative readings for small currents. At a heating cur-

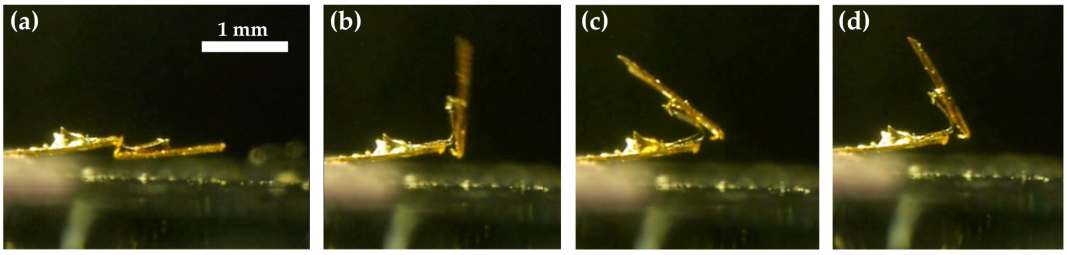

Figure 4.18.: Folding sequence of a miniaturized folding actuator (500 µm x 75 µm x 5 µm hinges) with polyimide tile annealed for 180° fold. **(a)** unfolded to 0°, **(b)** during actuation by Joule heating, **(c)** maximum fold angle of 145°, **(d)** re-unfolding upon cooling.

rent of 20 mA the bending moment increases due to the phase transformation and reaches a maximum value of 0.13×10^{-3} Nmm.

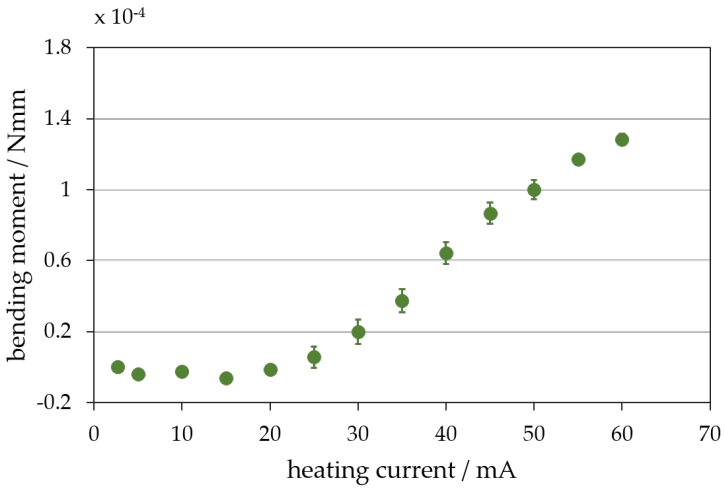

Figure 4.19.: Blocked angle measurement of miniaturized folding actuator (250 µm × 30 µm × 8 µm hinges)

4.5. Discussion

For mm-sized folding actuators uni- and bi-directional folding using a 20 µm TiNi foil is achieved. The uni-directional folding actuators can generate bending moments of up to 100 mNmm when heated and folds up to +150°. It requires an additional load of 3.8 mN to reach the maximum folding angle of +180°. To reduce this remaining opening angle, shape setting beyond +180° is an option. While this is possible at larger scale, curling in a con-

strained space and at small scale is not possible. Another explanation for the incomplete angle recovery is the observation that manual unfolding by rotating the freestanding tile does not lead to a completely flat SMA hinge. Its folded geometry is still visible (compare Figure 4.10) and the SMA foil experiences the maximum strain close to the fixed tile because the separation between the two rigid tiles is not kept constant. By introducing an additional compliant hinge that ensures the separation of the tiles and thereby elongates the SMA hinge towards a flat geometry upon unfolding, could further enhance the uni-directional angular folding range. However, additional stiff elements will also reduce the performance.

The bi-directional folding performance has been studied in detail to predict the possible angular folding range. The measured angles are lower due to mechanical and thermal coupling effects of the bonding partners. The theoretical prediction of bi-directional folding between +100° and -100° is also not sufficient for some applications especially for Origami-inspired 3D structures. If the uni-directional folding performance can be increased, the bi-directional folding range does also increase due to the shift of the actuation paths towards the outer edges (compare Figure 4.15). The mechanical coupling between the two pairs of tiles can be reduced by introducing an additional degree of freedom to allow for a relative motion between the two tile surfaces. Thereby the tiles can accommodate to the folding motion and additional stresses affecting the angular folding range, could be reduced.

The miniaturization by reducing the thickness of the TiNi foil has been studied. A 5 µm thin miniaturized folding actuator achieves uni-directional folding up to 145°. Its lateral dimensions are decreased by approximately one order of magnitude. Compared to the mm-sized folding actuator based on the 20 µm TiNi foil, the actuation bending moment is decreased by three orders of magnitude down to 0.13 mNmm. Due to the surface defects of the cold-rolled TiNi foil and the inhomogeneous surface etching, the further downscaling is at its limit here.

5. Cascaded Double-bridge Actuators for Multi-Stage Folding

The double bridge structures presented in the previous chapter represent the simplest layout for the realization of one-sided Joule heated folding actuators. With the overriding aim of achieving the widest possible bi-directional folding and the ambition for further miniaturization, changes must be made to this basic layout. The use of sputtered thin films enables a subtractive microfabrication process resultin in ever smaller structures by using standardized handling techniques in a cleanroom environment.
In the following, the sputtered TiNiCu thin films are characterized using the same methods as those employed for cold-rolled TiNi foils. The relevant parameters are derived from the material characterization data and are employed to design a new layout involving the serial connection of two double-bridge folding hinges. A simulation model is set up to study the parameters. The extended fabrication process required for micro-structuring and assembly is described in detail.
To evaluate the impact of the altered starting material, both the updated design and a simplified double-bridge structure are examined. Identical structure sizes are used for both, and they are created using the same fabrication process. This allows for a direct comparison of their folding performance.

5.1. Material Characterization of TiNiCu films

TiNiCu films with a layer thickness of 6 µm are provided by cooperation partners from CAU Kiel for this work. The chemical composition of these thin films is $Ti_{53.9}Ni_{30.4}Cu_{15.7}$ as obtained by XRD measurements.
Binary TiNi shape memory alloys show a constrained composition variation for the shift of phase transformation temperatures by thermal treatment. The addition of Cu as ternary alloy element allows for easier tuning of the phase transformation temperatures. Additionaly, the sputter-deposited films' thickness is more homogeneous with less defects on the surface, contrary to the cold-rolled TiNi foils.

The TiNiCu material is sputtered onto a sacrificial Cu layer and a Ta adhesion layer on a wafer. The 6 µm thin film is released from the substrate by wet-etching the sacrificial Cu layer and is crystallized by rapid thermal annealing (RTA) at 700 °C for 15 mins in a vacuum chamber. The detailed fabrication process is described in [78].
Figure 5.1 displays the DSC measurement of the as-received 6 µm TiNiCu thin film. Contrary to the binary TiNi material, one observes one-step phase transformations on heating (M-A) and cooling (A-M) without any intermediate phase. Upon heating the martensitic transformation takes place between 56.6 °C (A_s) and 68.6 °C (A_f). The derived phase transformation temperatures upon cooling are 55.5 °C (M_s) and 44.8 °C (M_f). The latent heat for M-A transformation is 12.7 J/g and for A-M transformation -13.1 J/g.

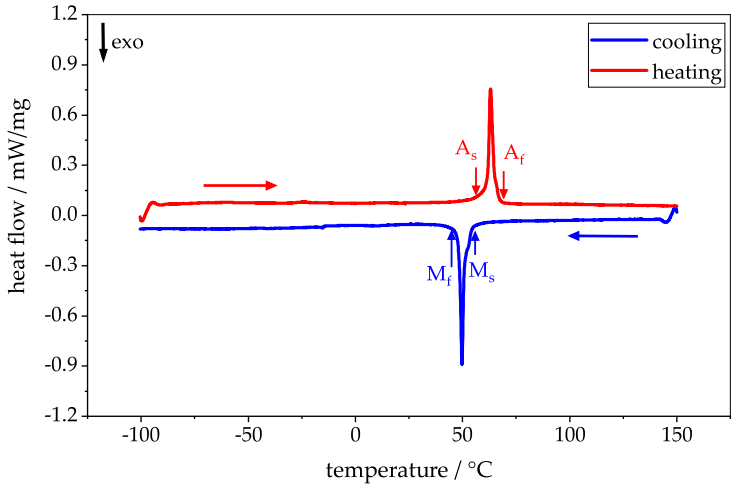

Figure 5.1.: DSC measurement of TiNiCu thin film after pre-annealing at 700 °C for 15 min. The phase temperatures are labeled by arrows.

The four-point probe resistance measurement in the cryostat provides information on the change in electrical resistivity of the freestanding TiNiCu thin film (see Figure 5.2). The approximated phase transformation temperatures upon heating are 50.8 °C (A_s) and 67.6 °C (A_f). On cooling, the reverse transformation takes place between 57.7 °C (M_s) and 44.5 °C (M_f).
Only small deviations in phase transformation temperatures between the two measurement methods are observed, thereby confirming the measurements. The results reveal the electrical conductivity, phase transformation temperatures, heat capacity and thermal conductivity of 6 µm sputtered TiNiCu. These material parameters are summarized in Table 5.1.

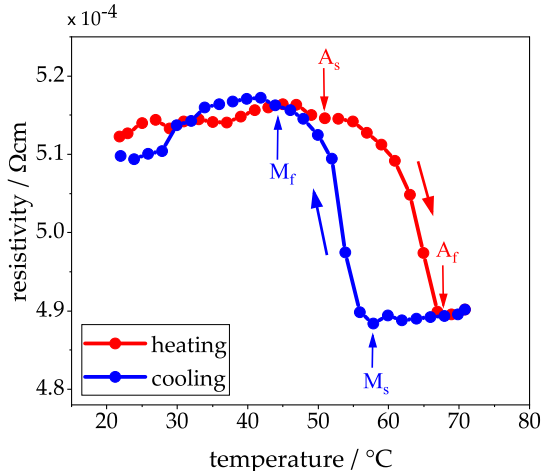

Figure 5.2.: Electrical resistivity of freestanding 6 µm TiNiCu thin film upon heating and cooling.

The thermo-mechanical material properties of the pre-annealed TiNiCu thin films are obtained by tensile testing. For this purpose, the dog-bone shaped specimens are fabricated by photolithography and wet etching. A tensile holder adapted to the dogbone shapes is manufactured in brass. Thereby it is possible to vertically align and clamp the 6 µm thin samples by friction/form fit connection.
Figure 5.3 (a) shows the loading and unloading curves obtained at three different ambient temperatures in a heating chamber. At room temperature the sputtered TiNiCu thin film shows the shape-memory effect. When it is quasi-plastically deformed to about 2.9 %, a strain of 1 % remains. It can be fully recovered by heating. The material shows a maximum recoverable strain of 4 %. For higher temperatures the critical stress for transformation increases as shown in Figure 5.3 (b). The Clausius-Clapeyron coefficient of 2.87 MPa/K is derived by the linear approximation of experimentally obtained values of the start of stress plateaus. At 65 °C, the material shows pseudoelastic behavior and strain is completely recovered upon unloading. At 80 °C, the critical stress for re-orientation of martensite variants at loading and unloading shifts to further higher stresses. All curves show a rather large slope of the stress plateau and a small hysteresis.

Appendix A.5 provides more information on the change of effective elastic modulus for increasing temperature. It is associated with the change of crystal structure from martensite to austenite state. For the use as a temperature-dependent variable in simulation models, the elastic modulus is approximated by the dotted function. A constant value of 15 GPa is assumed when the temperature of the material is below martensite

finish temperature. Above austenite finish temperature, the elastic modulus amounts to 41.5 GPa. Between the two limiting phase transformation temperatures, the change of the effective elastic modulus is defined as a linear function.

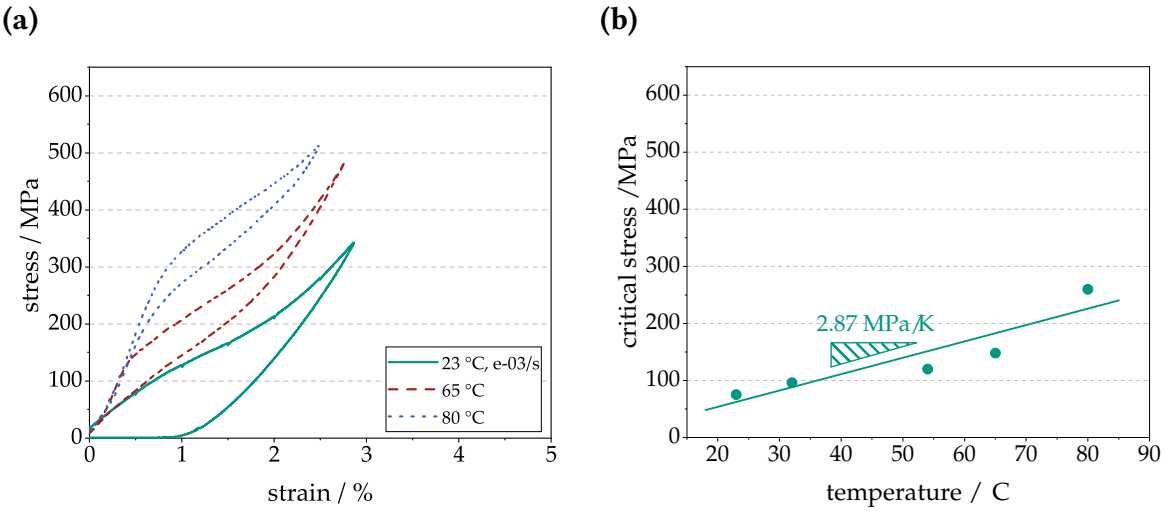

Figure 5.3.: **(a)** Tensile loading and unloading of pre-annealed 6 µm TiNiCu film at different ambient temperatures in a temperature chamber. **(b)** Change of critical transformation stress for different ambient temperatures and linear fit.

Table 5.1 shows a summary of all experimentally obtained parameters of the 6 µm pre-annealed TiNiCu thin film. The values are used in simulation models and are provided to cooperation partners.

Parameter	**Symbol**	**Value**	**Unit**
Young's modulus (martensite)	E_M	15	GPa
Young's modulus (austenite)	E_A	41.5	GPa
Critical stress (at RT)	σ_{cr}	87	MPa
Clausius-Clapeyron coefficient	C_{MA}	2.87	MPa/K
strain limit (at RT)	ε_{max}	0.04	-
Specific heat capacity (at RT)	c_p	420	J/kg/K
Thermal conductivity (martensite)	k_{th}^M	1.4	W/m/K
Thermal conductivity (austenite)	k_{th}^A	1.5	W/m/K

Table 5.1.: Summary of experimentally derived parameters for 6 µm TiNiCu (sputter-deposited, annealed for 15 min at 700 °C).

5.2. Design and Simulation

The basic design of the double-bridge folding actuator is extended by cascading two double-bridges that form two individual hinge pairs. The new design is referred to as *Cascaded Design*, whereas the basic layout is called *Single Hinge Design*. The new layout consisting of the two hinge pairs HP1 and HP2 is shown schematically in Figure 5.4 (a). By shape-setting the two hinge pairs HP1 and HP2, the overall folding angle is increased. The two folding axes of the cascaded hinge pairs are aligned as closely as possible, to keep the overall size compact compared to the single hinge layout. Furthermore, the folded geometry provides additional in-plane flexibility which accommodates stiffening effects during bending and improves bi-directional folding. The dimensions of the pad-like structures, connecting HP1 and HP2 are chosen as large as possible. They serve as electrical contacts for annealing HP1. Interconnecting the two outer pads on tile 1 allows for shape-setting of HP2 and actuation of the total cascaded SMA hinges. The two inner pads serve for resistance monitoring during actuation by four-point probe resistance measurement.

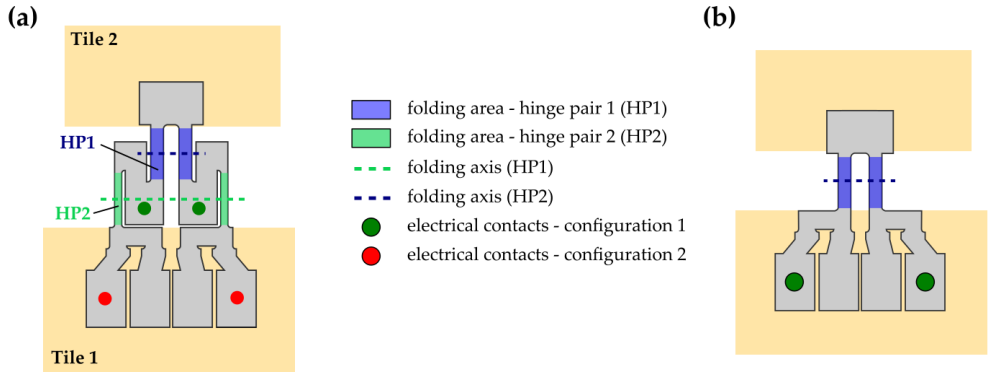

Figure 5.4.: Schematics of SMA folding hinge layouts: **(a)** Cascaded Design with two folding hinge pairs HP1 and HP2, **(b)** Single Hinge Design with one folding hinge pair HP1.

The bending radius r, the hinge length l and the width w of the two hinge pairs have to be adjusted. The minimal bending radius r_{min} is derived from the thickness of the TiNiCu film (t_{SMA}= 6 µm), the maximum admissible strain ε_{max}, and the desired angular folding range β. HP1 should bend in the range of +160 and -140° (β = 300°) after being heat treated at a constraint angle of +180°. Hinge pair HP2 is set for +90° memory shape and thus, unfolding between +80° and -180° (β = 260°) should be enabled. It can be assumed that the combined folding angles cover the total range of ± 180°. For β equal to 300° the

minimum bending radius r_{min} derives to:

$$r_{min} > t_{SMA}\left(\frac{1}{|\varepsilon_{max}|} - 1\right)\frac{\beta}{360°} = 120\,\mu m \tag{5.1}$$

The resulting minimal length is: $l_{min} = \pi r_{min} = 377\,\mu m$. A length l equal to 400 µm is chosen for each hinge pair.
The bridge widths w_{br} of the two hinge pairs are chosen to allow for separated shape setting. First, HP1 is electrically interconnected in configuration 1 (see Figure 5.4), the double bridge highlighted in blue is deformed to +180° and Joule-heated for annealing. The shape-setting of HP2 is performed by electrically connecting the SMA in configuration 2 and folding the double bridges into a +90° fold. During the second heat treatment step, the temperature of HP1 must remain below the recrystallization temperature to avoid "re-programming". Therefore, the width pairs have to be chosen in a suitable ratio.

A thermo-electrical simulation model is set up in COMSOL Multiphysics for the cascaded actuator design to study the temperature distribution across the actuator length for different width ratios and to estimate the required currents for shape-setting and actuation. The 3D geometry of the model is depicted in Figure 5.5.

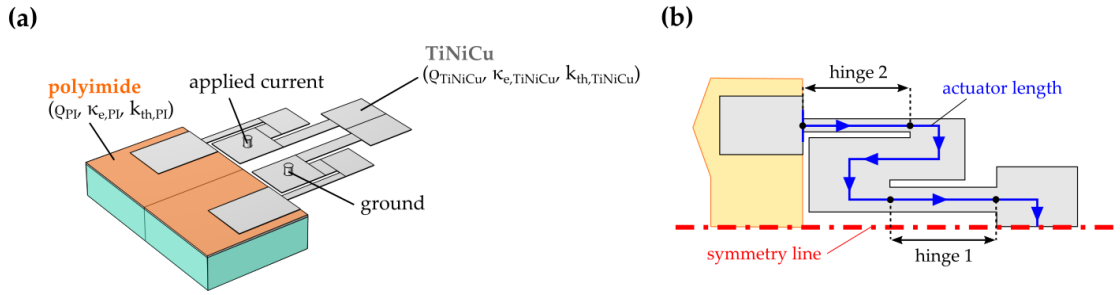

Figure 5.5.: (a) Geometry and material selection for finite element model, **(b)** Definition of the actuator length.

The 3D structure is surrounded by air. For each configuration, a current $I_{heating}$ is applied on one pad and the ground is set on the other pad. A current conversation over the total volume of the TiNiCu structure is applied and the entire 3D structure is electrically isolated. The heat convection strongly depends on the volume-to-surface ratio of the material. For dimensions below 1 mm, the convection coefficient is inversely proportional to the size. The further parameters of TiNiCu are selected from the material characterization data in Table 5.1. The properties of the polyimide tiles are chosen from DuPont datasheet

[89] (see Appendix A.6.). The heat transfer coefficient for convective cooling is given by a fourth-degree polynomial function of temperature T according to [90]:

$$h(T) = -4.034 \times 10^{-7}\, T^4 + 0.0001654\, T^3 - 0.02586\, T^2 + 2.07\, T + 41.96, \qquad (5.2)$$

where the temperature T is defined in °C and the heat transfer coefficient h in $Wm^{-2}°C^{-1}$. The electric potential field and the total generated heat by electric heating are solved by the electric current conservation equation. The temperature distribution along the actuator length (see Figure 5.5 (b)) is derived by a heat transfer model.

The simulation results are compared to the IR measurements of a fabricated cascaded actuator. To comply with the resolution of the IR camera, the minimum feature size of the fabricated actuator should be larger than 50 µm. The local temperature distribution across the actuator structure is evaluated along line segments (Li1-Li6) in the center of the hinges as shown in Figure 5.6. The dashed line indicates the contour of the actuator structure. Li3 and Li5 capture the temperature of HP1, Li1 and Li6 the temperature of HP2 for different heating currents. Because the focus plane of the IR camera does not align to positioning plane of the fabricated actuator, the temperature measurements cannot be expected to be fully symmetric.

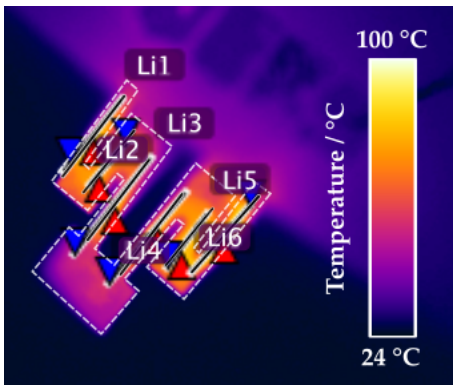

Figure 5.6.: IR measurements of the actuator along line sections Li1 to Li6. The accuracy of temperature measurement is approximately ±2 K.

Figure 5.7 shows the experimental values versus the simulated temperature distribution for four different heating currents along the actuator length as defined in Figure 5.5 (b). The temperature range for actuation, which is limited by the phase transformation temperatures M_f and A_f, is highlighted in light blue. With a broader width of HP1, HP2

is first to undergo the phase transformation at lower heating currents. Increasing the heating current further, HP1 starts its phase transformation while HP2 is already almost completely in austenite state. A good fit of simulation and experiment can be observed which allows an estimation of annealing and actuation currents.

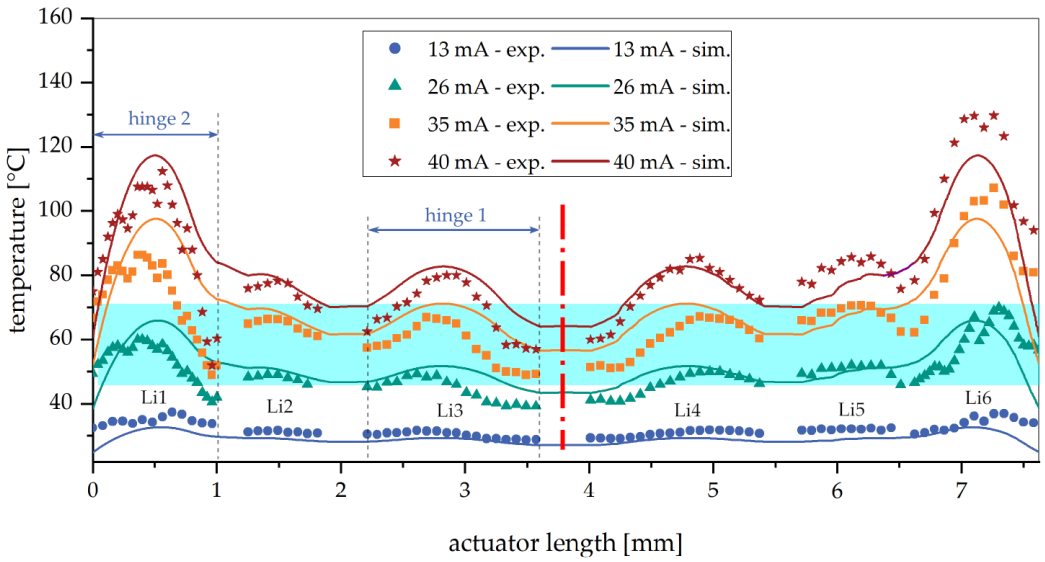

Figure 5.7.: Temperature distribution along the actuator length according as measured by IR thermography and simulated. The red dashed line indicated the symmetry line of the actuator. The temperature range of martensitic phase transformation ($M_f < T < A_f$) is highlighted in light blue. Experimental values are evaluated along the line sections as shown in Figure 5.6.

The temperature distribution is simulated for the two annealing configurations shown in Figure 5.8 (b). The annealing region is highlighted in green. Its limits are chosen according to experimental observations for resistive annealing at atmospheric conditions between 420 and 700 °C. As shown in Figure 5.8 (a), the total length of the two hinge regions reaches the annealing temperature range required for shape setting. A large temperature gradient occurs along the hinge sections. Therefore, different phase transformation properties can be expected.

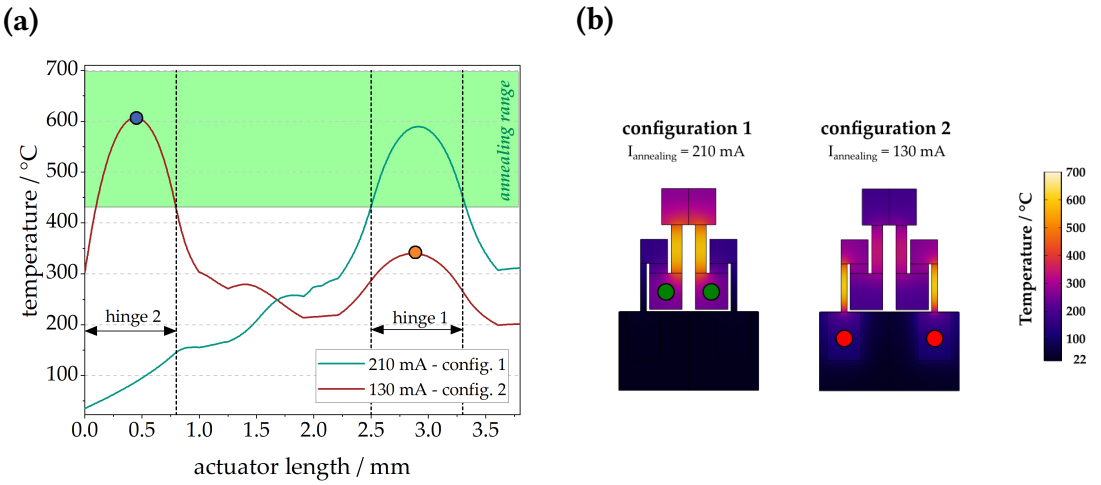

Figure 5.8.: **(a)** Evaluated temperature distribution along the actuator length (due to symmetry only half of the actuator is visualized), **(b)** Surface temperature distribution for the two annealing configurations.

In order to find a suitable ratio of the hinge widths, different combinations are studied. Figure 5.9 shows the maximum temperatures in the two hinge regions as a function of the annealing current. The maximum temperatures are located in the center of the hinges, as illustrated by the colored dots in Figure 5.8. In a two-step annealing process, HP1 is shape-set in the first step. The annealing of HP2 does thermally affect HP1 and to avoid re-crystallization HP2 should remain sufficiently below the annealing range.
For a width ratio w_{HP2}/w_{HP1} = 0.78 (b), the maximum temperatures evolve closely for increasing heating currents. While at a heating current of 170 mA, HP2 reaches the optimum annealing temperature, HP1 is approaching its (possible) re-crystallization temperature. For a width ratio of 0.67 (b), the two hinge pairs reach a temperature difference of 200 K at a heating current of 150 mA. The trend is further followed for a width ratio of 0.56 (c). Here, a temperature difference of 250 K can be reached at a heating current of 130 mA, whereby HP1 remains below 400 °C. Despite possible current fluctuations and small defects in the structure, overheating can be avoided. The simulations thus suggest an optimal hinge width ratio of 0.6 for the fabrication of folding actuators actuators. The respective annealing currents for HP1 and HP2 (210 mA and 130 mA) are derived from the simulation model. Figure 5.8 (a) shows the resulting temperature distribution during selective annealing.

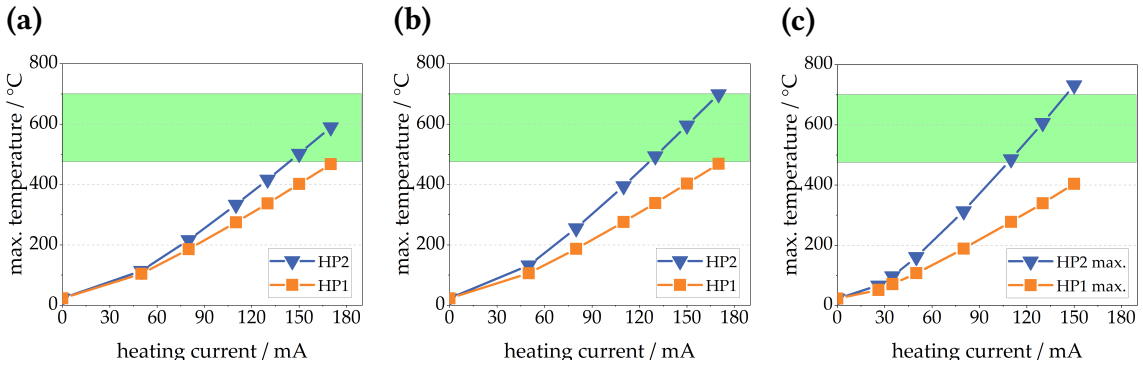

Figure 5.9.: Maximum hinge temperatures of HP1 and HP2 as a function of annealing current in configuration 2 for three different hinge width ratios: **(a)** w_{HP1} = 180 µm, w_{HP2} = **140** µm - w_{HP2}/w_{HP1} = 0.78; **(b)** w_{HP1} = 180 µm, w_{HP2} = **120** µm - w_{HP2}/w_{HP1} = 0.67; **(c)** w_{HP1} = 180 µm, w_{HP2} = **100** µm - w_{HP2}/w_{HP1} = 0.56.

5.3. Microstructuring Process and Experimental Setup

Starting from sputter deposited freestanding TiNiCu thin films (see Figure 5.10), the folding actuators are microstructured by photolithography. In step (I), the 6 µm film is laminated onto a thermal release tape. To prevent the formation of wrinkles, the SMA film is fixed to a polymer film by static attraction and rolled up between two spring-loaded rollers. After cleaning and dehydrating the surface, a 10 nm thin Cr layer is vapor-deposited as an adhesive layer for the subsequent 50 nm gold layer (III). This combination of Cr/Au thin film serves as an etch-stable hard mask after structuring. The AZ1505 photoresist is applied 1 µm thin for structuring. Using DLW, the layout of the TiNiCu folding structures is written into the photoresist (IV). After development of the photoresist, the Cr/Au layer can be etched (V). The photoresist is stripped to avoid organic impurities in the further etching process. The TiNiCu film can then be structured using HF:HNO_3 etching solution. The etching rate is approximately 1.5 µm / min. After removal of the hard mask only the TiNiCu structures remain on the thermal release tape. The structures can be easily released from the tape (VII) and transferred to the polyimide tiles (VIII) when the substrate is heated above 100 °C on a hot plate. The polyimide tiles were structured using laser cutting and are dispensed with a 2-component epoxy adhesive. The composite of SMA film, epoxy adhesive, and polyimide tiles cures on a hot plate at 150 °C within 3 minutes. The pads on the substrate can then be electrically contacted using copper wires, which are bonded to the pads with a silver adhesive (IX). This adhesive must also be allowed to evaporate on the hot plate for 15 minutes to harden.

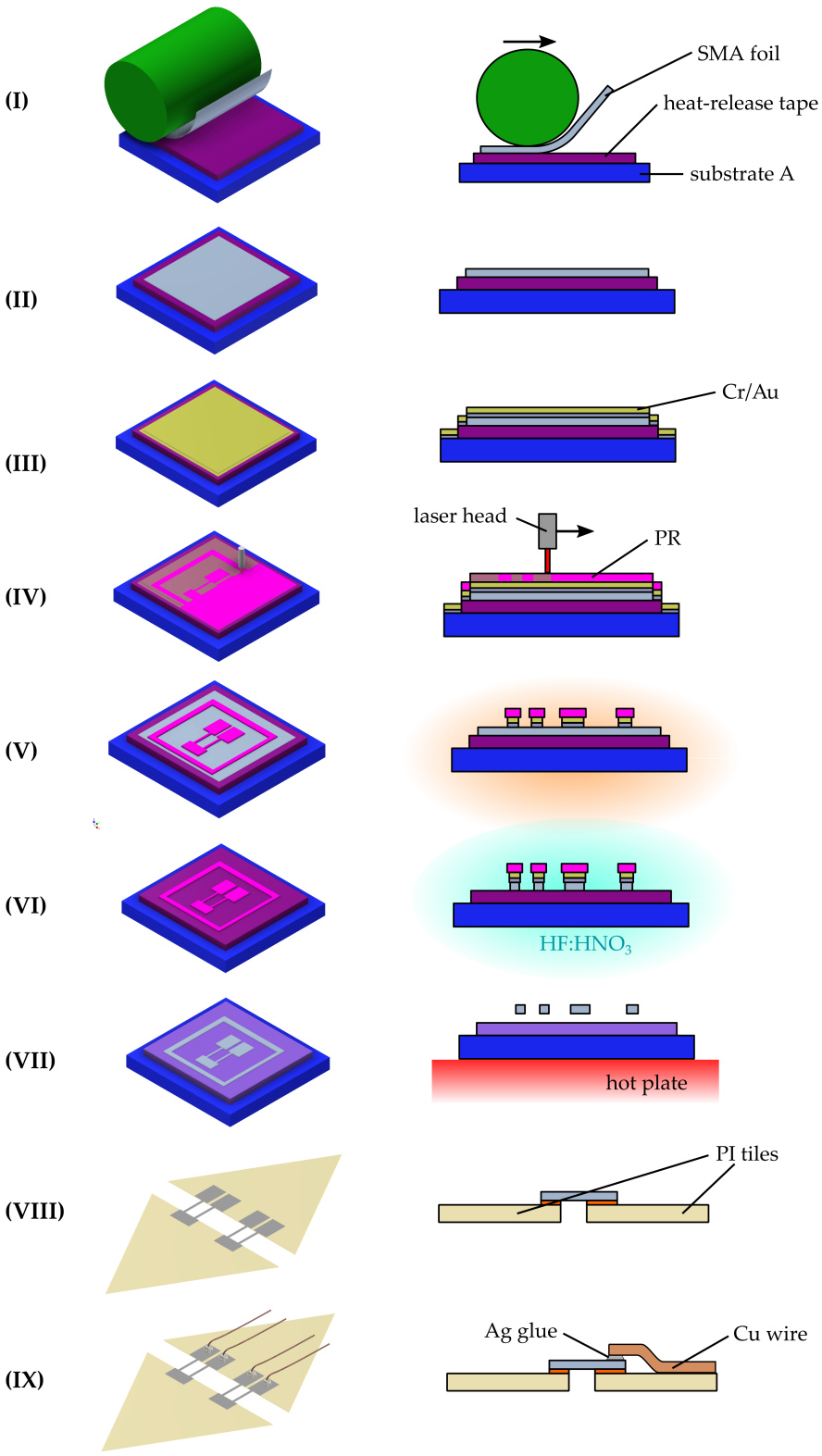

Figure 5.10.: Overview of fabrication process for micro folding actuators based on lithographically structured TiNiCu thin films and laser-structured PI tiles.

Folding actuators in different size scales are fabricated, among which two sizes are fully characterized. The "large" actuators have the dimensions as simulated in the previous section (hinge widths of 100 and 180 µm). The "smaller" actuators are scaled by a factor of 0.5, and thus have hinge widths of 50 and 90 µm. The annealing currents have been determined by simulation as 80 and 170 mA, respectively.

Figure 5.11 exhibits microscope images of selected fabrication steps. The result of the wet-etching process step (V) for structuring the Cr/Au mask is shown in Figure 5.11 (a). The 50 nm Au layer and 10 nm Cr layer are removed revealing the TiNiCu film. Underetching takes place and can be identified by the grey layer around the structure. The subsequent HF:HNO_3 etching step removes the uncovered TiNiCu film. The heat-releasable tape with its rough structure becomes visible (see Figure 5.11 (b)). Figure 5.11 (c) shows the folding actuator after gluing of the released TiNiCu structure onto a PI tile.

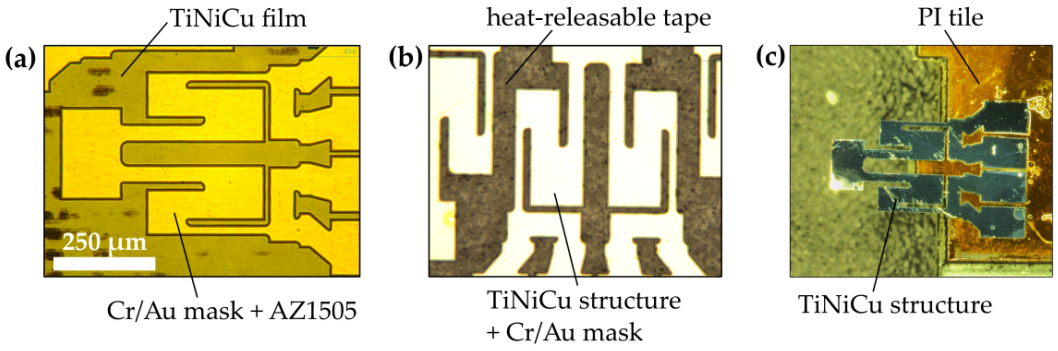

Figure 5.11.: Microscope images of fabrication steps: **(a)** Cascaded design structure after etching of the Cr/Au hard mask (step (V)); **(b)** structures after HF:HNO_3 etching of TiNiCu (step (VI)); **(c)** released and glued TiNiCu structure on PI tile (step (VIII)).

Compared to chapter 4 the experimental setup must be adapted. The size of the folding actuators is significantly reduced, and the heat treatment is carried out exclusively using Joule heating. For the two-step annealing process, the free-standing pad-like structures of the cascaded actuators must be temporarily contacted.

The test setup is schematically shown in Figure 5.12. It consists of a platform (white) that is mounted onto two linear stages (green). The folding actuators can be positioned onto

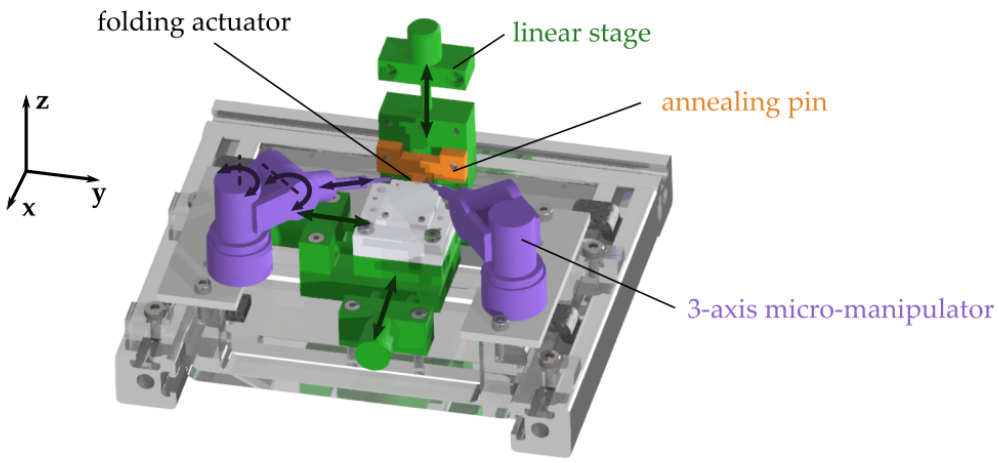

Figure 5.12.: Annealing and test setup for micro folding actuators including linear stages (green) and micro manipulators (purple).

the platform and be moved in x and y direction. An adapter with an annealing pin can be mounted onto the third linear stage that moves in z-direction. Thereby the actuator can be manually folded into the desired folding angle for annealing. Two micromanipulators (Kleindiek, purple) provide the electrical connection. They can move by two rotational and one linear axis and are equipped with a low-resistance probe tip holder in which a tungsten probe tip is inserted. A high precision source supplies the current for annealing and actuation. A camera is positioned in y-direction to record the folding angles of the folding actuators. The platform is positioned underneath an optical microscope in z-direction that additionally serves as light source. The positioning of the micromanipulators can be tracked via the camera in y-direction and the microscope in z-direction.

5.4. Single Stage Folding Actuators Based on TiNiCu Films

For comparison with the extended cascaded folding actuator, a single hinge design actuator is manufactured based on the layout in Figure 5.5. The lateral dimensions are based on the lengths selected for the cascaded actuator. The hinge width w_{br} is 50 µm. The length of the hinges, or the separation between the two polyimide tiles, is 400 µm. The hinge pair is bent into the 180° configuration with the annealing pin and shape-set with an annealing current of 170 mA. Figure 5.13 shows the resulting folding angle for different annealing times of single hinge actuators annealed with a 170 mA annealing current.

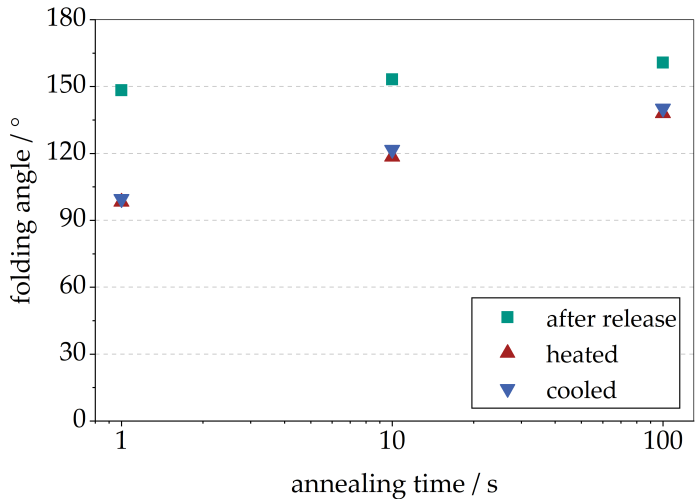

Figure 5.13.: Folding angles for different annealing times. The release angle corresponds to the folding angle directly after the shape setting and removal of the constraining pin. After manual unfolding, the heated and subsequently cooled folding angles are measured.

Short-time annealing (1 s) results in a folding angle of 149° after releasing the annealing pin. Subsequent unfolding, followed by a heating and cooling cycle results in a recovered angle of 111°. When the annealing time is increased, the memory shape shifts to higher angles but the difference between heated and cooled state also increases by a few degrees. Thus, a small two-way shape memory effect is introduced. In the heated state a maximum folding angle of 140° is achieved. If a higher annealing current is chosen, the surface starts to show large amounts of oxidation and upon cooling more pronounced unfolding occurs. To obtain a large folding angle after annealing it is not possible to completely avoid the two-way shape memory effect that occurs due to local overheating and overstraining.

Figure 5.14 shows the evolution of the resistance of the cascaded SMA hinge upon heating. Here, the actuator is interconnected in configuration 2 for annealing of HP2 and two distinct zones can be detected. When the current is raised, the resistance increases due to the heating of the structure. Between 15 mA and 22 mA, a drop in resistance can be observed which can be associated to the phase transformation. A second plateau of almost constant resistance forms over a higher temperature range. At 50 mA the resistance again raises sharply. Here, internal processes take place in the material, possibly crystallization. Consequently, an annealing current of 70 mA is chosen for the given actuator to shape-set HP2.

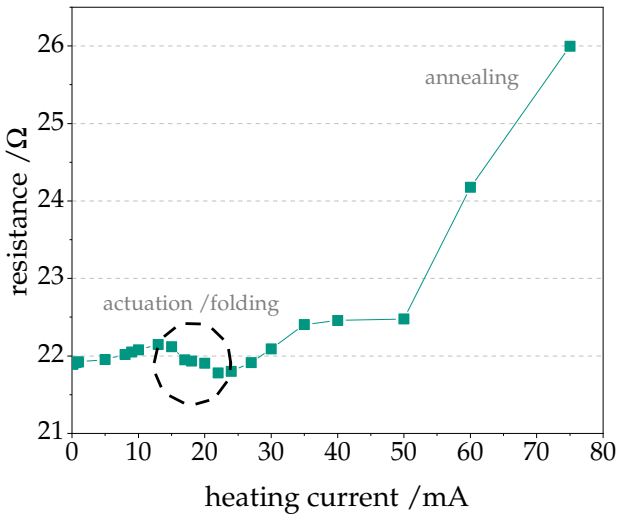

Figure 5.14.: Evolution of the cascaded SMA hinge resistance upon heating.

5.4.1. Uni-directional Folding Performance

For the characterization of the uni-directional folding performance, the single hinge folding actuator (shape-set to +180°) is unfolded by a manipulator tip that is attached to the z-axis linear stage. Unfolding to -180° results in an opening angle of around 80°. The free recovery is observed for two different load cases (see Figure 5.15). *Load 1* corresponds to the weight of a classical PI tile that is attached on one end of the folding actuator. Upon heating, a folding angle of 140° is reached which reduces to 128° upon cooling. In the case of *load 2* the folding angle is already decreased at the starting configuration due to the gravitational load. Upon heating a maximum folding angle of 150° is reached which remains unchanged upon cooling. The gravitational load is sufficient to prevent the unfolding related to the two-way shape memory effect and allows to quantify relevant forces.

5.4.2. Bi-directional Folding Performance

The bi-directional folding actuators are fabricated by positioning two single design actuators next to each other on the same side of the polyimide tiles. The protagonist is annealed at a constraint angle of +180°, the antagonist for the -180° angle.
Figure 5.16 shows the process based on images of the fabricated bi-directional folding actuator. Using the annealing tip, the bi-directional folding actuator is bent towards +180° for annealing of the protagonist (see (Ia) and (Ib)). After annealing and removal of the

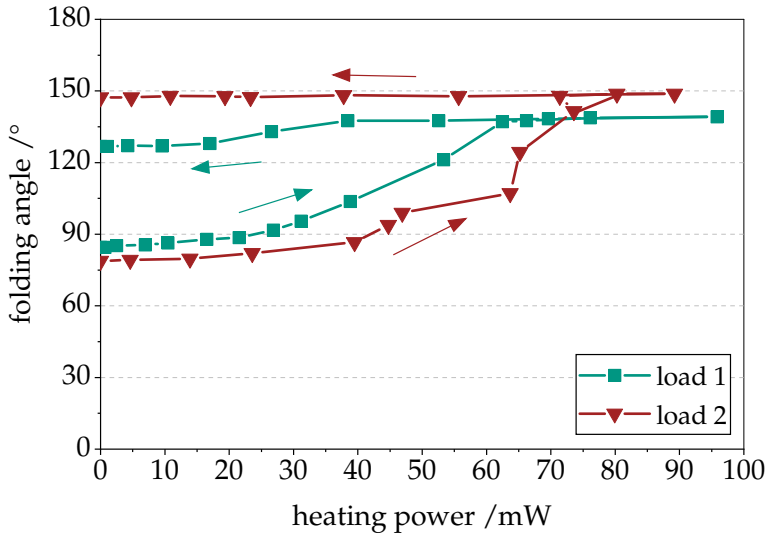

Figure 5.15.: Free recovery of the unfolded single design folding actuator after manual unfolding upon heating. The folding hinge is loaded with two different loads.

pin, the actuator remains in the position shown in (Ic). The subsequent annealing of the antagonist consists of folding the bi-directional actuator towards -180° (see (IIa) and (IIb)) and applying the annealing current. After removal of the pin the bi-directional actuator folds back into the position shown in (IIc). One initialising cycle consists of actuating the protagonist once, and the antagonist once before characterizing the bi-directional folding actuation in a full cycle.

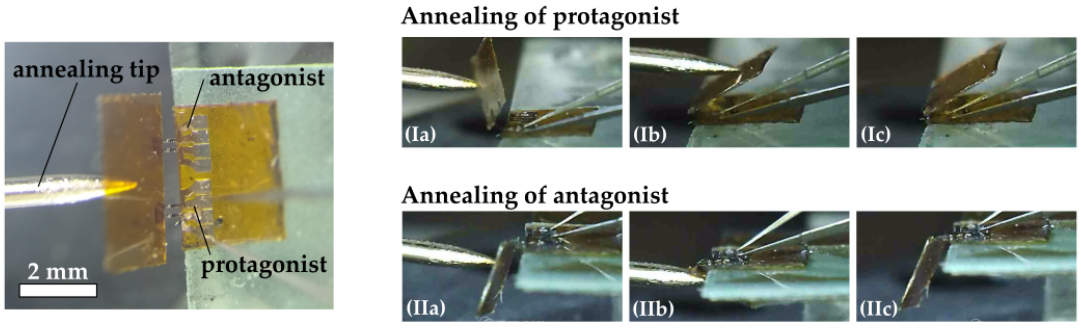

Figure 5.16.: Annealing process of a bi-directional single hinge design actuator: (Ia)-(Ib): folding of the protagonist by annealing tip; (Ic): after annealing of the protagonist; (IIa)-(IIb) folding of the antagonist by annealing tip; (IIc): after annealing of the antagonist.

The bi-directional actuation of single hinge actuators is shown in Figure 5.17. When the protagonist is exclusively heated, the actuator folds to +55°. If the heating current is removed, the folding actuator returns to +15°. When in the next step, the antagonist is exclusively heated, the total folding actuator reaches an angle of -50° and returns to -8° upon cooling. Folding starts at a heating power of around 40 mW and is completed at approximately 100 mW. A total bi-directional folding angle of 105° is achieved.

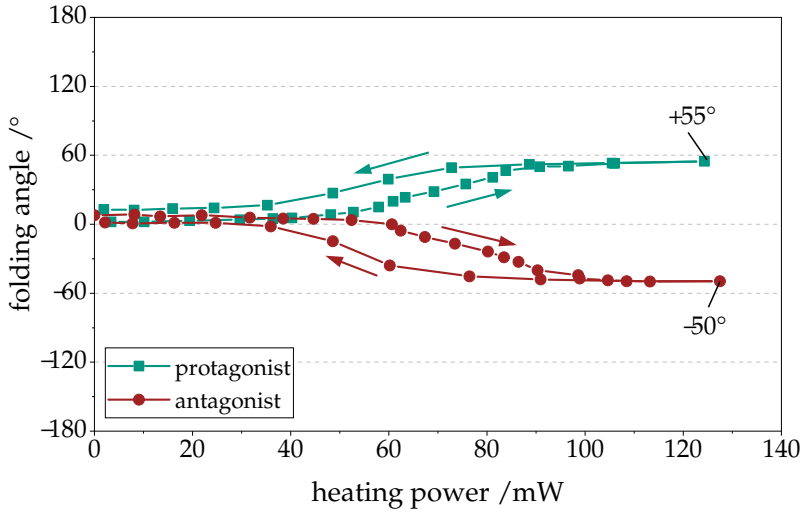

Figure 5.17.: Bi-directional folding performance of single hinge folding actuators based on TiNiCu thin films.

Furthermore, the dynamic behavior of the single design actuator is characterized for its bidirectional folding. Instead of a step-wise increase of the heating current, a current pulse is applied with three different amplitudes. The motion of the folding actuator is captured by a video camera. Figure 5.18 shows the angular response of the actuator for these three cases starting at a folding angle of +14.6°. For the 40 mA pulse, a folding angle of -20.4° is reached within Δt = 3.8 s, thus a total folding motion of 35°. When the heating current returns to 0 mA, the bi-directional folding actuator recovers to +10.2°. For the following 50 mA pulse, a folding angle of -40.5° is reached within Δt = 2.3 s. After switching off, the recovered folding angle is +7.7°. For a 60 mA current pulse, the heating time decreases further to Δt = 430 ms. The folding actuator reaches a folding angle of -44.8° and recovers to +6.6° upon cooling.

At higher amplitudes of the current pulses, the heating time Δt decreases and the cooling time to reach the stable position in cold state increases. Higher currents, thus higher temperatures in the actuator do also affect the surrounding material. While the natural

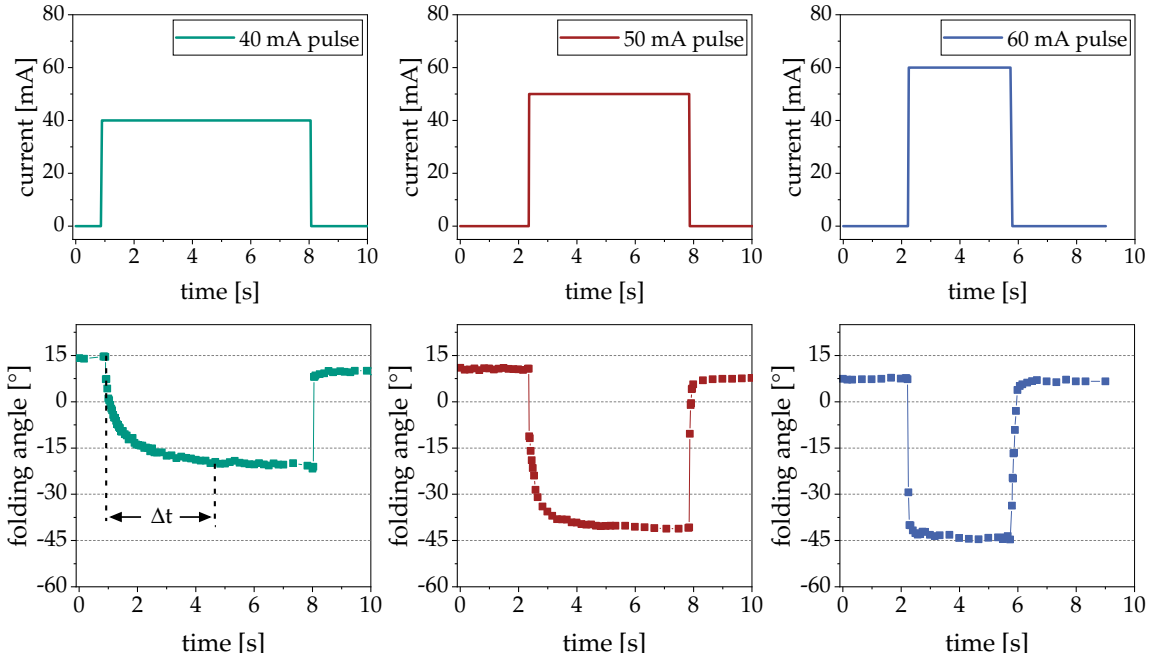

Figure 5.18.: Dynamic bi-directional folding behavior for different current pulses (40 mA, 50 mA and 60 mA).

convection of the thin and small TiNiCu is high, the heat transferred from the polyimide tiles slows down the cooling process.

5.5. Double-stage Folding Actuators Based on TiNiCu Films

Cascaded folding actuators are fabricated according to the derived dimensions in section 5.2. For annealing of the cascaded actuators, first the two freestanding pads are interconnected in configuration 1. The hinge pair 1 is folded into 180° configuration and annealed by a heating current of 210 mA for 10 s. In the next step, the pads in configuration 2 are interconnected. The hinge pair 2 is folded into a 90° configuration and annealed by a heating current of 130 mA for 10 s.

5.5.1. Uni-directional Folding Performance

The hinge pairs of the cascaded actuators are manually unfolded individually and total actuator is heated in configuration 2 for free recovery of the memory shape. As shown in Figure 5.19 (a), the relative folding angle of the two hinge pairs differs after manual unfolding. HP1 (shape-set to +180°) is opened to an angle of +90°, HP2 (shape-set to +90°)

is quasi-plastically deformed to +10°. Upon heating, the individual folding motion of both hinge pairs is tracked, as well as the total folding angle (see Figure 5.20). Due to its smaller width, the folding motion of HP2 starts at a heating power of 20 mW and is fully completed at 70 mW. In contrast, HP1 reaches the phase transformation temperatures only at around 65 mW and completes its folding motion at 110 mW.

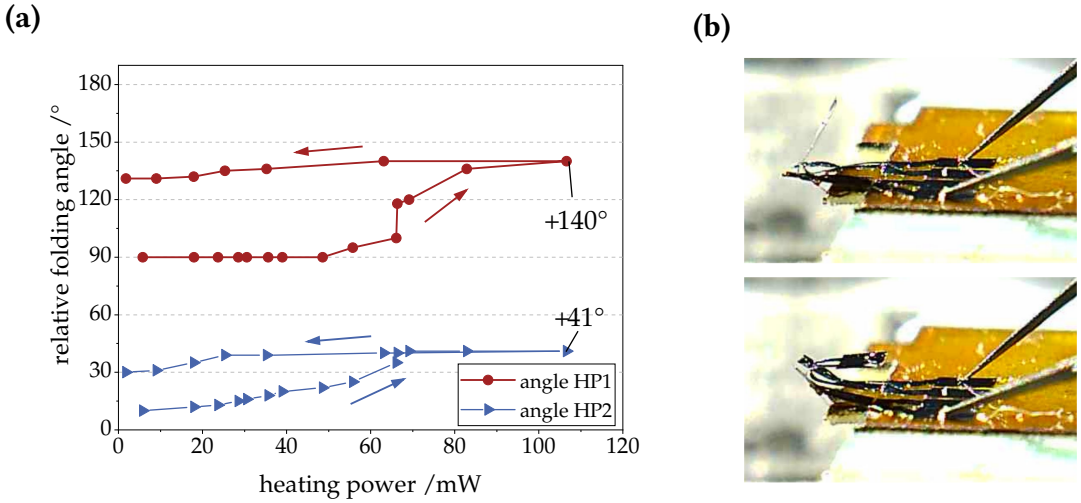

Figure 5.19.: **(a)** Relative folding angle of the individual hinge pairs HP1 and HP2 after manual unfolding and during free recovery upon Joule heating; **(b)** microscope images after manual unfolding (top) and after shape recovery (bottom).

The resulting total folding angle as a function of the heating power derives from the sum of the individual relative angles in 5.19 (a). Two regions can be distinguished in Figure 5.20. A small angular contribution of HP2 and the large folding motion of HP1.
The large difference in angular contribution of the two hinge pairs can be attributed to three phenomena: First, during the manual unfolding of the cascaded actuator by a manipulator tip, the hinge pair HP2 was more easily deformed. Thus, the quasi-plastic deformation in HP1 is larger compared to HP2. Secondly, the shape-set angle of HP1 is 180° whereas, HP2 was only heat-treated for 90°. Lastly, the wider hinge width of HP1 leads to a larger stiffness.

5.5.2. Bi-directional Folding Performance

Similarly to the single hinge folding actuators, two antagonistic cascaded actuators are combined sharing the same tiles. Here, the protagonist is shape-set to +180°/+90° (HP1/HP2) and the antagonist is shape set to -180°/-90°.

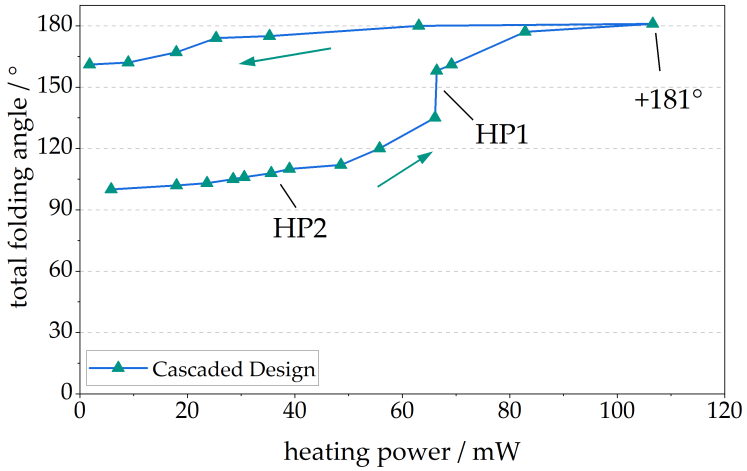

Figure 5.20.: Total free recovery angle of cascaded folding actuator after manual unfolding and upon Joule heating.

Selective heating of the protagonist initiates a folding motion for a heating power of around 40 mW and leads to a folding angle of +107° at a heating power of 70 mW (see Figure 5.21). Upon cooling the equilibrium point of -25° is reached. When the antagonist is exclusively heating in the subsequent step, the folding actuator starts its folding motion at a heating power of around 48 mW and completes its folding motion at an angle of -105° at a heating power of 74 mW. Turning off the heating current results in an equilibrium point of -10°.
The resulting total bi-directional folding angle for the antagonistic cascaded actuators is 212°. The angle difference of the two equilibrium positions in cold state is 15°.

5.6. Discussion

A completely new fabrication route has been developed for the fabrication of miniaturized multi-stage folding actuators including a microstructuring process and heat treatment by Joule heating. For the single design layout (comparable to the double bridge folding actuators in chapter 4) the uni-directional folding angle reaches +150° with an additional load. In bi-directional actuation, folding between -50° and +55° is achieved. Thus, a total folding angle of 105°.
The novel layout of the cascaded folding actuators allows for increasing the uni-directional folding angle to +180° without additional loading. The total bi-directional folding angle is doubled to 212°. Besides the improvement of uni-directional actuation

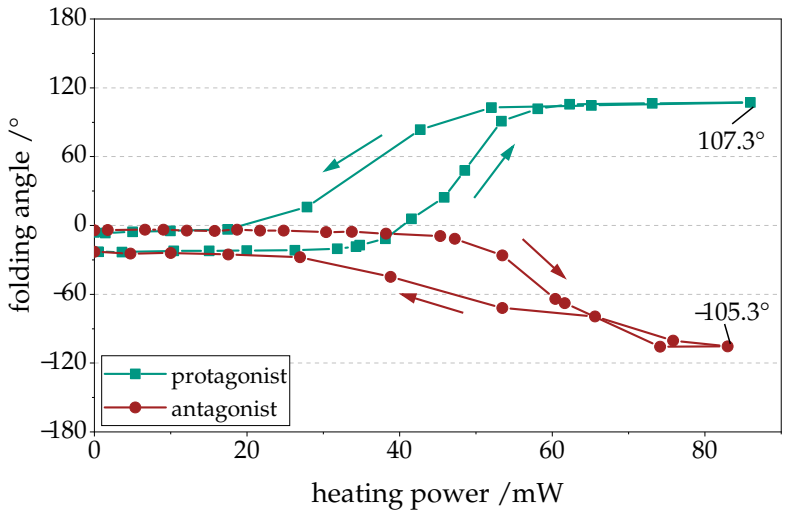

Figure 5.21.: Bi-directional folding actuation of a cascaded design actuator.

to the performance of bi-directional folding, this improvement can be attributed to the additional flexibility of the cascaded design. If one actuator is heated for folding, the other antagonistic hinge can accommodate to the folding motion and prevents additional stress.

Theoretically, the addition of more double hinge pairs in series, is possible with the chosen layout. This could enhance the uni- and bi-directional folding performance even further. But the heat treatment steps would become more difficult. It would be necessary to position additional freestanding tiles that serve as support structures during the shape setting step. Thereby, multi-stage folding can allow to reach bi-directional folding angles in the range of ±180° and beyond.

Further omptimization of the cascaded actuator layout could possibly improve the current actuation range. The easiest adaptation could be to decrease the temperature gradient along the hinge sections (as shown in Figure 5.8) during annealing and actuation. One possibility is the variation of the beam width along the hinge section.

6. Magnetic Latching of Micro Folding Actuators

By introducing a latching mechanism, the bi-directional folding can be upgraded to a bistable system, and the folding range can be extended due to the additional magnetic attraction forces. As described in chapter 2.5, two ferromagnetic elements are combined for the realization of a magnetic latching system, which are brought into proximity by the folding movement and come into contact with sufficient attractive force. For switchable folding via local heating, a sputtered NiMnGa(Cu) thin film with a thickness of 5 µm is used and bonded to the freely movable tile. A permanent magnet is positioned above the substrate of the micro-folding actuator to correspond with the folding movement.

The latching process involves the interaction of different forces and bending moments as illustrated in Figure 6.1. The folding hinges of the actuator are represented as a torsional element (orange dot). If the NiMnGa film is located on the free-moving tile and is moved towards the hard magnet by the folding movement, the bending moment of the heated protagonist ($M_{prot,A}$) reduces until reaching its maximum folding angle $\alpha_{max}=\beta$. Meanwhile, the counteracting bending moment of the cooled antagonist ($M_{ant,M}$) increases for larger folding angles. The attractive magnetic force becomes larger when the separation between the hard magnet and the soft magnetic film decreases upon folding. Its contribution to the overall moment depends on the location of the soft magnetic film on the freestanding tile. The bending moment M_{mag} can be approximated by $F_{mag}\times d$, where d is the distance to folding axis.

Here, two different cases are considered. In case I, the hard magnet is located at a folding angle $\alpha \leq \beta$. When the actuator folds towards its maximum bi-directional folding angle, a minimal attractive force is sufficient to fix the actuator in this position. In case II, the magnet is positioned at a position $\beta + \Delta\beta$, i.e. at a larger angle than the actual bi-directional folding angle generated by actuation. Beyond $|\alpha|=|\beta|$, the bending moment $M_{prot,A}$ is zero

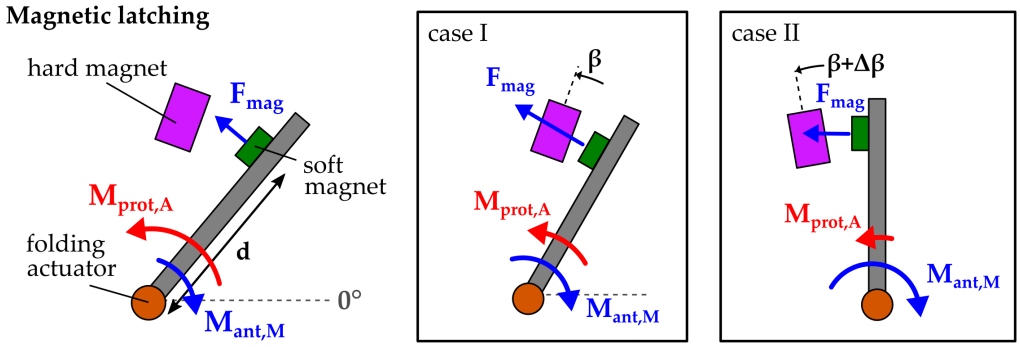

Figure 6.1.: Schematic of forces/ bending moments involved in magnetic latching and two studied cases.

and does no longer contribute to the folding motion. For the actuator to overcome the difference $\Delta\beta$, a sufficiently high magnetic attraction force is required. Therefore, a strong stray field is required for the hard magnet.

A further criterion for latching is whether the two magnetic components get released once the heating current of the protagonist is turned off. The holding force and resulting magnetic bending moment have to be higher than the two counteracting bending moments of the cooled folding hinges ($M_{prot,M}$ and $M_{ant,M}$). Otherwise, unlatching would take place. For controlled unlatching and on demand, two different scenarios are possible as schematically shown in Figure 6.2.

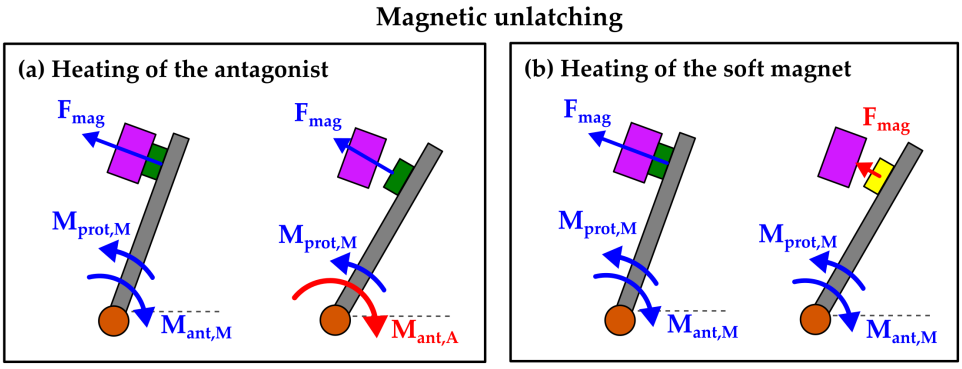

Figure 6.2.: Schematics of controlled unlatching: **(a)** Forced unlatching by heating of the antagonistic folding hinge; **(b)** Unlatching by controlled heating of the soft magnet.

In the first case (Figure 6.2(a)) the two magnetic components are separated from each other by heating the antagonistic folding hinge. The resulting bending moment $M_{ant,A}$ of the active folding hinge has to exceed $F_{mag} \times d + M_{prot,M}$, where $M_{prot,M}$ represents the

bending moment of protagonist in martensite state. In the second case (Figure 6.2(b)), the soft magnet is heated locally to reduce its magnetization. The magnetic attraction force lowers and once the resulting bending moment drops below the sum of the bending moments of both folding hinges, the two ferromagnets are separated. The combination of both unlatching mechanisms is possible.
The folding actuator operates within a three-dimensional working space and is highly flexible due to its design. However, due to additional loads such as neighboring tiles, or dynamic folding with overshoots caused by the system's inertia, the exact angular trajectory may not be clearly defined. Despite these uncertainties, it is important to ensure that the latching of the actuator latches is guaranteed. Considering the fixed position of the permanent magnet, the effect of misplacement of the NiMnGa layer, both in terms of fold angle and lateral displacement needs to be investigated.

In this chapter, the characterization of the NiMnGa(Cu) films is discussed and the magnetic attraction forces generated in combination with a permanent magnet are evaluated with regard to alignment and temperature dependence. Finally, the magnetic latching and unlatching of the folding actuator is characterized. A freestanding NiMnGaCu was used for the demonstrator. However, since most investigations were carried out using NiMnGa films on substrates, the generic term NiMnGa is used here for the sake of simplicity.

6.1. Material Characterization of NiMnGa Thin Films

NiMnGa thin films are fabricated by project partners. Different alloy compositions are investigated, including the addition of Cu. Using an alloy target ($Ni_{48}Mn_{22}Ga_{30}$) the NiMnGa(Cu) thin films are sputtered by DC magnetron sputtering onto a 20 nm Cr buffer layer as described in [91][1]. Subsequent annealing at 400 °C is performed in an ultra-high vacuum chamber. The temperature-dependent magnetization measurements are measured by a vibrating-sample magnetometer (VSM). The measured magnetic moment is divided by the respective sample mass to represent the specific magnetization M in Am^2kg^{-1} as a function of the temperature or the applied magnetic field [60].
Magnetization measurements of a freestanding NiMnGaCu film in dependence of temperature T for two different external magnetic fields H are depicted in Figure 6.3 (a). Contrary to the magnetization plot in Figure 2.13 (b), it does not show any first-order transformation between martensite and austenite state. For a field of $\mu_0 H = 0.1$ T, it reaches a magnetization of 37.7 Am^2/kg at room temperature (23 °C) and at $\mu_0 H = 0.3$ T

[1] Freestanding films and characterization data are provided by L. Fink from Leibniz IFW Dresden.

its specific magnetization is 46 Am²/kg. If the material is heated from room temperature, it directly drops in magnetization and enters the second-order transformation from ferromagnetic to paramagnetic state. The Curie temperature T_c is located at 348 K. The drop in magnetization upon heating is in the order of $\Delta M/\Delta T = 0.98\, Am^2 kg^{-1} K^{-1}$. The magnetization hysteresis curve of a $Ni_{48}Mn_{31}Ga_{21}$ film deposited onto a Si substrate is depicted in Figure 6.3 (b). The material shows a maximum magnetisation of 60 Am²/kg and a coercivity H_c of 12.27 mT. The remanent magnetization after removal of the external field is 6.71 Am²/kg.

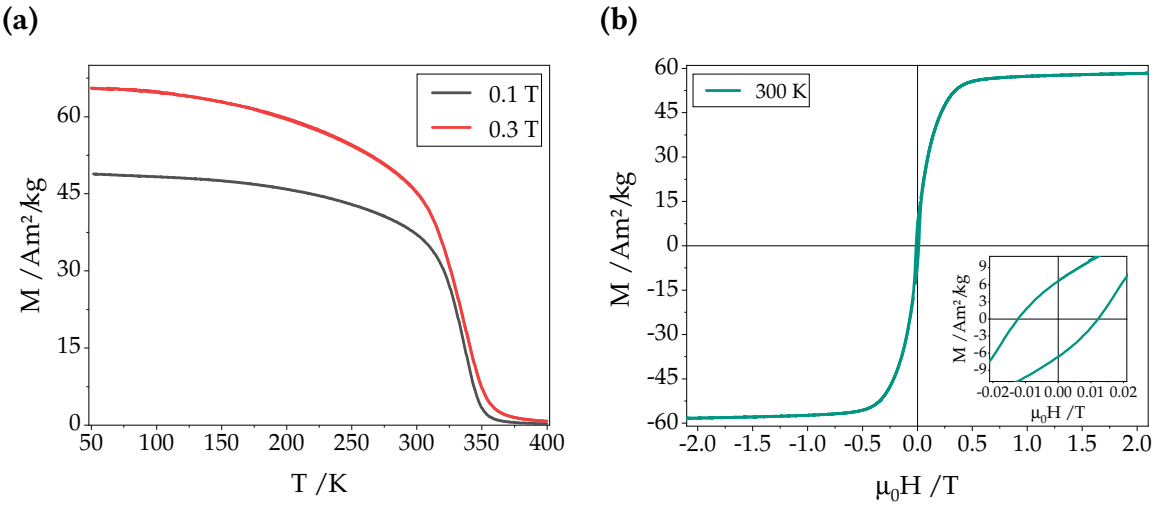

Figure 6.3.: (a) Magnetization of sputter-deposited NiMnGaCu thin film as a function of temperature for two different fields $\mu_0 H$. **(b)** Magnetization of $Ni_{48}Mn_{31}Ga_{21}$ as a function of external field H and hysteresis (inset) at an ambient temperature of 300 K.

No MH-curve is available for the freestanding NiMnGaCu thin films. It was shown that the Curie transition relevant for this work, does not vary with the substrate the thin film is deposited on. Only the first-order martensitic transformation is affected [60]. The MH-curve in Figure 6.3 (b) provides comparable magnetization values for NiMnGaCu films and is included in magnetic simulations. The Curie temperature (T_c = 348 K) provides information on the heating required for unlatching of the two magnets.

6.2. Magnetic Field Simulations

A computational model is built within COMSOL Multiphysics for studying the combination of hard and soft magnets in varying relative orientations and the resulting magnetic forces. The built-in physics module named *Magnetic Fields, No Currents (mfnc)* was used in

the simulations. As schematically shown in Figure 5.5, the geometry is divided into three domains: the NdFeB magnet (green), the NiMnGa film and the surrounding air. When using the *mfnc* module, the following Maxwell equations are solved for all domains using the Finite Element Method (FEM):

$$\nabla(\mu_0\mu_r \boldsymbol{H}) = 0 \tag{6.1}$$

$$\boldsymbol{H} = -\nabla V_m + \boldsymbol{H}_b, \tag{6.2}$$

where $\boldsymbol{H}$ is the magnetic H-field, V_m is the scalar potential, μ_r is the relative permeability of the material, and $\boldsymbol{H}_b$ represents the boundary conditions.
The magnetic flux $\boldsymbol{B}$ in air is described by the constitutive equation $\boldsymbol{B} = \mu_0\mu_r\boldsymbol{H}$, where $\mu_r = 1$ (as in vacuum). The domain of the cylindrical permanent magnet is described by $\boldsymbol{B} = \mu_0\mu_r\boldsymbol{H} + \boldsymbol{B}_r$, where $\boldsymbol{Br}$ corresponds to its remanent flux, which is oriented in z-direction. Finally, the domain of the soft NiMnGa film follows the relationship $\boldsymbol{B} = \mu_0(\boldsymbol{H} + \boldsymbol{M})$. Its magnetization is determined using the specific magnetization curve (refer to Figure 6.3 (b)) and the density of NiMnGa.

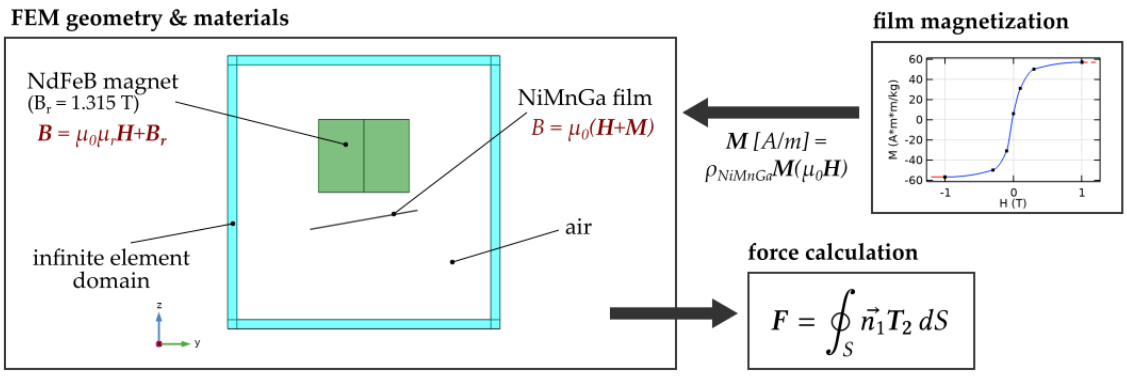

Figure 6.4.: Setup of the computational FEM model for magnetic force estimation.

The air domain is enclosed within an infinite element domain. The magnetic force (F) is calculated by integrating the Maxwell surface stress tensor ($\vec{n_1}\boldsymbol{T_2}$) over the NiMnGa film exterior boundaries:

$$\vec{n_1}\boldsymbol{T_2} = -\frac{1}{2}\vec{n_1}(\boldsymbol{H}\cdot\boldsymbol{B}) + (\vec{n_1}\cdot\boldsymbol{H})\boldsymbol{B}^T, \tag{6.3}$$

where $\vec{n}_1$ corresponds to the normal vector of the entity's surface.
The force calculation by direct evaluation of the fields requires a finer mesh and smooth edges in order to avoid singularities at the edges. This method allows for evaluating distributed forces and local magnetomechanical coupling.

6.3. Magnetic Forces between Soft and Hard Magnets

The permanent magnet used is a cylindrical NdFeB bar magnet (HKCM) with a diameter of 1 mm and a length of 0.8 mm. It is covered with a Ni coating and its operation temperature is limited to 100 °C. Based on analytical calculations, the manufacturer specifies a specific magnetic flux density of 1.28 T on the inside and 0.48 T on the surface of the magnet. Its relative permability is $\mu_r = 1.05$.

To characterize the magnetic attraction force, the hard magnet is glued on a holder that is mounted to a 5 N load cell. The load cell can be moved in the z-direction (see schematic in Figure 6.5). A square NiMnGaCu thin film (edge length of 1.2 mm and thickness of 5 µm) is glued onto a substrate. This substrate is fixed to a heatable platform and can be moved in the x-y direction.

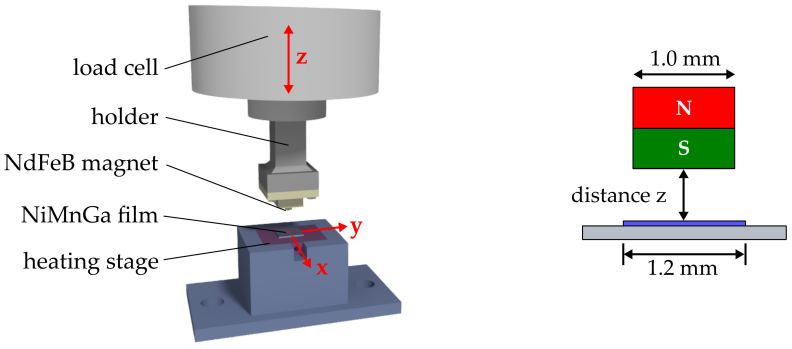

Figure 6.5.: Setup for magnetic force measurements and dimensions of hard NdFeB magnet and soft NiMnGaCu film.

An additional tilting stage allows for adjusting the relative angle γ between the hard NdFeB magnet and the soft NiMnGaCu film. While the distance z is defined between the center of the NiMnGaCu film to the surface of the bar magnet, the measurement in a tilted configuration is limited to the minimum distance z_{min} (see Figure 6.6 (a)).

In repeated measurements, deviations of the maximum attraction force of up to 0.02 mN are observed. The individual force measurements exhibit a noise level of 0.02 mN. Since the noise exceeds the averaged error, the error bars in the graphs indicate the load cell's measurement error.

Figure 6.6 (b) shows a selection of force-displacement characteristics for different relative angles. These curves are smoothed by removing the noise. For $\gamma = 0°$ the maximum magnetic attraction force F_{mag} reaches 2.55 mN. The curves are also plotted for the distance z in the appendix A.6.

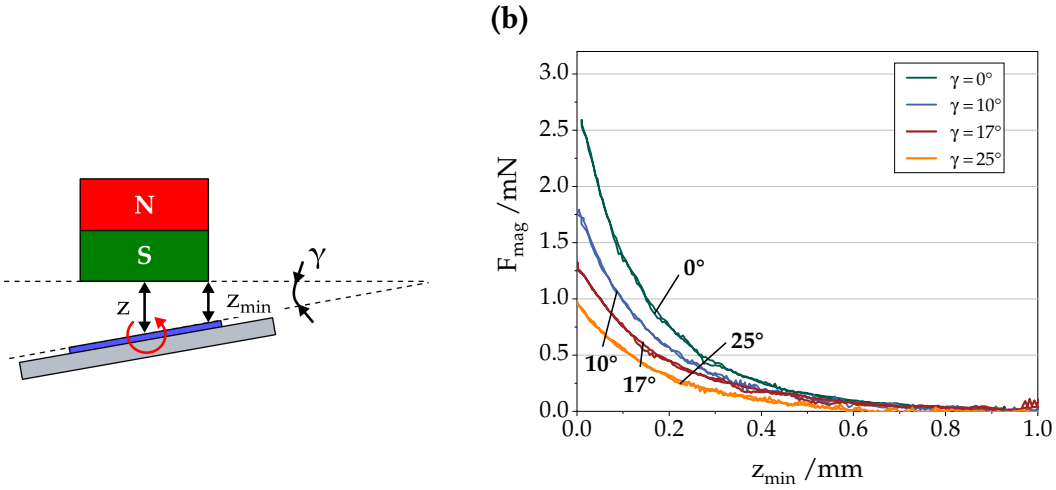

Figure 6.6.: Effect of angular misplacement of soft magnet relative to the permanent magnet: **(a)** setup and parameter definition **(b)** experimental magnetic force measurement curves for four different tilt angles γ (0°,10°,17°,25°).

If the force curve is compared, the characteristics shift to the right with increasing tilt angle in the micrometer range. For a given minimum distance between hard magnet and soft magnetic film, the tilt angle can lead to minimally higher forces due to the high gradient of magnetic flux density at the outer edge of the bar magnet. However, the decisive factor for the magnetic attraction force generated, is the distance z, which is severely restricted by the tilt.

The experimentally derived maximum force for different tilt angles are plotted in Figure 6.7 (b). Additionally, the force drop at z_{min} = 100 µm and z_{min} = 200 µm is plotted. At a distance of 100 µm, the magnetic force is already 50% of the force of attraction in direct contact. The further away the film is from the magnet, the smaller the effect of the tilt angle. The absolute difference in force decreases, but the percentage reduction

in force remains almost the same. While the maximum force decreases by 44% at a tilt angle of 16° compared to 0°, the force also decreases by 40% (from 0.75 mN to 0.45 mN) at a distance of 200 µm. A FEM simulation confirms the trend (see Figure 6.7 (b)) but generates higher magnetic force values as the simulation assumes defectless surfaces of the hard magnet, homogeneous properties of the NiMnGa film and assuming analytically derived BH-curves.

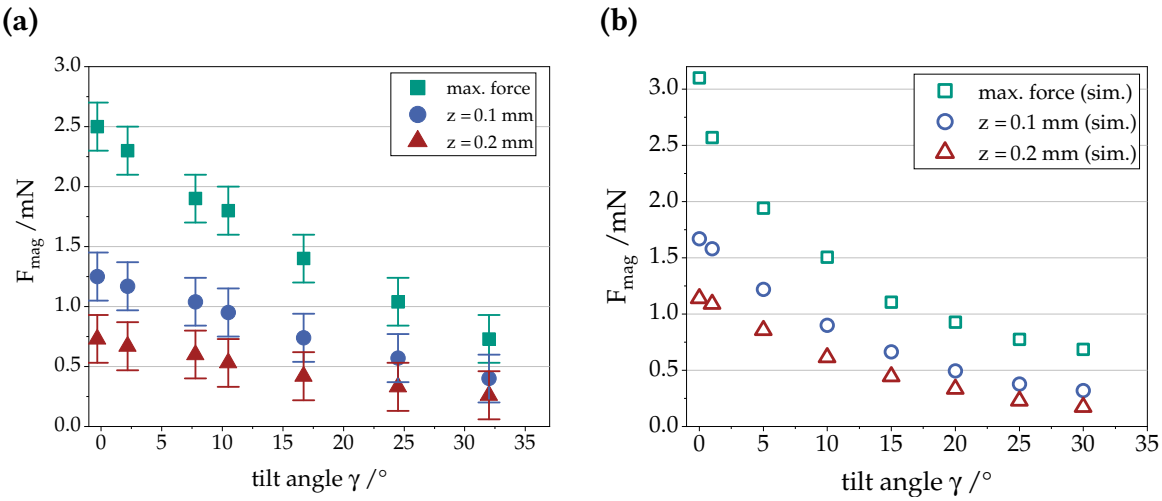

Figure 6.7.: Effect of angular misplacement of soft magnet relative to the permanent magnet: **(a)** experimental values **(b)** simulation.

Another possibility of misplacement is the lateral displacement of the NiMnGaCu thin film relative to the NdFeB magnet. As shown in Figure 6.8 (a), the lateral displacement is represented by the parameter Δy. Here, too, the influence on the magnetic attraction should be estimated experimentally and using FEM simulations. In Figure 6.8 (b), the experimentally determined maximum force is plotted via the lateral displacement Δy. The force in the z-direction as well as the in-plane forces in x- and y-direction can be read out via the FEM simulation and are entered as unfilled data points in the diagram.

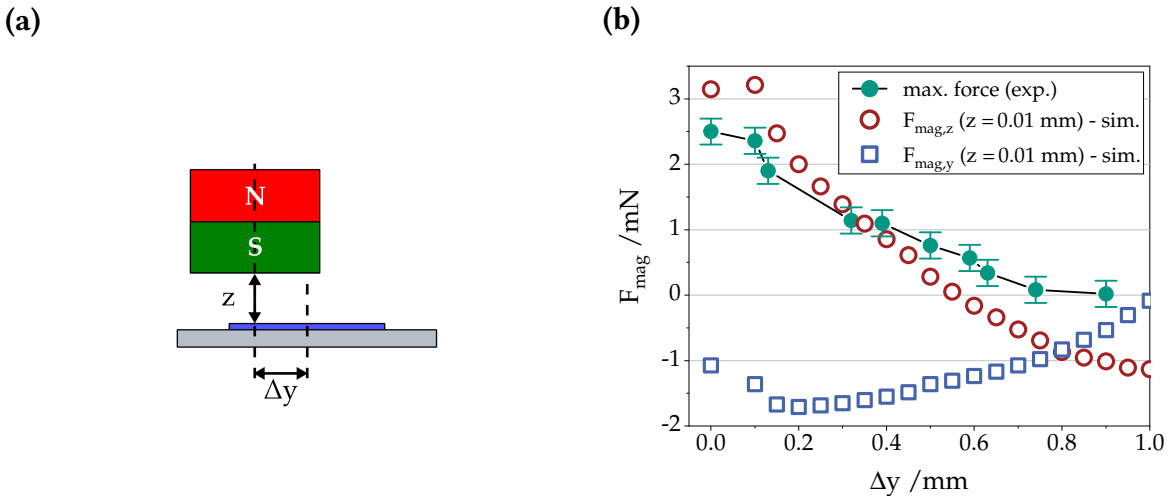

Figure 6.8.: Effect of lateral misplacement Δy of soft magnet relative to the permanent magnet: **(a)** experimental setup, **(b)** comparison of maximum attraction force in experiment and simulation (at distance z = 0.01 mm).

As the thin film is 200 µm larger than the 1 mm wide hard magnet, only a displacement beyond 100 µm leads to a reduction in force. From a lateral displacement of 550 µm, the force in the z-direction changes its sign and acts as a repulsive force. The magnetic force in direction of the lateral displacement F_y is negative and changes its sign from Δy = 1 mm, when the film is no longer located underneath the permanent magnet. The force measurements shows a similar decrease in maximum attraction force. Here, only the z-direction is recorded. From Δy = 0.75 mm, the forces are almost zero.
If one would consider the non-magnetostatic case, a small lateral displacement can be compensated by the flexibility of the actuator. The in-plane forces (in y-direction) can drag the NiMnGaCu film in a more favorable position and allow for latching in z-direction.

Finally, the thermomagnetic properties of the combination of NdFeB and NiMnGaCu thin film are assessed by positioning the thin film onto a heating stage and recording magnetic force vs displacement curves for different temperatures. In an initial step the surface temperature measurement is calibrated by covering the thin film with a carbon spray and placing it onto a hot plate. Thereby, the coefficient of emissivity (0.8) for IR measurements is derived. The temperature evolution on the movable heating stage is then obtained before the force measurements.
Figure 6.9 shows the maximum forces for different temperatures of the NiMnGaCu thin film. Upon heating the force values decrease and a large drop is observed at T = 43 °C. Above 80 °C, the force readings become very small, and the material can be considered to be paramagnetic.

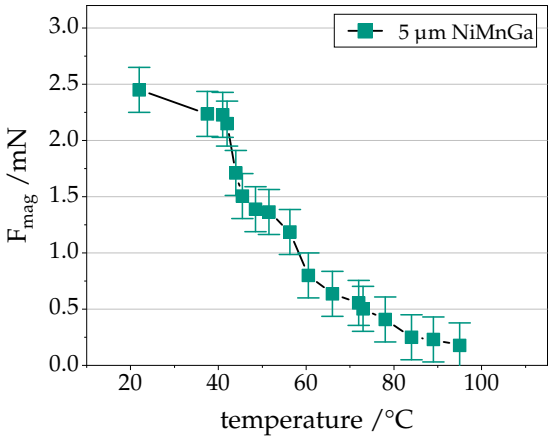

Figure 6.9.: Decrease of the magnetic attraction force upon heating of the NiMnGaCu film.

These measurements compare well with the magnetization measurement as a function of temperature obtained by VSM in Figure 6.3 (a). The Curie temperature of 74 °C can be confirmed by the force measurements.
The evaluation of magnetic force characteristics depending of various parameters (angular and lateral misplacement, temperature), allows for estimating the forces and folding moments acting during the folding actuation and the requirements for latching.

6.4. Latching and Unlatching of Bi-directional Folding Actuators

The freestanding NiMnGaCu thin film is glued in the center of the freely movable tile in between the two opposing actuators. The NdFeB magnet is positioned with a movable holder above the fixed tile and can be adjusted in its position.

Two different latching and unlatching scenarios are studied in the following. In one case, the latching is performed by actuating the protagonist until reaching a folding angle that allows for latching between the soft and the hard magnet. Unlatching is performed by actuating the antagonist and thereby generating enough bending moment to separate the two magnets according to Figure 6.2 (a).
In the second setup, the latching is again performed by actuating the protagonist for latching. The unlatching is performed by step-wise heating of the magnet and thereby

reducing the magnetization of the NiMnGaCu film. This unlatching method is introduced in Figure 6.2 (b).

6.4.1. Unlatching by Antagonistic Actuation

Two different magnet positions are studied (refer to Figure 6.10). First, the hard magnet is positioned at +102° (a). The folding actuator is cooled and rests in its equilibrium position at -10° (1). Upon step-wise Joule heating of the protagonist, the bi-directional folding actuator starts its folding motion at 25 mA and becomes attracted to the magnet at 36 mA (2) before reaching its maximum folding angle of +107°. The folding actuator remains at the magnet position of +102° upon further heating to point (3). The reduction of the heating current down to 0 mA, does not change the position of the folding actuator (4). The latching force between hard and soft magnet is sufficient to overcome the counteracting force of the antagonist and prevents the recovery to the equilibrium angle (-10°).

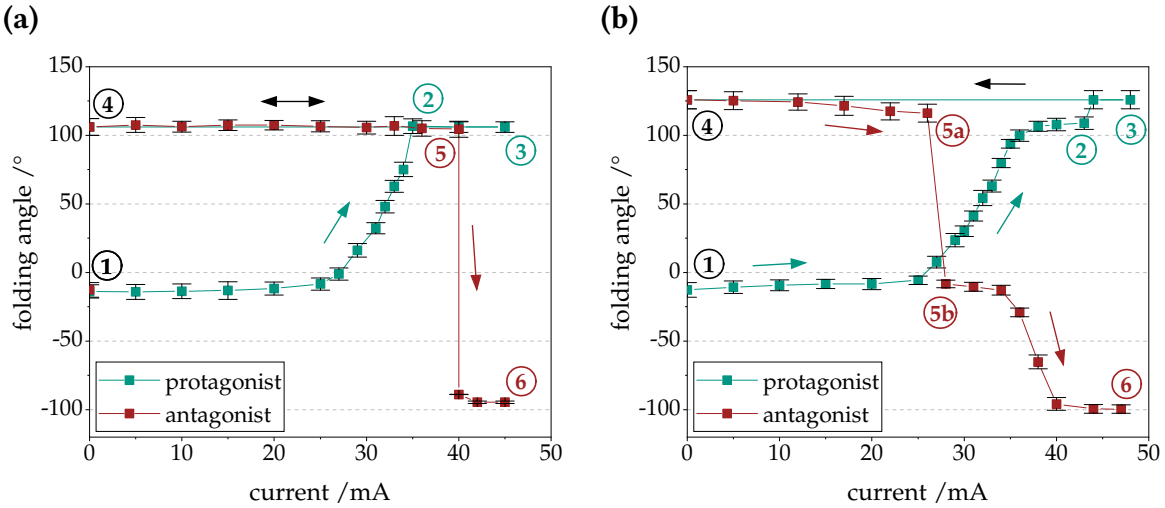

Figure 6.10.: Latching and unlatching motion for different positions of the soft magnetic dot. **(a)** Magnet positioned at 102°. **(b)** Magnet positioned at 125°.

In a second step, the antagonist is heated step-wise by increasing its supply current. At a heating current of 40 mA, unlatching occurs (5) and the bi-directional folding actuator switches to its opposite side reaching an folding angle of -85°. The corresponding heating power at this point amounts to 84 mW. At this heating power the antagonist has almost completely undergone its phase transformation to austenite state and provides the highest folding moment for unlatching. This actuation moment is therefore required to overcome the magnetic attraction force between the two magnets. Upon further heating

to 45 mA, the actuator reaches a maximum of -99° (6).

In Figure 6.10 (b), the magnet is positioned at +125°. Starting from the cooled equilibrium point (1), the protagonist is heated and reaches its maximum folding angle of +107° (see Figure 6.11 (a)). At this point (2), the soft magnetic film is approximately 1 mm away from the hard magnet and is at a relative angle of 5°. The magnetic attraction force is below 0.05 mN at this distance. Latching takes place at a heating current of 43 mA (3), resulting in an increase of the total folding angle by $\delta\alpha = 18$ (see Figure 6.11 (b)). Cooling of the protagonist does not affect the position of the folding actuator (4). When in the second step, the antagonist is Joule heated, the unlatching occurs earlier compared to Figure 6.10 (a). Here, the folding actuator starts to move at a heating current of 23 mA (5a) and the two magnets get completely separated at 27 mA (5b). The heating power amounts to 55 mW. The antagonist is not fully transformed at this point. Therefore, the switching results in a folding angle of −12°. Further heating of the antagonist completes its phase transformation and moves the folding actuator to its final equilibrium point of -100° (6).

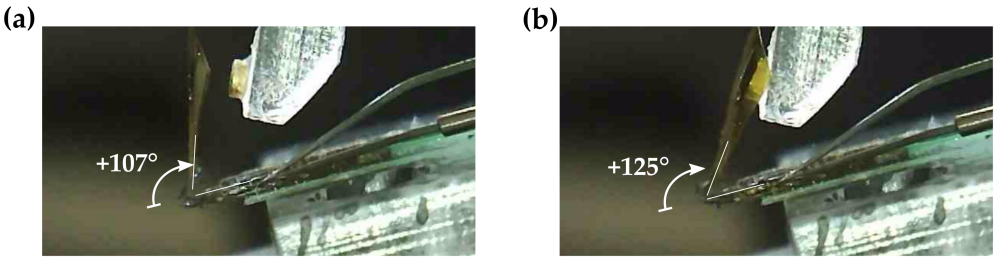

Figure 6.11.: Magnetic latching sequence of a bi-directional actuator: **(a)** maximum folding angle upon heating before latching (I = 42 mA), **(b)** folding actuator position after latching (I = 43 mA).

Placing the magnet at an even higher angle than +125° no longer enables latching in the case of a 5 µm NiMnGaCu film. For latching, the attractive force would have to overcome an angle of more than 20° and a distance of more than 1.1 mm. According to the experimental characterizations from Figure 6.6, the magnetic attraction force is less than 0.02 mN under these conditions and is therefore not sufficient for increased folding of the actuator.

6.4.2. Unlatching by Heating of the Magnet

In the second setup, the unlatching by local heating of the switchable soft magnet is studied. As shown in the microscope image in Figure 6.12 (a), the permanent magnet is glued onto a Cu stripe holder. On its backside a 10 Ω heating resistor is glued that is electrically connected by solder joints. This setup allows for resistive heating of the NdFeB magnet and the reduction of magnetization of the soft magnetic film when in contact.
Figure 6.12 (b) shows the change in surface temperature of the permanent magnet when the voltage on the heating resistor is increased. It follows a linear trend and allows for evaluating the temperature of the magnet. When the softmagnetic film is in contact with the NdFeB magnet, the heat transfer and contact resistance have to be considered to estimate the temperature of the thin film.

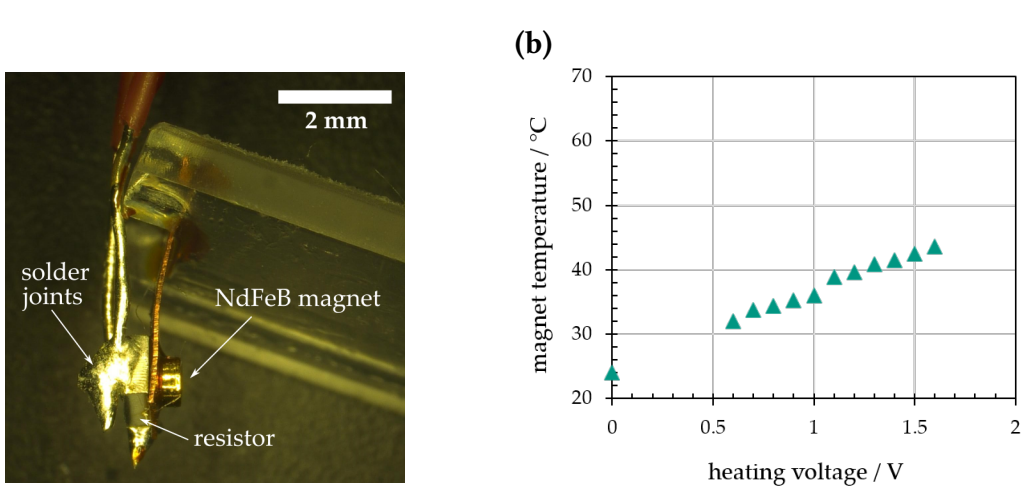

Figure 6.12.: (a) Setup for local heating of the permanent magnet. **(b)** Surface temperature of the hard magnet upon resistive heating.

During bi-directional folding, the permanent magnet is kept at a constant position (α = +120°), only the temperature of the magnet is changed by adjusting the voltage. The fold angle caused by the thermal actuation is tracked over time so that the latching and unlatching can be identified. A microscope camera is used for tracking with a recording frame rate of 60 fps.

Figure 6.13 shows the case of an unheated magnet during latching. The heating current of the protagonist is switched to 40 mA, causing a folding movement to +105°. The latching to +120° after a heating time of 5 s can be recognized by the abrupt jump in the fold-

ing angle. Even after switching off the heating current, the freely movable tile remains attached to the permanent magnet. The heating voltage of the magnet is now incrementally increased in order to reduce the magnetic attraction force. At a voltage of 1.5 V, the folding actuator jumps back to its starting angle of -10°. According to Figure 6.12 (b), this corresponds to a magnet temperature of 42 °C and a reduction in force from 2.5 mN to 1.7 mN (compare Figure 6.9).

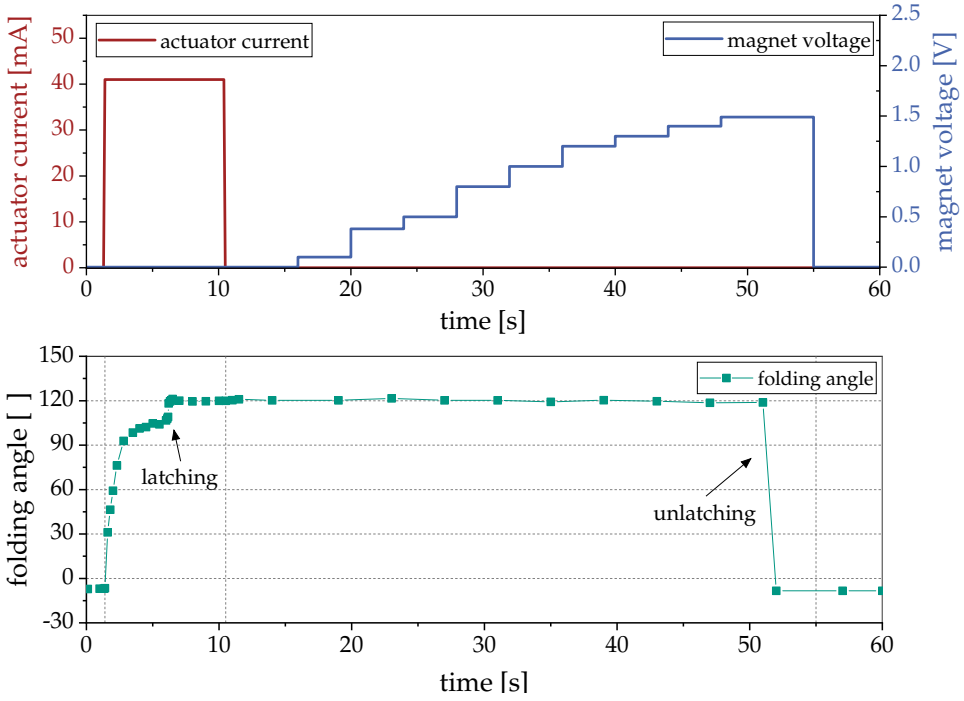

Figure 6.13.: Latching and unlatching of the bi-directional folding actuator.

The magnet is now heated during the folding movement of the actuator and the latching process. Different base voltages are selected for this (1.2 V, 1.4 V and 1.5 V). Figure 6.14 shows the folding angle curve for a base voltage of 1.4 V. The protagonist is also heated with different current pulses. The first current pulse with a level of 35 mA achieves a maximum folding angle of +75°. For a current pulse of 39 mA, the actuator already folds up to +100°. A current level of 40 mA is required again to achieve a folding angle above +105°. Only here is the actuator close enough to the permanent magnet and the latching of the two magnets is achieved.

Here too, the folding actuator remains in its position after the heating current for the protagonist is switched off. The heating voltage of the solenoid is now increased continuously at a rate of 0.1 V/s, starting from the base voltage of 1.4 V. When 1.53 V is reached, the folding actuator snaps back to an angle of +15°. Due to the long thermal

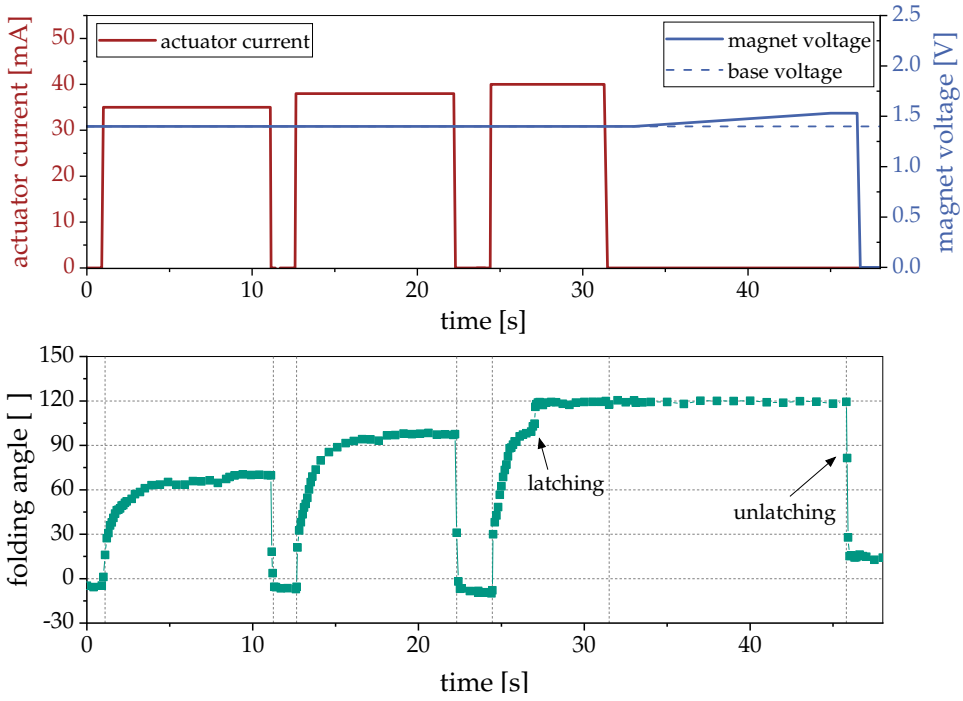

Figure 6.14.: Latching and unlatching of the bi-directional folding actuator. The magnet is heated with a voltage of 1.4 V during latching.

load, it is possible that the entire folding actuator has heated up. To reach the output angle of -10°, the entire substrate and the environment must therefore cool down again. Similar behavior can be observed for a lower base current of 1.2 V. This measurement can be found in the appendix A.7 for the sake of completeness. Unlatching also occurs at a voltage of 1.5 V. In addition, the camera captures the swing-in of the folding actuator. During unlatching, the folding actuator overshoots up to 5° before leveling off at a folding angle of 15°.

The last case is shown in Figure 6.15. Here, the magnet is heated with the base voltage of 1.5 V. Here too, different current pulses are initially used for latching. If the protagonist is supplied with 30 mA, it achieves a folding angle of +32°. For a heating current of 35 mA, an angle of +70° is reached and at 40 mA, the actuator exceeds the +105° before the final latching at +120°. After switching off the heating current of the protagonist, the folding actuator returns directly to the unfolded position (α = -10°). Unlatching takes place immediately after the heating current is switched off. This confirms the previous experiments in which unlatching also occurs at a voltage of 1.5 V.

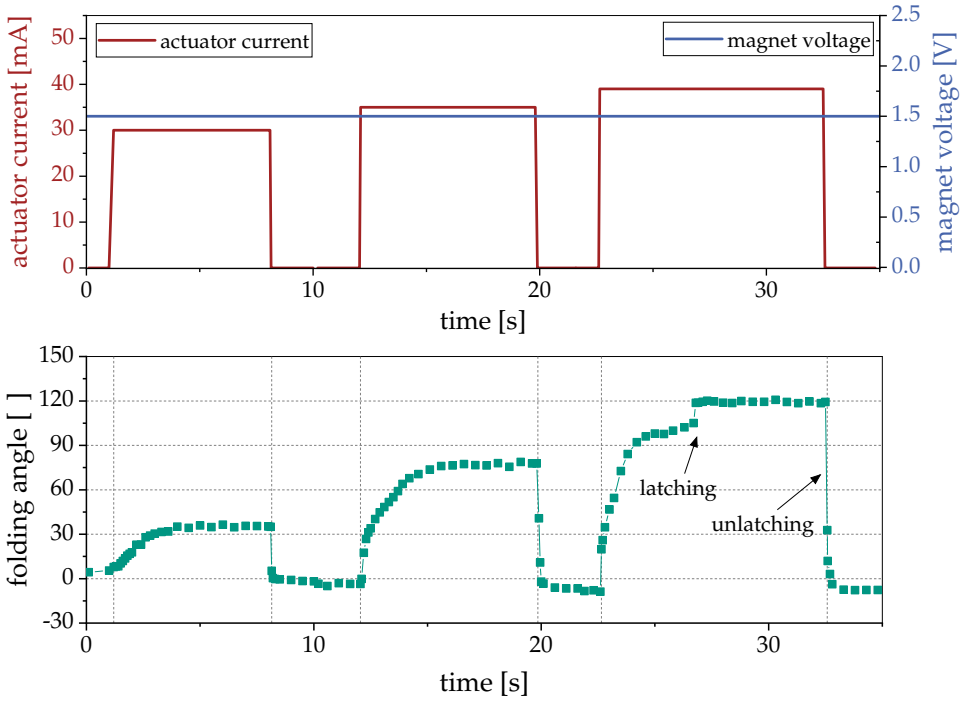

Figure 6.15.: Latching and unlatching of the bi-directional folding actuator. The magnet is heated with a voltage of 1.5 V during latching.

At a voltage of 1.5 V, the surface temperature of the magnet is approximately 42 °C. The corresponding heating power amounts to 210 mW. The holding force is around 1.7 mN and the generated bending moment by magnetic attraction can be approximated to M_{mag} = 1.7 mN × 3 mm = 5.1 mNmm. In this range, M_{mag} is sufficient for latching, meaning that it can enable further folding of the bi-directional actuator and overcome the bending moment of the antagonist $M_{ant,M}$. When the heating current of the protagonist is turned off, its bending moment decreases to $M_{prot,M}$. This drop is sufficient to generate a total negative bending moment and separate the two magnetic components.

In general, both concepts for latching and unlatching have been demonstrated. Unlatching by antagonistic actuation requires a minimum heating power of around 55 mW, whereas the magnet has to be heated with a heating power of 210 mW for unlatching. The thermal losses due to the resistive heating of the permanent magnet via a resistor and additional heat transfer to the film has to be taken into account. Direct heating of the soft magnetic film would reduce the heating power.

7. Conclusions

This work presents the development, fabrication and characterization of various Origami-inspired SMA-based folding actuators at the miniature scale. First, macroscopic mm-sized single hinge folding actuators are developed and their folding performance is investigated. The goal to further miniaturize the folding actuators by a factor of 10 is achieved by introducing a new fabrication process. Second, to increase the folding ranges of the miniaturized actuators, a novel layout consisting of cascaded hinge folding actuators is developed. Finally, the concept of magnetic latching is introduced and explored. The key findings are summarized in this section, and the future scope of this work is outlined.

Macroscopic single hinge folding actuators

Macroscopic folding actuators are developed based on the one-way shape memory effect of TiNi double-bridge structures. 20 µm foils are laser-cut, heat treated for a +180° fold, and glued in between two triangular polyimide tiles, forming the basic unit of an Origami-inspired layout. The folding actuators are manually unfolded, and Joule-heated for shape recovery. Unidirectional folding is achieved up to +150° without any supporting loads. The measurement of the hinge temperature by IR thermography upon heating, confirms the temperature range of phase transformation obtained by DSC measurements. When the actuator is blocked in the 0° configuration, a maximum bending moment of 0.11 Nmm is reached upon heating. The opposing bending moment that is generated upon unfolding in cold state is only 0.03 Nmm. An actuation path diagram is derived from these two types of experiments. It predicts a bi-directional folding range of ±100° for two unidirectional actuators that are combined in an antagonistic setup by pairing the tiles. In experiment, resetting to planar state and bi-directional folding is achieved, but the folding range is limited to ±40°. Thermal and mechanical coupling effects that are neglected in the simple actuation path diagram reduce the actual folding performance. The mm-sized macroscopic folding actuators enable both force and temperature measurements for understanding the underlying mechanisms in uni- and bi-directional folding. However, the heat-treatment in the vacuum oven and the manual assembly steps limit the further downscaling. Additionally, the material shows cyclic fatigue.

Miniaturized folding actuators

A new fabrication process is developed that allows for miniaturization towards microscale folding actuators. It involves photomask structuring by Direct Laser Writing, SMA microstructuring by wet etching and electrical contacting by silver glue. The heat treatment for shape setting to +180° is performed by Joule heating in air. Thus, re-programming of the memory shape is shown. Smallest folding actuators with bridge dimensions of 250 µm × 30 µm × 8 µm are fabricated. The thickness reduction of the 20 µm TiNi foils is achieved by controlled wet-etching. However, non-uniform thinning, surface defects and increased roughness are observed on the initially cold-rolled foil. These can lead to local stress, affect the formation of martensite variants and ultimately reduce the folding performance. A uni-directional folding angle of +145° is reached.
Replacing the cold-rolled foil material by freestanding 6 µm sputtered TiNiCu films improves various steps throughout the microfabrication and results in a higher yield of usable structures. However, the uni- and bi-directional folding range is not improved.
For the miniaturized folding actuators, a new annealing and test setup is developed to allow for convenient shape setting by Joule heating and tracking of the folding angle. However, the reduced dimensions and associated lower bending moments present challenges for accurate force measurement. Applying additional loads onto the freestanding tiles and introducing magnetic latching components with known force characteristics, allow for a rough estimation of the involved bending forces/moments.

Cascaded hinge folding actuators

A novel layout of a cascaded hinge folding actuator is introduced to increase the angular folding range by multi-stage folding. It consists of two hinge pairs arranged in series and aligned as closely as possible. The concept is studied in detail by a thermo-electrical finite element simulation which shows good fit with test structures. A challenging two-step annealing process is required which involves interconnecting different pad structures. The uni-directional angle reaches the aimed +180° and the bi-directional folding range extends to ±105°, which corresponds to an increase by more than a factor of 2 compared to the single hinge folding actuators. The additional in-plane flexibility of the cascaded design benefits the bi-directional folding motion because it can accommodate bending related deformations. Further extension to three hinge pairs is theoretically possible but makes the heat treatment process even more challenging.

Magnetic latching

A novel concept of magnetic latching and unlatching (release) is developed that aims for fixing the angular position of the folding actuator, even when the heating current for actuation is turned off. A soft magnetic NiMnGaCu thin film (5 µm) is attached onto the freely movable tile and is brought in contact with a permanent NdFeB magnet. The additional bending moment generated by the magnetic attraction force can contribute to enhanced folding angles. The magnetic attraction force is studied in terms of its dependence on temperature, angle and lateral misplacement. Successful latching is achieved for magnet positions at 102°, 120° and 125°. Two types of unlatching are demonstrated. For the first type, heating of the antagonist with a heating power of 55 mW generates an opposing bending moment that separates the two magnetic elements. The second type involves the heating of the soft magnetic NiMnGaCu film to reduce its magnetization. In this work, the thin film is only heated indirectly by resistive heating of the macro-scale hard magnet at a large heating power of 210 mW.

Table 7.1 compares the different fabricated actuator concepts according to Table 2.1. Miniaturization has neither worsened nor improved the folding angles. The change in material has only a minor influence on the folding performance and increases the folding range by ±10°.

	t [µm]	**w** [µm]	**L** [mm]	α [°]	M_z [mNmm]	**P** [mW]
Macroscopic single hinge						
TiNi	20	1000	3	150° / ±40°	110	300
Miniaturized single hinge						
TiNi, *500×75×5 µm³*	5	75	0.5	145° / -	-	10
TiNi, *250×30×8 µm³*	8	30	0.25	- / -	0.13	14
TiNiCu, *400×90×6 µm³*	6	90	0.4	140° / ±50°		70
Cascaded hinges						
TiNiCu, *HP1: 400×90×6 µm³* *HP2: 400×50×6 µm³*	6	50 / 90	1.4	180° / ±105°	-	90

Table 7.1.: Comparison of the performance of various folding actuators (SMA thickness t, SMA width w, SMA length L, total uni-/bi-directional folding angle, bending moment M_z and heating power P).

The SMA hinge being used as a bending element can never fully use its potential due to the distributed stress profile across its cross-section. There are portions within the bent hinge that are not strained, while the outer surfaces risk over-straining. These

constraints were studied theoretically and provide the basis for the actuator dimensions. The new concept of cascaded hinge folding actuators is one possibility to overcome the limitations related to the material and loading case. It proves to be successful and increases both, uni- and bi-directional folding range.
The heating power required for actuation scales with the actuator thickness and lateral dimensions. In addition, the material's resistivity plays an important role. The wet-etched and miniaturized TiNi folding actuators show lower heating powers. Their rough and defective surface contains holes in the hinge region that contribute to higher resistivity.

In his review article, Kejun Hu et al. [69] compares different concepts for the realization of bending movements using SMA actuators with regard to their use for origami robots [69]. Figure 7.1 summarizes the performance of three different actuator categories in a 3D-plot. The relevant characteristics are the diameter and length of the SMA element used in the actuator, and the output bi-directional folding range. For thin films and foils, the element's diameter refers to the thickness. As introduced in section 2.1.2 the actuator principles are divided into linear, torsional and bending type. The folding actuators fabricated and characterized in the framework of this thesis are of bending-type and are added in the 3D graph (highlighted in green).
In terms of hinge length and SMA thickness, the fabricated folding actuators are located far outside of the existing concepts and thus open up new options at miniature scales. The single hinge folding actuators can compete with other works in terms of angular folding performance. Their total folding angles (±40° = 80° and ±50° = 100°) are among the average of linear- and bending-type SMA actuators. The cascaded hinge folding actuator shows an exceptional total folding angle (±105° = 210°) and represents a new benchmark in this field.

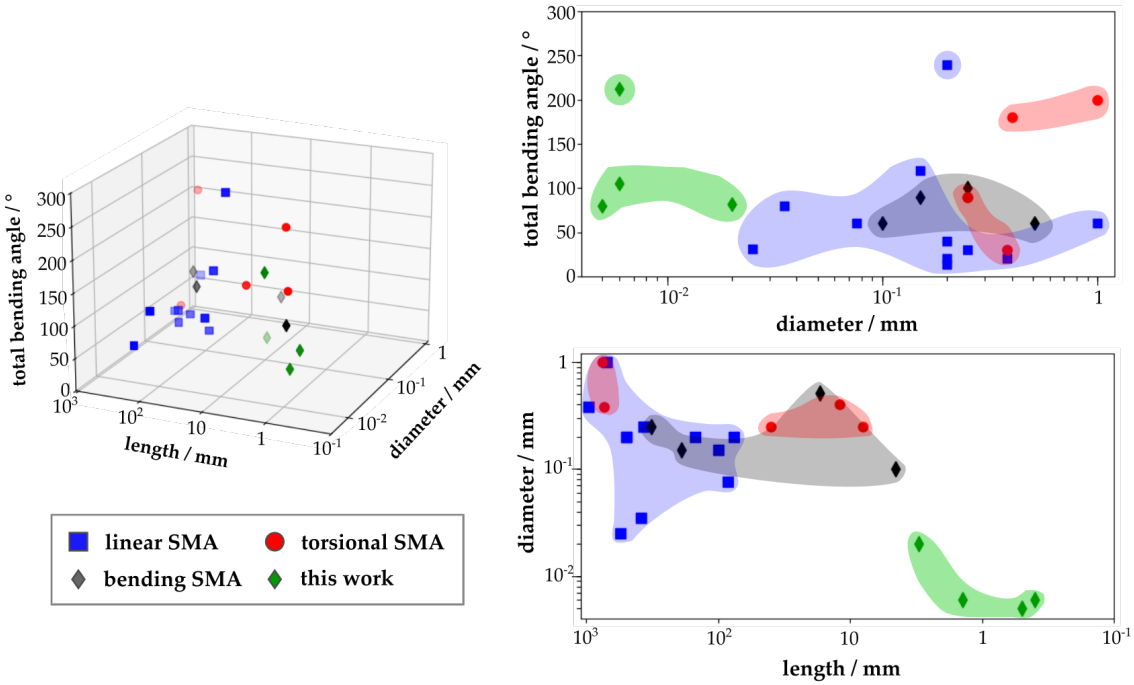

Figure 7.1.: Performance of various SMA-based actuators for folding from literature (adapted from [69]). Symbols and colors correspond to different actuator types. The bending-type actuators that are developed in this thesis, are highlighted in green.

8. Outlook

This thesis points out a new concept for SMA-based folding actuators that allows for miniaturization down to the micrometer range and enhanced folding performance well beyond the state-of-the art. Here, basic elements are studied extensively consisting of a pair of rigid tiles and a unidirectional, bidirectional or a bistable hinge mechanism with reversible latching performance. Further study on the following topics are recommended:

Design optimization:
Although various characterizations have been performed on uni-directional and bi-directional folding actuators, the experimental assessment of thermal, mechcanical and magnetic coupling effects at small scale is difficult. The material parameters obtained by experiments on large samples are utilized by project partners to develop a fully coupled simulation model of the SMA folding actuator [92]. It can serve to predict the macroscopic material behavior and help to understand performance-related phenomena such as local stress concentrations and temperature distribution. While temperature measurements at micro scale are difficult due to the limitations of IR thermography, simulations can provide estimates on temperature distributions and phase fractions. The geometry of the folding hinges can be optimized to generate a homogeneous temperature during Joule heating. Additionally, the separation between multiple hinge actuators affects their thermal and mechanical coupling. An experimental parametric study could help to calibrate the multiphysical model and provide further paths for optimization. Computation complexity and time could be reduced by implementing a lumped element model (LEM).

Magnetic latching:
In this work, only the hard magnet is heated resulting in a high power consumption. The ultimate goal is to locally heat the soft magnetic thin film. While samples with the foreseen layout for local heating of the NiMnGaCu film failed during fabrication in the time scope of this thesis, [93] shows the feasibility of this concept. The current pick-and-place method for bonding the soft magnetic film onto the tile becomes impratical

at micro scale. Besides direct sputtering of a NiMnGa-based film, alternative latching concepts have to be explored that allow for integration into a monolithic process route. One possible option are wax structures, which can be printed onto the tiles and can be heated locally for shifting between hard and sticky state.

Upscaling towards a multi-tile system:
The given layout can be extended to a 4-tile system, that folds into a tetrahedron by simply adding a tile on each edge of the triangular tile. The electrical connection via multiple power lines must be arranged onto the base tile. The extension towards a micro Origami device has been shown in [93]. For further upscaling, the SMA elements must be heated across multiple tiles while avoiding local overheating. The mechanical coupling effects when many (possibly connected) tiles fold simultaneously must be considered. Thermal coupling can occur between the multiple power lines and folding hinges by heat conduction. Additional isolation layers could be added. For full system integration, a control of folding should be implemented, such as using the intrinsic self-sensing potential of the SMA hinges. The change in resistivity related to the phase transformation of SMAs can be used to determine the folding angle. Furthermore, a folding algorithm is required to avoid collisions upon multi-tile folding. Existing Origami simulators can already calculate optimum folding sequences for custom 3D shapes. As the number of power lines increases with a multi-tile system, local power sources (e.g. batteries or capacitor) could be positioned onto some tiles. The distribution of many small logic and power controls is important to selectively control the multi-tile system and to reduce the number of power lines that have to guided across tiles.

Re-programmable matter
For realizing the vision of re-programmable matter, the individual folding hinges should be able to be re-programmed to new memory shapes by a local heat treatment. Like the actuation, this could ideally be achieved via Joule heating. This has already been shown in this thesis. However, much higher currents are involved and the heat treatment may damage neighbouring components. Laser heating could be an alternative. For this purpose the desired folding angle of a tile pair has to be set either by a cooperative motion of all remaining tiles or by an external guiding structure.
By overcoming the challenges of upscaling to a multi-tile systems and integrating a fully monolithic process fabrication alongside an efficient local heat-treatment, a versatile re-programmable actuator system can be developed. Its multifunctionality could provide solutions in various fields where deployable 3D structures are required.

Bibliography

[1] F. Momeni, S. M.Mehdi Hassani.N, X. Liu, and J. Ni, "A review of 4d printing", *Materials & Design*, vol. 122, pp. 42–79, Jan. 1, 2017, ISSN: 02641275. DOI: 10.1016/j.matdes.2017.02.068.

[2] E. Hawkes, B. An, N. M. Benbernou, H. Tanaka, S. Kim, E. D. Demaine, D. Rus, and R. J. Wood, "Programmable matter by folding", *Proceedings of the National Academy of Sciences of the United States of America*, vol. 107, no. 28, pp. 12 441–5, Jan. 1, 2010. DOI: 10.1073/pnas.0914069107.

[3] (). SPP 2206 - cooperative multistage multistable microactuator systems, SPP 2206 - Cooperative Multistage Multistable Microactuator Systems, [Online]. Available: www.spp-kommma.de.

[4] A. Ghassaei. (Jan. 1, 2017). Origami simulator, [Online]. Available: https://origamisimulator.org/.

[5] R. D. Resch, "Self-supporting structural unit having a series of repetitious geometrical modules: U.s. patent no. 3,407,558", pat.

[6] K. Miura, "Method of packaging and deployment of large membranes in space", *Institute of Space Science*, no. 618, pp. 1–9, Dec. 1985, ISSN: 0285-6808. [Online]. Available: https://cir.nii.ac.jp/crid/1574231877571121152.

[7] E. T. Filipov, T. Tachi, and G. H. Paulino, "Origami tubes assembled into stiff, yet reconfigurable structures and metamaterials", *Proceedings of the National Academy of Sciences of the United States of America*, vol. 112, no. 40, pp. 12 321–6, Jan. 1, 2015. DOI: 10.1073/pnas.1509465112.

[8] M. Meloni, J. Cai, Q. Zhang, D. Sang-Hoon Lee, M. Li, R. Ma, T. E. Parashkevov, and J. Feng, "Engineering origami: A comprehensive review of recent applications, design methods, and tools", *Advanced Science*, vol. 8, no. 13, Jan. 1, 2021, Number Of Volumes: 2000636, ISSN: 2198-3844. DOI: 10.1002/advs.202000636.

[9] R. J. Lang, "The science of origami", *Physics World*, vol. 20, no. 2, pp. 30–31, Jan. 1, 2007, ISSN: 0953-8585.

[10] ——, *A computational algorithm for origami design*. New York, New York, USA: ACM Press, Jan. 1, 1996. DOI: 10.1145/237218.237249.

[11] E. D. Demaine and J. O'Rourke, *Geometric Folding Algorithms: Linkages, Origami, Polyhedra*. Cambridge University Press, Jan. 1, 2007, ISBN: 978-1-107-39409-4.

[12] K. Fuchi and A. R. Diaz, "Origami design by topology optimization", *Journal of Mechanical Design*, vol. 135, no. 11, Jan. 1, 2013, Publisher: American Society of Mechanical Engineers Digital Collection, ISSN: 1050-0472. DOI: 10.1115/1.4025384.

[13] E. A. Peraza Hernandez, D. J. Hartl, and D. C. Lagoudas, *Active Origami*. Cham: Springer International Publishing, Jan. 1, 2019, ISBN: 978-3-319-91865-5. DOI: 10.1007/978-3-319-91866-2.

[14] T. Tachi, "Simulation of rigid origami", in *Origami 4*, R. J. Lang, Ed., CRC Press, Jan. 1, 2009, pp. 175–187, ISBN: 978-1-4398-7104-1.

[15] ——, *Rigid Origami Simulator & Freeform Origami*. Jan. 1, 2013. [Online]. Available: http://www.tsg.ne.jp/TT/software/ (visited on 03/14/2024).

[16] A. Ghassaei, E. D. Demaine, and G. Neil, "Fast, interactive origami simulation using GPU computation", in *Origami 7: Proceedings of the 7th International Meeting Proceedings of the 7th International Meeting on Origami in Science, Mathematics and Education*, vol. 4, Jan. 1, 2018, pp. 1151–1166.

[17] M. Schenk and S. D. Guest, "Origami folding: A structural engineering approach", in *Origami 5: Fifth International Meeting of Origami Science, Mathematics, and Education*, P. Wang-Iverson, R. J. Lang, and M. YIM, Eds., CRC Press, Jan. 1, 2016, pp. 291–304, ISBN: 978-1-4398-7350-2.

[18] Y. Zhu, M. Schenk, and E. T. Filipov, "A review on origami simulations: From kinematics, to mechanics, toward multiphysics", *Applied Mechanics Reviews*, vol. 74, no. 3, Jan. 1, 2022, ISSN: 0003-6900. DOI: 10.1115/1.4055031.

[19] S.-M. Baek, S. Yim, S.-H. Chae, D.-Y. Lee, and K.-J. Cho, "Ladybird beetle–inspired compliant origami", *Science Robotics*, vol. 5, no. 41, Jan. 1, 2020, Publisher: Science Robotics. DOI: 10.1126/scirobotics.aaz6262.

[20] J. T. Bruton, T. G. Nelson, T. K. Zimmerman, J. D. Fernelius, S. P. Magleby, and L. L. Howell, "Packing and deploying soft origami to and from cylindrical volumes with application to automotive airbags", *Royal Society open science*, vol. 3, no. 9, p. 160 429, Jan. 1, 2016, ISSN: 2054-5703. DOI: 10.1098/rsos.160429.

[21] W. Gao, K. Ramani, R. J. Cipra, and T. Siegmund, "Kinetogami: A reconfigurable, combinatorial, and printable sheet folding", *Journal of Mechanical Design*, vol. 135, no. 11, Jan. 1, 2013, Number Of Volumes: 111009, ISSN: 1050-0472. DOI: 10.1115/1.4025506.

[22] S. Yao, X. Liu, S. V. Georgakopoulos, and M. M. Tentzeris, "A novel reconfigurable origami spring antenna", in *IEEE Antennas and Propagation Society international symposium (APSURSI), 2014: 6 - 11 July 2014, Memphis, Tennessee, USA ; proceedings*, in collab. with I. of Electrical {and} Electronics Engineers and I. A. P̃. Society, Piscataway, NJ: IEEE, Jan. 1, 2014, pp. 374–375, ISBN: 978-1-4799-3540-6. DOI: 10.1109/APS.2014.6904519.

[23] S. Babaee, J. T. B. Overvelde, E. R. Chen, V. Tournat, and K. Bertoldi, "Reconfigurable origami-inspired acoustic waveguides", *Science advances*, vol. 2, no. 11, p. 1 601 019, Jan. 1, 2016. DOI: 10.1126/sciadv.1601019.

[24] C. H. Belke and J. Paik, "Mori: A modular origami robot", *IEEE/ASME transactions on mechatronics : a joint publication of the IEEE Industrial Electronics Society and the ASME Dynamic Systems and Control Division*, vol. 22, no. 5, pp. 2153–2164, Jan. 1, 2017, ISSN: 1083-4435. DOI: 10.1109/TMECH.2017.2697310.

[25] Y. Ke, J. Sharma, M. Liu, K. Jahn, Y. Liu, and H. Yan, "Scaffolded DNA origami of a DNA tetrahedron molecular container", *Nano letters*, vol. 9, no. 6, pp. 2445–7, Jan. 1, 2009. DOI: 10.1021/nl901165f.

[26] M. Z. Miskin, A. J. Cortese, K. Dorsey, E. P. Esposito, M. F. Reynolds, Q. Liu, M. Cao, D. A. Muller, P. L. McEuen, and I. Cohen, "Electronically integrated, mass-manufactured, microscopic robots", *Nature*, vol. 584, no. 7822, pp. 557–561, Jan. 1, 2020. DOI: 10.1038/s41586-020-2626-9.

[27] R. Gagler, A. Bugacov, B. E. Koel, and P. M. Will, "Voxels: Volume-enclosing microstructures", *Journal of Micromechanics and Microengineering*, vol. 18, no. 5, p. 055 025, Jan. 1, 2008, ISSN: 0960-1317. DOI: 10.1088/0960-1317/18/5/055025.

[28] S. Miyashita, L. Meeker, M. Gouldi, Y. Kawahara, and D. Rus, "Self-folding printable elastic electric devices: Resistor, capacitor, and inductor", in *IEEE International Conference on Robotics and Automation (ICRA), 2014: May 31, 2014 - June 7, 2014, Hong Kong, China*, in collab. with I. of Electrical {and} Electronics Engineers, Piscataway, NJ: IEEE, Jan. 1, 2014, pp. 1446–1453, ISBN: 978-1-4799-3685-4. DOI: 10.1109/ICRA.2014.6907042.

[29] W. Yan, S. Li, M. Deguchi, Z. Zheng, D. Rus, and A. Mehta, "Origami-based integration of robots that sense, decide, and respond", *Nature communications*, vol. 14, no. 1, p. 1553, Jan. 1, 2023. DOI: 10.1038/s41467-023-37158-9.

[30] T. H. Hong, S.-H. Park, J.-H. Park, N.-J. Paik, and Y.-L. Park, "Design of pneumatic origami muscle actuators (POMAs) for a soft robotic hand orthosis for grasping assistance", in *2020 3rd IEEE International Conference on Soft Robotics (RoboSoft)*, Jan. 1, 2020, pp. 627–632. DOI: 10.1109/RoboSoft48309.2020.9116046.

[31] P. W. K. Rothemund, "Folding DNA to create nanoscale shapes and patterns", *Nature*, vol. 440, no. 7082, pp. 297–302, Jan. 1, 2006. DOI: 10.1038/nature04586.

[32] T. Tørring, N. V. Voigt, J. Nangreave, H. Yan, and K. V. Gothelf, "DNA origami: A quantum leap for self-assembly of complex structures", *Chemical Society reviews*, vol. 40, no. 12, pp. 5636–46, Jan. 1, 2011. DOI: 10.1039/c1cs15057j.

[33] P. Wang, T. A. Meyer, V. Pan, P. K. Dutta, and Y. Ke, "The beauty and utility of DNA origami", *Chem*, vol. 2, no. 3, pp. 359–382, Jan. 1, 2017, ISSN: 24519294. DOI: 10.1016/j.chempr.2017.02.009.

[34] J. M. Zanardi Ocampo, P. O. Vaccaro, K. Kubota, T. Fleischmann, T. S. Wang, T. Aida, T. Ohnishi, A. Sugimura, R. Izumoto, M. Hosoda, and S. Nashima, "Characterization of GaAs-based micro-origami mirrors by optical actuation", *Microelectronic Engineering*, vol. 73-74, pp. 429–434, Jan. 1, 2004, Publisher: Elsevier BV, ISSN: 0167-9317. DOI: 10.1016/j.mee.2004.03.012.

[35] W. Xu, Y. Huang, H. Li, Y. Luo, and Y. Wu, "Research on mechanical properties and impact resistance of origami-based metamaterial for GIL", *Frontiers in Materials*, vol. 10, Jan. 1, 2023, Number Of Volumes: 1208510. DOI: 10.3389/fmats.2023.1208510.

[36] S. Xu, Z. Yan, K.-I. Jang, W. Huang, H. Fu, J. Kim, Z. Wei, M. Flavin, J. McCracken, R. Wang, A. Badea, Y. Liu, D. Xiao, G. Zhou, J. Lee, H. U. Chung, H. Cheng, W. Ren, A. Banks, X. Li, U. Paik, R. G. Nuzzo, Y. Huang, Y. Zhang, and J. A. Rogers, "Assembly of micro/nanomaterials into complex, three-dimensional architectures by compressive buckling", *Science (New York, N.Y.)*, vol. 347, no. 6218, pp. 154–9, Jan. 1, 2015. DOI: 10.1126/science.1260960.

[37] O. G. Schmidt and K. Eberl, "Nanotechnology. thin solid films roll up into nanotubes", *Nature*, vol. 410, no. 6825, p. 168, Jan. 1, 2001. DOI: 10.1038/35065525.

[38] J. Rogers, Y. Huang, O. G. Schmidt, and D. H. Gracias, "Origami MEMS and NEMS", *MRS Bulletin*, vol. 41, no. 2, pp. 123–129, Jan. 1, 2016, ISSN: 0883-7694. DOI: 10.1557/mrs.2016.2.

[39] S. Felton, M. Tolley, E. Demaine, D. Rus, and R. Wood, "Applied origami. a method for building self-folding machines", *Science (New York, N.Y.)*, vol. 345, no. 6197, pp. 644–646, Jan. 1, 2014. DOI: 10.1126/science.1252610.

[40] A. Firouzeh and J. Paik, "Robogami: A fully integrated low-profile robotic origami", *Journal of Mechanisms and Robotics*, vol. 7, no. 2, Jan. 1, 2015, ISSN: 1942-4302. DOI: 10.1115/1.4029491.

[41] A. Schulz, C. Sung, A. Spielberg, W. Zhao, R. Cheng, E. Grinspun, D. Rus, and W. Matusik, "Interactive robogami: An end-to-end system for design of robots with ground locomotion", *The International journal of robotics research*, vol. 36, no. 10, pp. 1131–1147, Jan. 1, 2017, ISSN: 0278-3649. DOI: 10.1177/0278364917723465.

[42] K. Kuribayashi, K. Tsuchiya, Z. You, D. Tomus, M. Umemoto, T. Ito, and M. Sasaki, "Self-deployable origami stent grafts as a biomedical application of ni-rich TiNi shape memory alloy foil", *Materials Science and Engineering: A*, vol. 419, no. 1, pp. 131–137, Jan. 1, 2006, ISSN: 09215093. DOI: 10.1016/j.msea.2005.12.016.

[43] M. Chauhan, J. H. Chandler, A. Jha, V. Subramaniam, K. L. Obstein, and P. Valdastri, "An origami-based soft robotic actuator for upper gastrointestinal endoscopic applications", *Frontiers in robotics and AI*, vol. 8, no. 664720, Jan. 1, 2021. DOI: 10.3389/frobt.2021.664720.

[44] T. Tachi, "Geometric considerations for the design of rigid origami structures", in *Proceedings of the International Association for Shell and Spatial Structures (IASS) Symposium*, 2010.

[45] P. K. Kumar and D. C. Lagoudas, "Introduction to shape memory alloys", in *Shape Memory Alloys*, D. C. Lagoudas, Ed., vol. 1, Boston, MA: Springer US, Jan. 1, 2008, ISBN: 978-0-387-47684-1.

[46] E. A. Peraza-Hernandez, D. J. Hartl, R. J. Malak Jr, and D. C. Lagoudas, "Origami-inspired active structures: A synthesis and review", *Smart Materials and Structures*, vol. 23, no. 9, Jan. 1, 2014, ISSN: 0964-1726. DOI: 10.1088/0964-1726/23/9/094001.

[47] G. McKnight and C. Henry, "Variable stiffness materials for reconfigurable surface applications", in *Smart Structures and Materials 2005: Active Materials: Behavior and Mechanics*, ser. SPIE Proceedings, W. D. Armstrong, Ed., SPIE, Jan. 1, 2005, p. 119. DOI: 10.1117/12.601495.

[48] D. C. Lagoudas, Ed., *Shape Memory Alloys*, vol. 1, Boston, MA: Springer US, Jan. 1, 2008, ISBN: 978-0-387-47684-1. DOI: 10.1007/978-0-387-47685-8.

[49] M. Kohl, *Shape memory microactuators*, ser. Microtechnology and MEMS. Berlin: Springer, Jan. 1, 2004, 247 pp., ISBN: 3-540-20635-3.

[50] K. Otsuka and C. M. Wayman, Eds., *Shape Memory Materials*, in collab. with C. Wayman, Cambridge: Cambridge Univ. Press, Jan. 1, 1999, 284 pp., ISBN: 0-521-44487-X.

[51] S. Miyazaki, W. M. Huang, and Y. Q. Fu, Eds., *Thin film shape memory alloys: Fundamentals and device applications*, Cambridge: Cambridge University Press, Jan. 1, 2009, 459 pp., ISBN: 978-0-511-63536-6. DOI: 10.1017/CBO9780511635366.

[52] S. Miyazaki and K. Otsuka, "Deformation and transition behavior associated with the r-phase in ti-ni alloys", *Metallurgical Transactions A*, vol. 17, no. 1, pp. 53–63, Jan. 1, 1986, ISSN: 0360-2133. DOI: 10.1007/BF02644442.

[53] T. W. Duerig, K. N. Melton, and D. Stöckel, *Engineering Aspects of Shape Memory Alloys*. Burlington: Elsevier Science, Jan. 1, 1990, 512 pp., ISBN: 978-0-7506-1009-4.

[54] Y.-T. Chen, A. G. Kolhatkar, O. Zenasni, S. Xu, and T. R. Lee, "Biosensing using magnetic particle detection techniques", *Sensors*, vol. 17, no. 10, p. 2300, Oct. 10, 2017, ISSN: 1424-8220. DOI: 10.3390/s17102300.

[55] D. C. Jiles and D. L. Atherton, "Theory of the magnetisation process in ferromagnets and its application to the magnetomechanical effect", *Journal of Physics D: Applied Physics*, vol. 17, no. 6, p. 1265, Jun. 1984, ISSN: 0022-3727. DOI: 10.1088/0022-3727/17/6/023.

[56] N. A. Spaldin, *Magnetic materials: fundamentals and applications*, 2nd ed. Cambridge: Cambridge University Press, 2011, OCLC: 659500281, ISBN: 978-0-511-90071-6.

[57] A. Guinier and R. Jullien, *The solid state: from superconductors to superalloys*, in collab. with International Union of Crystallography, ser. International Union of Crystallography texts on crystallography 1. New York: Oxford University Press, 1989, 271 pp., ISBN: 978-0-19-855554-4.

[58] P. J. Webster, K. R. A. Ziebeck, S. L. Town, and M. S. Peak, "Magnetic order and phase transformation in ni_2MnGa", *Philosophical Magazine B*, vol. 49, no. 3, pp. 295–310, Mar. 1984, ISSN: 1364-2812, 1463-6417. DOI: 10.1080/13642817408246515.

[59] A. N. Vasil'ev, A. D. Bozhko, V. V. Khovailo, I. E. Dikshtein, V. G. Shavrov, V. D. Buchelnikov, M. Matsumoto, S. Suzuki, T. Takagi, and J. Tani, "Structural and magnetic phase transitions in shape-memory alloys $ni_{2+x}mn_{1-x}ga$", *Physical Review B*, vol. 59, no. 2, pp. 1113–1120, Jan. 1, 1999, ISSN: 0163-1829, 1095-3795. DOI: 10.1103/PhysRevB.59.1113. [Online]. Available: https://link.aps.org/doi/10.1103/PhysRevB.59.1113 (visited on 07/24/2024).

[60] Fink, Lukas, "Verbesserung der magnetischen und thermomagnetischen eigenschaften von ni-mn-ga-basierten schichten", PhD thesis, TU Dresden, Dresden, Jan. 25, 2024.

[61] H. Yuan, J. Fauroux, F. Chapelle, and X. Balandraud, "A review of rotary actuators based on shape memory alloys", *Journal of Intelligent Material Systems and Structures*, vol. 28, no. 14, pp. 1863–1885, Aug. 2017, ISSN: 1045-389X, 1530-8138. DOI: 10.1177/1045389X16682848.

[62] X. Yan, D. Huang, and X. Zhang, "Note: A novel curvature-driven shape memory alloy torsional actuator", *Review of Scientific Instruments*, vol. 85, no. 12, p. 126 109, Dec. 1, 2014, ISSN: 0034-6748, 1089-7623. DOI: 10.1063/1.4904734.

[63] H.-H. Yue, Z.-Q. Liu, H. Yuan, Y.-F. Long, and H.-S. Tzou, "Analysis and design of active morphing units based on SMA actuators", in *Volume 4B: Dynamics, Vibration and Control*, San Diego, California, USA: American Society of Mechanical Engineers, Nov. 15, 2013, ISBN: 978-0-7918-5625-3. DOI: 10.1115/IMECE2013-65546.

[64] J. K. Paik and R. J. Wood, "A bidirectional shape memory alloy folding actuator", *Smart Materials and Structures*, vol. 21, no. 6, p. 065 013, Jan. 1, 2012, ISSN: 0964-1726. DOI: 10.1088/0964-1726/21/6/065013.

[65] E. A. Peraza-Hernandez, D. J. Hartl, and R. J. M. Jr, "Design and numerical analysis of an SMA mesh-based self-folding sheet", *Smart Materials and Structures*, vol. 22, no. 9, p. 094 008, Jan. 1, 2013, Publisher: IOP Publishing, ISSN: 0964-1726. DOI: 10.1088/0964-1726/22/9/094008.

[66] B. H. Shin, T. Jang, B.-J. Ryu, and Y. Kim, "A modular torsional actuator using shape memory alloy wires", *Journal of Intelligent Material Systems and Structures*, vol. 27, no. 12, pp. 1658–1665, Jul. 2016, ISSN: 1045-389X, 1530-8138. DOI: 10.1177/1045389X15600084.

[67] Y. Kim, T. Jang, H. Gurung, N. A. Mansour, B. Ryu, and B. Shin, "Bidirectional rotating actuators using shape memory alloy wires", *Sensors and Actuators A: Physical*, vol. 295, pp. 512–522, Aug. 2019, ISSN: 09244247. DOI: 10.1016/j.sna.2019.05.047.

[68] K. Zheng, E. Gao, B. Tian, J. Liang, Q. Liu, E. Xue, Q. Shao, and W. Wu, "Modularized paper actuator based on shape memory alloy, printed heater, and origami", *Advanced Intelligent Systems*, vol. 4, no. 12, p. 2 200 194, Dec. 2022, ISSN: 2640-4567. DOI: 10.1002/aisy.202200194.

[69] K. Hu, K. Rabenorosoa, and M. Ouisse, "A review of SMA-based actuators for bidirectional rotational motion: Application to origami robots", *Frontiers in Robotics and AI*, vol. 8, p. 678 486, Jul. 2, 2021, ISSN: 2296-9144. DOI: 10.3389/frobt.2021.678486.

[70] J. K. Paik, E. Hawkes, and R. J. Wood, "A novel low-profile shape memory alloy torsional actuator", *Smart Materials and Structures*, vol. 19, no. 12, p. 125 014, Jan. 1, 2010, Num Pages: 10, ISSN: 0964-1726. DOI: 10.1088/0964-1726/19/12/125014.

[71] J. Frenzel, Z. Zhang, K. Neuking, and G. Eggeler, "High quality vacuum induction melting of small quantities of NiTi shape memory alloys in graphite crucibles", *Journal of Alloys and Compounds*, vol. 385, no. 1, pp. 214–223, Jan. 1, 2004, ISSN: 09258388. DOI: 10.1016/j.jallcom.2004.05.002.

[72] J. Frenzel, Z. Zhang, C. Somsen, K. Neuking, and G. Eggeler, "Influence of carbon on martensitic phase transformations in NiTi shape memory alloys", *Acta Materialia*, vol. 55, no. 4, pp. 1331–1341, Jan. 1, 2007, ISSN: 13596454. DOI: 10.1016/j.actamat.2006.10.006.

[73] T. Saburi, "TiNi shape memory alloys", in *Shape Memory Materials*, K. Otsuka and C. M. Wayman, Eds., in collab. with C. Wayman, Cambridge: Cambridge Univ. Press, Jan. 1, 1999, ISBN: 0-521-44487-X.

[74] "Thin film technology", IEC, Jan. 1, 2018, Issue: 523-05-02. [Online]. Available: www.electropedia.org.

[75] Y. Suzuki, "Fabrication of shape memory materials", in *Shape Memory Materials*, K. Otsuka and C. M. Wayman, Eds., in collab. with C. Wayman, Cambridge: Cambridge Univ. Press, Jan. 1, 1999, pp. 133–148, ISBN: 0-521-44487-X.

[76] Q. S. Zheng and Y. Liu, "Prediction of the detwinning anisotropy in textured NiTi shape memory alloy", *Philosophical Magazine A*, vol. 82, no. 4, pp. 665–683, Jan. 1, 2002, Publisher: Taylor & Francis, ISSN: 0141-8610. DOI: 10.1080/01418610208243195.

[77] K. Kim and S. Daly, "The effect of texture on stress-induced martensite formation in nickel–titanium", *Smart Materials and Structures*, vol. 22, no. 7, p. 075 012, Jan. 1, 2013, ISSN: 0964-1726. DOI: 10.1088/0964-1726/22/7/075012.

[78] R. Lima de Miranda, C. Zamponi, and E. Quandt, "Micropatterned freestanding superelastic TiNi films", *Advanced Engineering Materials*, vol. 15, no. 1, pp. 66–69, Jan. 1, 2013, ISSN: 1438-1656. DOI: 10.1002/adem.201200197.

[79] H. H. Gatzen, V. Saile, and J. Leuthold, *Micro and Nano Fabrication: Tools and Processes*. Berlin, Heidelberg: Springer Berlin Heidelberg, Jan. 1, 2015, 519 pp., ISBN: 978-3-662-44394-1.

[80] S. Hengsbach, "Introduction to maskless laser-writing for generation of (sub) microstructures", Jan. 1, 2020.

[81] H. Instruments and H. Instruments, "DWL66+: The ultimate lithography research tool". [Online]. Available: https://heidelberg-instruments.com/product/dwl-66-laser-lithography-system/.

[82] H. Cho and S. Miyazaki, "TiNi multilayer thin films", in *Thin film shape memory alloys: Fundamentals and device applications*, S. Miyazaki, W. M. Huang, and Y. Q. Fu, Eds., Cambridge: Cambridge University Press, Jan. 1, 2009, pp. 110–123, ISBN: 978-0-511-63536-6.

[83] J. A. Shaw, C. B. Churchill, and M. A. Iadicola, "TIPS AND TRICKS FOR CHARACTERIZING SHAPE MEMORY ALLOY WIRE: PART 1-DIFFERENTIAL SCANNING CALORIMETRY AND BASIC PHENOMENA", *Experimental Techniques*, vol. 32, no. 5, pp. 55–62, Jan. 1, 2008, ISSN: 07328818. DOI: 10.1111/j.1747-1567.2008.00410.x.

[84] *Standard test method for determining specific heat capacity by differential scanning calorimetry, ASTM e1269*, version 11, May 2011.

[85] F. M. Smits, "Measurement of sheet resistivities with the four-point probe", *Bell System Technical Journal*, vol. 37, no. 3, pp. 711–718, 1958, ISSN: 00058580. DOI: 10.1002/j.1538-7305.1958.tb03883.x.

[86] M. Keret-Klainer, R. Padan, Y. Khoptiar, Y. Kauffmann, and Y. Amouyal, "Tailoring thermal and electrical conductivities of a ni-ti-hf-based shape memory alloy by microstructure design", *Journal of Materials Science*, vol. 57, no. 25, pp. 12 107–12 124, Jan. 1, 2022, ISSN: 0022-2461. DOI: 10.1007/s10853-022-07383-6.

[87] V. Gottwald, *SMA Bending Microactuators for Origami-Type Applications: Master Thesis*. IMT, Karlsruhe Institute of Technology, 2022.

[88] H. Tobushi, P.-h. Lin, T. Sawada, and T. Hattori, "Recovery stress associated with the r-phase transformation in TiNi shape memory alloy. properties under constant maximum strain and residual strain", *TRANSACTIONS OF THE JAPAN SOCIETY OF MECHANICAL ENGINEERS Series A*, vol. 59, no. 560, pp. 1075–1081, 1993, ISSN: 0387-5008, 1884-8338. DOI: 10.1299/kikaia.59.1075.

[89] DuPont. (). Kapton® EN polyimide film - datasheet, [Online]. Available: https://www.dupont.com/electronics-industrial/kapton-en.html (visited on 04/15/2024).

[90] H. Talebi, H. Golestanian, M. Zakerzadeh, and H. Homaei, "Thermoelectric heat transfer modeling of shape memory alloy actuators", presented at the The 22st Annual International Conference on Mechanical Engineering-ISME2014, Ahvaz, Iran, Apr. 22, 2014.

[91] L. Fink, S. Kar, K. Lünser, K. Nielsch, H. Reith, and S. Fähler, "Integration of multifunctional epitaxial (magnetic) shape memory films in silicon microtechnology", *Advanced Functional Materials*, vol. 33, no. 51, p. 2 305 273, Dec. 1, 2023, Publisher: John Wiley & Sons, Ltd, ISSN: 1616-3028. DOI: 10.1002/adfm.202305273.

[92] G. K. Tshikwand, L. Seigner, F. Wendler, and M. Kohl, "Coupled finite element simulation of shape memory bending microactuator", *Shape Memory and Superelasticity*, vol. 8, no. 4, pp. 373–393, Jan. 1, 2022, ISSN: 2199-384X. DOI: 10.1007/s40830-022-00396-9.

[93] V. Gottwald, L. Seigner, and M. Kohl, "Development of a re-programmable micro origami device", presented at the Int. Conf. and Exhibition on New Actuator Systems and Applications - Actuator'24, Wiesbaden, Germany, Jun. 2024.

A. Appendix

A.1. Anisotropic Material Behavior of cold-rolled 20 µm TiNi

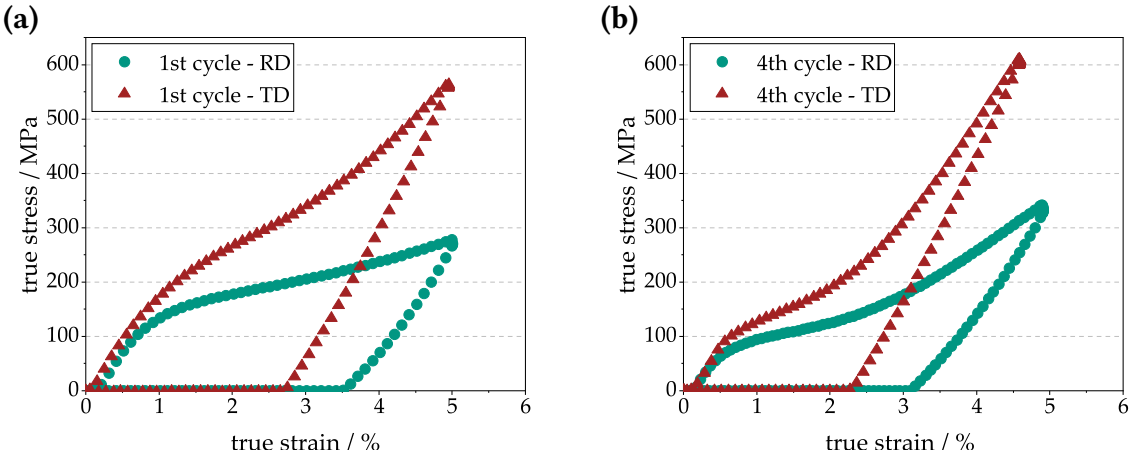

Figure A.1.: Tensile tests of 20 µm TiNi cold-rolled foil in rolling (RD) and transverse direction (TD) **(a)** Initial cycle, **(b)** 4th loading cycle.

A.2. Temperature-dependent Elastic Modulus of 20 µm TiNi

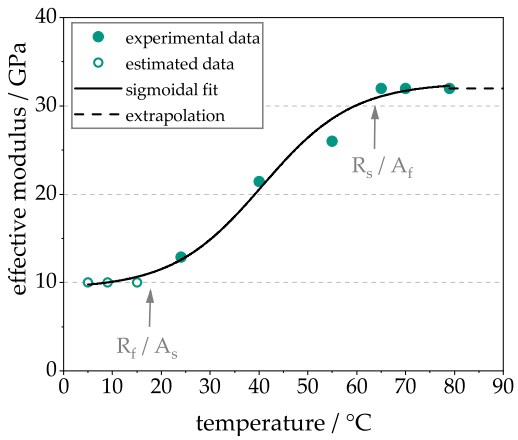

Figure A.2.: Effective elastic modulus derived from linear fit of tensile loaded samples.

A.3. Re-annealing of SMA structures in Vacuum Furnace

The heat treatment of SMA foil structures requires a customized annealing setup to imprint a folded configuration memory shape. To protect the SMA from oxidation, it is covered with Ti foils that act as an oxygen getter. As schematically shown in Figure A.3 the sequential steps are:

1. The laser-cut SMA structure is placed between two Ti foils (d = 100 µm) and positioned onto the annealing jig using a centering pin.
2. The foil stack is folded into a 180° configuration.
3. The annealing jig is closed by its counterpart and fixed onto a temperature sensor with screws.
4. The annealing jig is placed into a quartz tube that is evacuated by the vacuum pump.
5. The quartz tube is put into a heated tube furnace.
6. The heat treatment is run for 45 min at a constant temperature of 460 °C.
7. The annealing jig is quenched by nitrogen flushing of the quartz tube.
8. The annealing jig is removed from the quartz tube and the SMA structure is released from the setup.

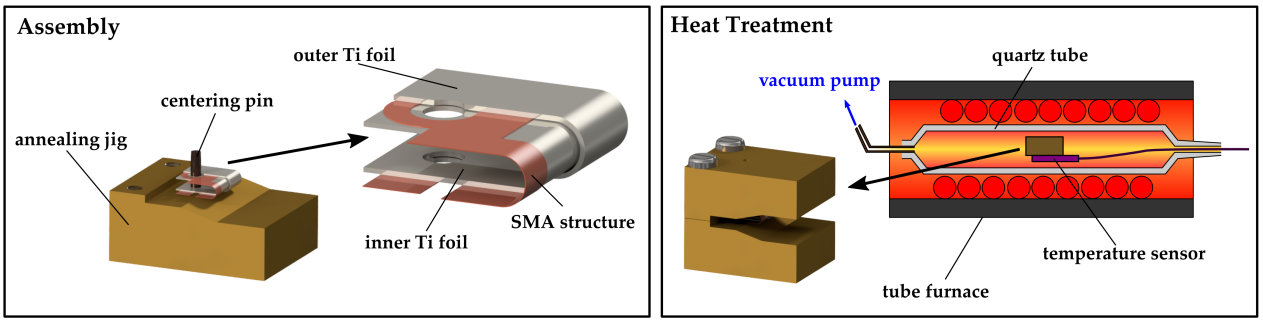

Figure A.3.: Annealing procedure of SMA foil structures.

A.4. Bi-directional Folding of Coupled TiNi Actuators

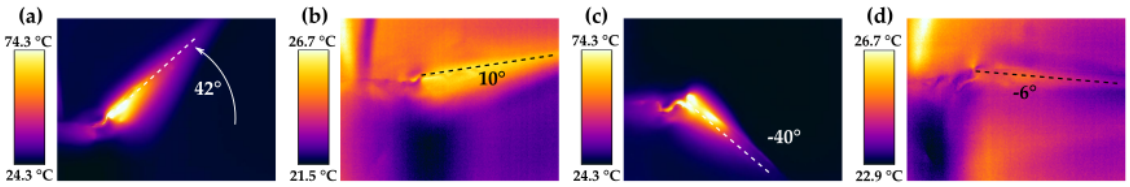

Figure A.4.: Reversible and bi-directional folding actuation sequence: **(a)** heating of the protagonist, **(b)** cooled state after protagonist heating, **(c)** heating of the antagonist, **(d)** cooled state after antagonist heating.

A.5. Temperature-dependent Elastic Modulus of 6 µm TiNiCu

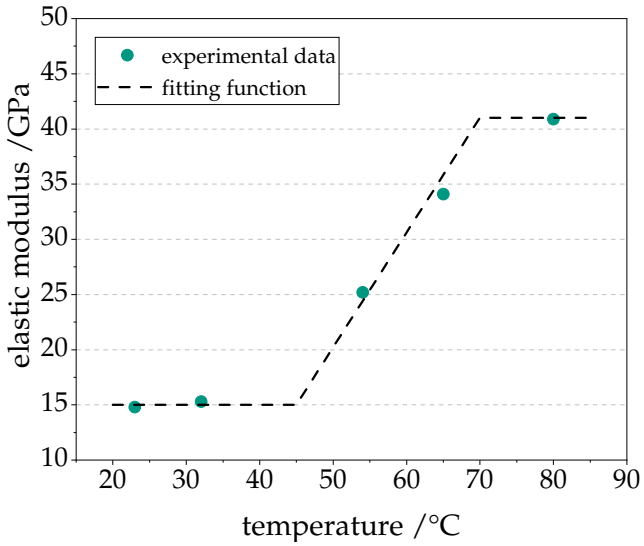

Figure A.5.: Effective elastic modulus of 6 µm TiNiCu film derived by linear fit of tensile loaded samples in heating chamber.

A.6. Material Parameters for FE Simulation

Parameter	Symbol	Value	Unit
Density (TiNiCu)	ρ_{TiNiCu}	6.4	g/cm³
Density (Polyimide)	ρ_{PI}	1.4	g/cm³
Thermal conductivity (TiNiCu)	k_{th}^{TiNiCu}	1.5	W/m/K
Thermal conductivity (Polyimide)	k_{th}^{PI}	0.15	W/m/K
Electrical conductivity (TiNiCu)	κ_e^{TiNiCu}	1.9×10^5	S/m
Electrical conductivity (Polyimide)	κ_e^{PI}	1×10^{-17}	S/m
Specific heat capacity (TiNiCu)	$c_{p,TiNiCu}$	320	J/kg/K
Specific heat capacity (Polyimide))	$c_{p,PI}$	1100	J/kg/K

Table A.1.: Summary of material parameters for the electro-thermal multiphysical FE model in COMSOL Multiphysics.

A.7. Magnetic Force Measurements for different Tilt Angles

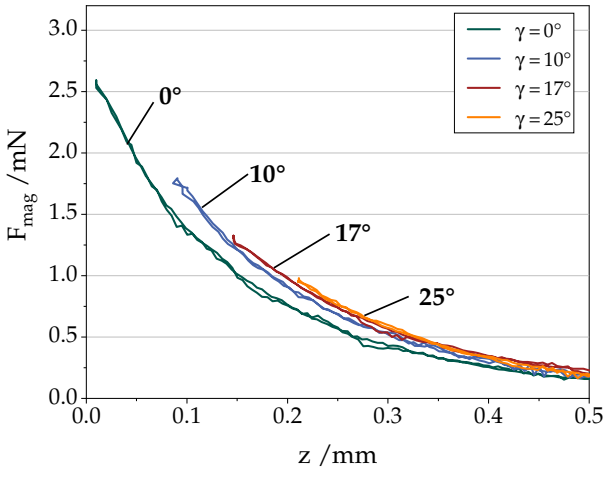

Figure A.6.: Magnetic attraction force as a function of distance z (effective distance between film center and magnet surface) for different tilt angles γ.

A.8. Latching and Unlatching of the Bi-directional Actuator

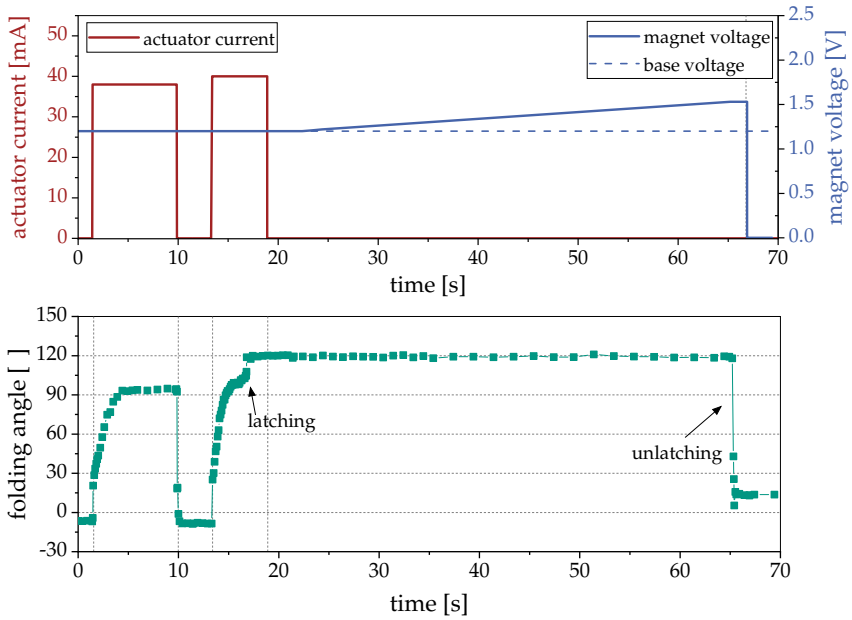

Figure A.7.: Latching and unlatching of folding actuator for a base voltage of 1.2 V.

List of Figures

List of Tables